T.C. DOGUS UNIVERSITY

Institute of Science

EM Diffraction Modeling with Numerical Methods

Ph.D. Thesis

Mehmet Alper USLU

2011198002

Thesis Supervisor: Prof.Dr. Ercan TOPUZ

Istanbul, January 2016

Contents

ACKNOWLEDGEMENTS

I would like to express my deepest gratitude to my co-supervisor, Prof. Dr. Levent SEVGI, for his guidance and valuable help throughout the thesis. He provided me with a better understanding of many concepts as well as academic insight. His contributions will effect in the rest of my academic life. He is actually more than supervisor for me, he is my mentor, my teacher and my second father.

I would like to thank my co-supervisor Prof. Dr. Ercan TOPUZ for his scientific contributions to my knowledge on electromagnetic theory from undergraduate to doctorate. I would not progress on electromagnetic theory without his teaching.

I would like to also thank Assist. Prof. Dr. Cagatay ULUISIK. He was like a brother to me throughout all my graduate and undergraduate studies in Dogus University in the past 10 years. Without his support I would not continue my academic career.

I would like to thank my mother Hicran USLU, my sister Hande Ceren ARSLAN and my father Ilbey USLU for supporting me in every way they can.

Finally, my special thanks go to Tuğba YÜZÜAK for bringing me invaluable feelings and happiness during a significant portion of my doctorate education. I admire you for being wonderful, kind person. Although you are far away from me, I will never forget you and your value.

ABSTRACT

Electromagnetic scattering theory is crucial to understand interaction of electromagnetic waves with objects and medium in which it propagates. Scattering fields are formed primarily by reflected, refracted and diffracted fields. There are also other wave phenomenon such as creeping waves, whispering-galley waves, etc. but all these phenomenon are formed by the interaction of reflected, refracted and diffracted fields.

Each scattering phenomenon should be considered carefully in the design of electronic devices. For example, warplane designer should minimize radar cross section (RCS) by avoiding reflective surfaces that may direct incoming radar wave towards radar receiver. Another example is that, today's electronic circuits contain so many components and conductive traces. Unwanted incoming radiation can reach critical components by being subjected to various scattering mechanisms. Therefore, EMC engineers should protect important parts of the devices by applying shielding techniques. As a final example, mobile phone designers should control the electromagnetic energy radiated towards human head to reduce specific absorption rate (SAR) value. This is accomplished by covering the back side of mobile phone with specific materials e.g. perfect electric conductor (PEC) materials. All these applications require extensive knowledge on scattering theory.

Reflection and refraction phenomenon has long been analyzed via well-known Snell's law. On the other hand, diffraction is much more difficult to analyze. There is no simple formulation to analyze diffraction. Exact solutions of diffracted fields are only known for a limited number of geometries such as wedge, sphere, and cylinder. In addition, these solutions are generally in the form of infinite series that are slowly convergent at high frequencies (i.e. when the wavelength is very small compare to the object size). Hence their applicability is limited. High frequency asymptotic (HFA) methods such as geometric theory of diffraction (GTD) and physical theory of diffraction (PTD) are developed to overcome this difficulty. These methods are derived from the exact solution of the problem and can be used to analyze diffraction mechanism at high frequencies. With today's high speed modern computers, it is also possible to analyze diffraction phenomena numerically. Numerical methods such as finite difference time domain (FDTD), method of moments (MoM) and finite element method (FEM) can be used for this purpose. These methods are

used in broad range of frequencies and the upper frequency limit depend on the computer's resources.

In this dissertation, we advanced the numerical diffraction theory by proposing three novel time domain based diffraction models: double tip diffraction model (Chapter 3), soft-hard strip diffraction model (Chapter 4) and time domain fringe current model (Chapter 5). In double tip diffraction model study, we obtained diffracted fields around 2D rectangular object for various incidence angles and rectangle thicknesses with FDTD method. The verification is performed with MoM model. In soft-hard strip diffraction model study, diffracted fields around a 2D canonical strip geometry with one face hard and the other face soft boundary condition (BC) is obtained with FDTD method. The model is verified with existing MoM solution. Finally in time domain fringe current model, we obtain fringe currents that are induced on 2D wedge geometry that is illuminated by a line source. We then calculate fringe waves radiated by fringe currents and verified proposed model with existing PTD and MoM solutions.

ÖZET

Elektromanyetik saçılma teorisi elektromanyetik dalgaların nesnelerle veya yayıldığı ortamlarla etkişemini anlamak için çok önemlidir. Bir objeden saçılan alanlar başlıca yansıyan, kırılan, kırınan alanlardan oluşur. Bunların dışında whispering-galley, creeping vb. alanlarda mevcuttur fakat tüm bu alanlar yansıyan, kırılan ve kırınan alanların birbirleriyle etkileşimlerinden dolayı oluşur.

Elektronik cihaz tasarımında bütün saçılma mekanizmaları göz önünde bulundurulmalıdır. Örneğin, savaş uçağı tasarımcısı gelen radar sinyalini radar vericisine doğru yönlendirecek yansıtıcı yüzey kullanımından olabildiğince kaçınmalıdır. Bir diğer örnek olarak, günümüzün elektronik devreleri oldukça fazla bileşen ve devre yolundan oluşur. Dış ortamdan gelen istenmeyen elektromanyetik radyasyon birden fazla saçılma mekanizmasına maruz kalarak devredeki kritik bileşenlere ulaşabilir. Bu yüzden elektromanyetik uyumluluk (EMC) mühendisleri cihazlardaki kritik parçaları çeşitli ekranlama teknikleriyle koruma altına almalıdırlar. Son bir örnek olarak, cep telefonu tasarımcıları insan kafasına doğru yayılan elektromanyetik enerjiyi özgül emilim oranını (SAR) düşürmek için yansıtmalıdırlar. Bu işlem cep telefonlarının arka yüzeyinin özel materyallerle (ör. süper elektriktriksel iletken), kaplanılmasıyla gerçekleştirilir. Bahsettiğimiz tüm uygulamalar saçılma teorisinin iyi bir biçimde anlaşılmasıyla mümkündür.

Yansıma ve kırılma saçılma mekanizmaları uzun süreden beri herkes tarafından bilinen Snell yasası ile incelenmektedir. Diğer taraftan, kırınım saçılma mekanizması için bu şekilde bir formülasyon bulunmamaktadır. Kırınan alanların kesin/tam çözümleri sadece belli başlı kanonik geometriler (ör. Kama, küre ve silindir) için bilinmektedir. Bunun yanında bu çözümler genelde yüksek frekanslarda (dalga boyunun obje boyutlarından çok küçük olduğu durumlarda) yavaş yakınsayan sonsuz seri formatındadır. Bu yüzden bu çözümlerin kullanım alanları sınırlıdır. Kesin çözümleri kullanmakta karşılaşılan sorunları ortadan kaldırmak için geometrik kırınım teorisi (GTD), fiziksel kırınım teorisi (PTD) gibi metotlar geliştirilmiştir. Bu metotlar problemin kesin çözümü kullanılarak elde edilmiştir ve kırınım mekanizmasını sadece yüksek frekanslarda analiz etmek için kullanılabilir. Günümüzün modern ve yüksek hızlı bilgisayarları kırınım mekanizmasını analiz etmek için nümerik yöntemlerin kullanımına izin vermektedir. Zamanda sonlu farklar metodu

(FDTD), moment metodu (MoM) ve sonlu elemanlar metodu (FEM) bu amaçla kullanılabilmektedir. Tüm bu nümerik metodlar geniş bir frekans aralığında kullanılabilir ve frekans üst limiti kullanılan bilgisayarın kaynaklarına bağlıdır.

Bu tez kapsamında çift uçlu kırınım modeli (Bölüm 3), yumuşak-sert şerit kırınım modeli (Bölüm 4) ve zaman domeninde kenar akımları modeli (Bölüm 5) adlı üç adet yeni kırınım modeli zaman domeninde FDTD yöntemi ile geliştirilerek nümerik kırınım teorisine katkıda bulunulmuştur. Çift uçlu kırınım modeli çalışmasında iki boyutlu dikdörtgensel nesneden oluşan kırınan alanlar çeşitli gelen dalga açısı ve dikgörtgen kalınlığında incelenmiştir. Sonuçların doğruluğu MoM metodu kullanılarak sağlanmıştır. Yumuşak-sert kırınım modeli çalışmasında, bir tarafı yumuşak diğer tarafı sert sınır koşuluna sahip iki boyutlu şerit geometrisinden kırınan alanlar zaman domeninde elde edilmiştir. Model halihazırda var olan MoM çözümü kullanılarak doğrulanmıştır. Son olarak, zaman domeninde kenar akımları modeli çalışmasında iki boyutlu kama geometrisinin çizgisel kaynak tarafından aydınlatılması sonucunda yüzeyde indüklenen kenar akımları zaman domeninde elde edilmiştir. Daha sonra kenar akımlarından dolayı oluşan kenar alanları hesaplanmış ve model hali hazırda var olan MoM ve PTD çözümü ile doğrulanmıştır.

LIST OF FIGURES

LIST OF SYMBOLS/ABBREVIATIONS

$2D$	Two-Dimensional
$3D$	Three-Dimensional
$\boldsymbol{B}$	Magnetic flux density vector
$\boldsymbol{D}$	Electric flux density vector
f	Frequency
$\boldsymbol{H}$	Magnetic field intensity vector
j	Imaginary unit
$j^{(0)}$	Uniform surface currents generated by the incident field
$j^{(1)}$	Non-uniform surface currents generated by the incident field
$\boldsymbol{J}$	Electric current density vector
$\boldsymbol{k}$	Wave vector
$\boldsymbol{M}$	Magnetic current density vector
∇	Gradient
∇x	Curl
ϵ	Electrical permittivity
ϵ_r	Relative electrical permittivity
μ	Magnetic permeability
σ	Electrical conductivity
ω	Wave angular frequency
ABC	Absorbing Boundary Condition
BC	Boundary Condition
DSI	Double Side Illumination
EM	Electromagnetic
EMC	Electromagnetic Compatibility
FDTD	Finite Difference Time Domain
FEM	Finite Element Method
FFT	Fast Fourier Transform
GO	Geometric Optics
GTD	Geometric Theory of Diffraction
GUI	Graphical User Interface
HBC	Hard Boundary Condition
HFA	High Frequency Asymptotic
ISB	Incident Shadow Boundary
LU	Lower Upper
MoM	Method of Moments

PEC	Perfect electric conductor
PMC	Perfect Magnetic Conductor
PML	Perfectly Matched Layer
PO	Physical Optics
PTD	Physical Theory of Diffraction
RBC	Radiation Boundary Condition
RCS	Radar Cross Section
RSB	Reflection Shadow Boundary
SAR	Specific Absorption Rate
SBC	Soft Boundary Condition
SSI	Single Side Illumination
TE	Transverse Electric
TM	Transverse Magnetic
UTD	Uniform Theory of Diffraction

1. INTRODUCTION

1.1. Research Overview

Electromagnetic (EM) waves interact with objects and media, in which they travel, by inducing currents in the object body. These induced currents give rise to scattered fields which are formed by reflected, refracted and diffracted fields. Reflection occurs when electromagnetic wave bounces from a surface back towards the source. Refraction occurs when electromagnetic waves are deflected as the wave goes through a substance. The wave generally changes its the speed and angle of its general direction. Diffraction occurs when electromagnetic wave passes an edge, passes through a narrow gap or goes past an object. Diffracted waves radiate in all directions as if being emerged by a point source. It is for this reason that signals are able to provide coverage even in hilly or mountainous terrain. Diffraction theory is used in many areas by physicists, mathematicians and various engineering disciplines. For example, telecommunications engineer should study the effects of building's edges or hills located in transmission path before designing the link.

Each scattering mechanism needs to be modeled and considered separately for the design of targets with desired scattered field characteristics. Reflection and refraction can be modeled with well-known Snell's law but diffraction is much more difficult to model. Exact solution of diffracted fields is obtained from an appropriate boundary value problem for Maxwell's equations. However, there are only a few problems such as infinite half-plane, wedge and circular cylinder that allows explicit exact solutions [1], [2]. These problems are also called as canonical problems. The solutions of canonical problems are generally in the form of infinite series (e.g., a series formed by Hankel and Bessel functions of any kind) which are slowly convergent for the electrically large objects ($l > \lambda$). Hence they have limited applicability at high frequencies.

High frequency asymptotic (HFA) methods such as geometric theory of diffraction (GTD) [3], uniform theory of diffraction (UTD) [4] and physical theory of diffraction (PTD) [5], [6] can be used to analyze diffraction approximately when the wavelength is small compared to the object being considered. These methods are constructed by using either direct or indirect approach [7]. In the former approach, asymptotic method applied to Maxwell's equations directly at the beginning of the problem, while in the latter,

asymptotic method is applied to the exact solution of the problem to construct approximate asymptotic solution. At high frequencies, diffracted fields obey localization principle i.e. they don't depend on every point on the surface of the scatterer but only on the points located in the vicinity of discontinuities e.g. tips, edges and vertices. Localization principle allows HFA methods to calculate diffracted fields around more complex shapes. This can be accomplished by first dividing the shape into canonical geometries and then super-positioning contributions of each canonical geometry at observation point.

Numerical methods such as FDTD [8], MoM [9] and FEM [10] can also be used to analyze diffracted fields starting from Rayleigh region ($\lambda >> l$; l : maximum length of target). The upper frequency limit depends on the computational resources but today's high speed, large memory computers enable us to analyze diffraction mechanism up to the beginning of the optical scattering region ($l \le 10\lambda$). Time domain based numerical methods also improves our understanding of diffraction phenomena because they enable to analyze diffraction step by step in time.

1.2. Contributions

The work discussed in this dissertation advances numerical diffraction theory by introducing three novel time domain based diffraction models: double tip diffraction model [11], soft-hard strip diffraction model [12] and time domain fringe current model [13]. Currently there are no exact solution exists for introduced models. The models are derived on specific two-dimensional (2D) geometries by using FDTD method. MoM method is used to validate proposed diffracted models. The following section describes the organization of each of the topics within this dissertation.

1.3. Organization of Dissertation

The remaining chapters of this thesis are outlined as follows:

Chapter 2 reviews fundamentals of electromagnetic theory including boundary conditions, time-harmonic fields and wave equations. Next, it introduces the concept of radar cross section and scattering mechanisms. The chapter continues with brief information about high frequency asymptotic methods; geometric optics (GO), physical optics (PO), geometrical theory of diffraction (GTD) and physical theory of diffraction (PTD). Finally,

it concludes with a description of most used numerical electromagnetic methods; MoM, FEM and FDTD. Here, we dwell on mostly FDTD method because all the diffraction models introduced by this thesis are derived with this method.

Chapter 3 presents one of the main contributions of this dissertation: Double tip diffraction model [11]. It starts with the introduction of the problem and its geometry. FDTD based diffraction model is next introduced and necessary steps that are needed to extract diffracted fields from total fields are explained. Afterwards, MoM-based diffraction model is presented. Finally, several examples and comparisons are shown to prove validity of proposed model.

Chapter 4 presents another novel diffraction model: Diffraction modeling by a soft-hard strip [12]. First, the problem geometry is introduced; a strip having soft boundary condition on one of its faces and hard boundary condition on the other. Afterwards, FDTD based diffraction model is explained step by step. Although, MoM method has been available for this structure we also briefly described it for the sake of completeness. Finally, the validity of the proposed FDTD based diffraction model is proved with the comparisons of MoM model.

Chapter 5 describes time domain modeling of fringe waves around perfectly reflecting wedge geometry [13]. A novel FDTD approach is first introduced to obtain fringe currents on the surface of the wedge. The fringe waves are then calculated from fringe currents via well-known radiation integrals [14]. The chapter concludes with several examples and comparisons against existing MoM model [15] to illustrate validity of proposed method.

Although each chapter has its own concluding section, we summarize our work and give directions for future work in *Chapter 6*.

2. BACKGROUND

2.1. Overview of Electromagnetics

2.1.1. Maxwell's Equations

Electromagnetic phenomena are governed by a set of four vector equations known as Maxwell's equations. Differential forms of these equations for time-varying fields are given by (2.1)-(2.4):

$$\nabla \cdot \mathbf{D} = q_{ev} \tag{2.1}$$

$$\nabla \cdot \mathbf{B} = q_{mv} \tag{2.2}$$

$$\nabla x \mathbf{E} = -\mathbf{M} - \frac{\partial \mathbf{B}}{\partial t} \tag{2.3}$$

$$\nabla x \mathbf{H} = \mathbf{J} + \frac{\partial \mathbf{D}}{\partial t} \tag{2.4}$$

where **D** is electric flux density (C/m^2), **B** is magnetic flux density (Wb/m^2), **E** is electric field intensity (V/m), **H** is magnetic field intensity (A/m), **J** is electric current density (A/m^2), **M** is magnetic current density (W/m^2), q_{ev} is volume electric charge density (C/m^3) and q_{mv} is volume magnetic charge density (Wb/m^3). Equations (2.1)–(2.4) are known as Gauss' law, magnetic Gauss' law, Maxwell-Faraday law and Ampere law respectively. In addition to the four Maxwell's equations, there is an additional equation relating the electrical charge density to the electrical current density. This equation is also known as continuity equation and expressed by:

$$\nabla \cdot \mathbf{J} = -\frac{\partial q_{ev}}{\partial t} \tag{2.5}$$

For problems that possess symmetry, it is more convenient to use integral form of Maxwell equations. These are obtained from differential form by utilizing Stoke's and divergence theorems given in (2.6) and (2.7) respectively:

$$\oint_C \mathbf{A} \cdot \mathbf{dl} = \iint_S (\nabla \times \mathbf{A}) \cdot \mathbf{ds} \tag{2.6}$$

$$\oiint_S \mathbf{A}\cdot\mathbf{ds} = \iiint_V (\nabla\cdot\mathbf{A})\,dv \tag{2.7}$$

Taking surface integral of both sides of (2.3) and (2.4) and applying Stoke's theorem yields integral form of Faraday and Amperes law which are given in (2.8) and (2.9):

$$\oint_C \mathbf{E}\cdot\mathbf{dl} = -\frac{\partial}{\partial t}\iint_S \mathbf{B}\cdot\mathbf{ds} \tag{2.8}$$

$$\oint_C \mathbf{H}\cdot\mathbf{dl} = \iint_S \mathbf{J}\cdot\mathbf{ds} + \frac{\partial}{\partial t}\iint_S \mathbf{D}\cdot\mathbf{ds} \tag{2.9}$$

The other two Maxwell equations can be obtained in integral form by taking volume integral of both sides of (2.1) and (2.2) and then applying divergence theorem. These are also given in equations (2.10) and (2.11):

$$\oiint_S \mathbf{D}\cdot\mathbf{ds} = \iiint_V q_{ev}\,dv \tag{2.10}$$

$$\oiint_S \mathbf{B}\cdot\mathbf{ds} = \iiint_V q_{mv}\,dv \tag{2.11}$$

Similarly, integral form of continuity equation can be obtained by utilizing divergence theorem as:

$$\oiint_S \mathbf{J}\cdot\mathbf{ds} = -\frac{\partial}{\partial t}\iiint_V q_{ev}\,dv. \tag{2.12}$$

The relationship between electric flux density **D** and electric field intensity **E** and similarly magnetic flux density **B** and magnetic field intensity **H** are governed by constitutive equations given in (2.13) and (2.14):

$$\mathbf{D} = \epsilon\mathbf{E} \tag{2.13}$$

$$\mathbf{B} = \mu\mathbf{H} \tag{2.14}$$

where ϵ is the permittivity, and μ is the permeability of the medium. In free space they are expressed as:

$$\epsilon = \epsilon_0 \approx 8.85x10^{-12}\ (Farad/meter) \tag{2.15}$$

$$\mu = \mu_0 = 4\pi x10^{-7}\ (Henry/meter) \tag{2.16}$$

2.1.2. Boundary Conditions

The differential forms of Maxwell equations given in (2.1)-(2.4) are not valid in regions where the parameters of the media changes abruptly. In other words, partial derivatives in differential form of Maxwell equations have meaning only if the medium is continuous. At points of discontinuity of the material properties, the field behavior is governed by BCs which are expressed by (2.17)-(2.20):

$$-\mathbf{n}\times(\mathbf{E_2}-\mathbf{E_1}) = \mathbf{M_s} \tag{2.17}$$

$$\mathbf{n}\times(\mathbf{H_2}-\mathbf{H_1}) = \mathbf{J_s} \tag{2.18}$$

$$\mathbf{n}\cdot(\mathbf{D_2}-\mathbf{D_1}) = q_{es} \tag{2.19}$$

$$\mathbf{n}\cdot(\mathbf{B_2}-\mathbf{B_1}) = q_{ms} \tag{2.20}$$

where the subscripts 1 and 2 are used for fields located in medium 1 and 2 and **n** is the unit vector normal to the boundary. These equations state that in source-free regions of space, the tangential components of electric and magnetic field are continuous whereas normal components of electric and magnetic fields are discontinuous by amount of ϵ_1/ϵ_2 and μ_2/μ_1 respectively.

2.1.3. Time-Harmonic Fields

Time-harmonic fields are those fields whose time variations are of cosinusoidal form. Assuming that fields have a time dependence $e^{j\omega t}$, the instantaneous fields can be related with their complex forms by:

$$\mathbf{A}(x,y,z,t) = \mathrm{Re}\left[\tilde{\mathbf{A}}(x,y,z)e^{j\omega t}\right] \tag{2.21}$$

where $\tilde{\mathbf{A}}$ is complex form. For such time-harmonic fields, the time-derivative in Maxwell equations are replaced simply by $j\omega$ and can be re-written as:

$$\nabla\times\tilde{\mathbf{E}} = -\tilde{\mathbf{M}}_i - j\omega\tilde{\mathbf{B}} \tag{2.22}$$

$$\nabla\times\tilde{\mathbf{H}} = \tilde{\mathbf{J}}_\mathbf{i} + j\omega\tilde{\mathbf{D}} \tag{2.23}$$

$$\nabla \cdot \tilde{\mathbf{D}} = q_{ev} \tag{2.24}$$

$$\nabla \cdot \tilde{\mathbf{B}} = q_{mv} \tag{2.25}$$

2.1.4. Wave Equations

Maxwell's equations given by (2.1)-(2.4) or (2.22)-(2.25) are first-order coupled partial differential equations, i.e. calculation of electric field requires knowledge about magnetic field and vice versa. These coupled equations can be transformed to uncoupled equations by increasing their order. This can be accomplished by first taking the curl of (2.3) and (2.4) and then applying the vector identity given by:

$$\nabla \times \nabla \times \mathbf{A} = \nabla(\nabla \cdot \mathbf{A}) - \nabla^2 \mathbf{A} \tag{2.26}$$

Substituting equations (2.1) and (2.2) into resulting equation yields the following second-order uncoupled equations which are also known as wave equations:

$$\nabla^2 \mathbf{E} = \nabla \times \mathbf{M} + \mu \frac{\partial \mathbf{J}}{\partial t} + \frac{1}{\epsilon} \nabla q_{ev} + \mu\sigma \frac{\partial \mathbf{E}}{\partial t} + \mu\epsilon \frac{\partial^2 \mathbf{E}}{\partial t^2} \tag{2.27}$$

$$\nabla^2 \mathbf{H} = -\nabla \times \mathbf{J} + \sigma \mathbf{M} + \frac{1}{\mu} \nabla q_{mv} + \epsilon \frac{\partial \mathbf{M}}{\partial t} + \mu\sigma \frac{\partial \mathbf{H}}{\partial t} + \mu\epsilon \frac{\partial^2 \mathbf{H}}{\partial t^2} \tag{2.28}$$

In source-free and lossless regions ($\mathbf{J} = \mathbf{M} = q_{ev} = q_{mv} = \sigma = 0$), (2.27) and (2.28) can be re-written as:

$$\nabla^2 \mathbf{E} = \mu\epsilon \frac{\partial^2 \mathbf{E}}{\partial t^2} \tag{2.29}$$

$$\nabla^2 \mathbf{H} = \mu\epsilon \frac{\partial^2 \mathbf{H}}{\partial t^2}. \tag{2.30}$$

Similar wave equations can be obtained for time-harmonic fields by replacing partial derivatives in (2.27)-(2.30) by $\partial / \partial t = j\omega$, $\partial^2 / \partial t^2 = -\omega^2$.

2.2. Radar Cross Section

Radar cross section (RCS) is a measure of reflective strength of a target which is defined by IEEE as 4π times the ratio of the power per unit solid angle scattered in a specified direction to the power per unit are in a plane wave incident on the scatterer from specified direction. Mathematically it is expressed as:

$$\sigma = \lim_{R\to\infty} 4\pi R^2 \frac{|\mathbf{E_s}|^2}{|\mathbf{E_i}|^2} \tag{2.31}$$

When electromagnetic wave sent by radar transmitter hits an object, currents are induced on the surface of the body and even within its volume if the object is not made of perfectly conducting material. These induced currents give rise to scattered fields which are radiated back and detected by radar receiver. A typical radar scenario is pictured at Fig. 2.1. According to the arrangement of transmitter and receiver, radar systems can be categorized into two groups: mono-static and bi-static. Mono-static radars use the same antenna for transmitter and receiver. Most radar systems works in mono-static arrangement because of their compactness. Bi-static radars use separate antennas located in two different locations for transmitter and receiver. It is possible to obtain larger RCS with bi-static arrangement because most RCS reduction techniques consider mono-static arrangement.

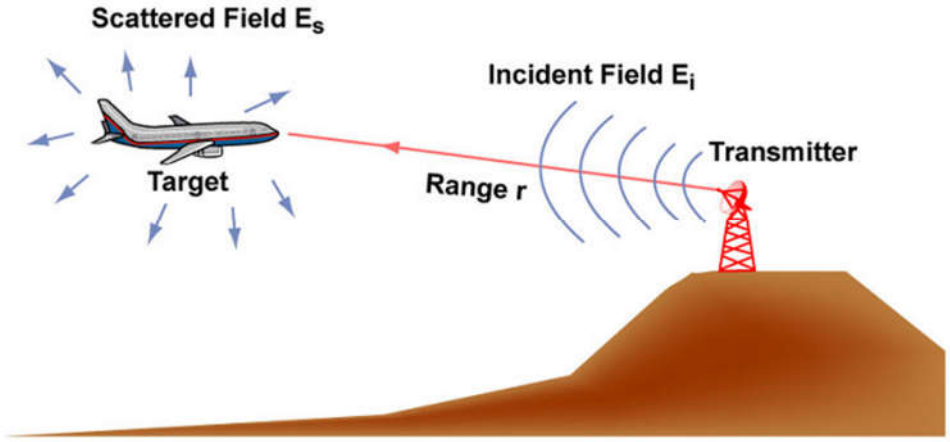

Figure 2.1 Typical radar scenario [16]

Scattering characteristics of the target not only depend on the target's geometry and its material properties but also the frequency of incident wave. There are three frequency regimes in which RCS of the target behave differently: Rayleigh, resonance and optical.

These frequency regimes are illustrated in Fig. 2.2 for RCS of sphere of radius a. In Rayleigh region where the target size is small compared with wavelength, the current induced on the target is approximately constant. RCS increases with frequency and does not depend on the shape of target. In resonance region, target size becomes comparable with wavelength and the current induced on the target have considerable phase variations. The target contributes to its RCS as a whole. In optical region, target size is large compared with the wavelength and the RCS of the target approaches to physical area of the target. Measurement of RCS is a very time consuming and expensive process. Instead, high frequency and numerical techniques can be used to calculate RCS approximately at initial steps of target design. High frequency methods such as GO, PO, PTD and GTD are widely used in optical region. Numerical methods such as MoM, FDTD and FEM become computationally expensive as the target size increases; therefore they are used generally in Rayleigh and resonance region.

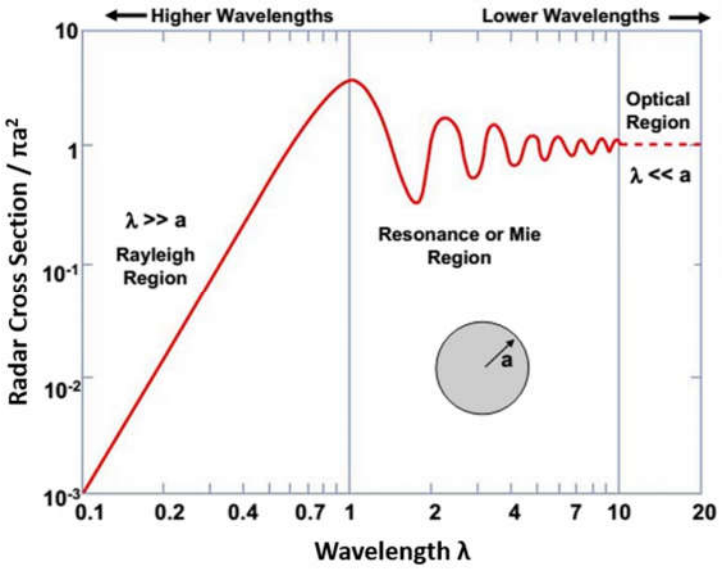

Figure 2.2 RCS of a sphere [16]

2.3. Scattering Mechanisms

Scattering field is comprised as a result of various scattering mechanisms. Fig. 2.3 shows various scattering mechanisms formed on combat aircraft. Specular reflection is mirror-like reflection of wave from flat and smooth surfaces. This scattering mechanism is governed by well-known Snell's law i.e. the angle of incidence is equal to the angle of

reflection ($\theta_i = \theta_r$), and contributes significantly to the target RCS especially in optical region. Multiple reflections are possible if multiple surfaces are present. For example, electromagnetic wave can reflect from vertical stabilizer of an aircraft, hit horizontal stabilizer and then return to radar receiver by reflecting from that surface. Diffraction arises from electrically small discontinuities such as edges, tips and vertexes. Diffracted fields emerge in all directions hence they exists even in the shadow region where the incident field is zero. Diffracted fields contribute significantly to scattered field especially in lower and middle resonance regions. As the wavelength becomes smaller than object size, diffracted fields become less intense than reflected fields. An incident electromagnetic wave leads to traveling surface waves which propagate along flat smooth surfaces. Upon reaching a surface discontinuity such as edges or vertex, part of the surface wave reflects and propagates back towards the radar. They have significant contribution to target's RCS for surface grazing angles less than $30°$ in resonance and optical region [17].

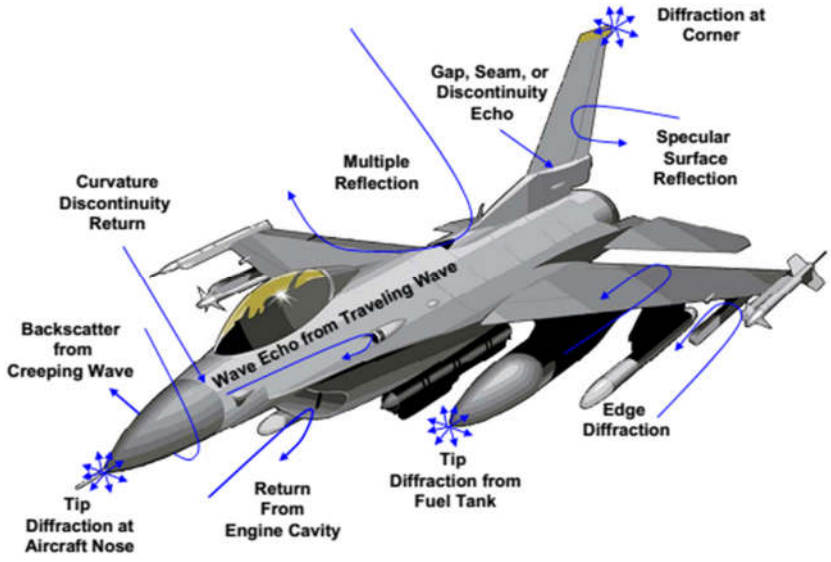

Figure 2.3 Scattering mechanisms [16]

Creeping wave is actually traveling wave which circulates around the smooth closed shapes such as sphere. Together with diffracted fields, these are the only waves that exist in shadow region. They are also responsible for the oscillations in resonance region of RCS of the sphere as shown at Fig. 2.2. Creeping waves may not be taken into account when radius of curvature is greater than five times the wavelength. Hence their contribution is only significant up to middle of resonance region.

Any discontinuity on the object surface such as curvature, gap and seam can been seen as an echo source. Their effects generally masked with other scattering mechanisms discussed so far. Hence, they are not taken into account generally in designing low observable targets.

2.4. Analytic Methods in Electromagnetics

2.4.1. Geometric Optics

Geometric optics (GO), also known as ray optics, is a high frequency asymptotic technique used to analyze electromagnetic wave scattering from objects whose dimensions are very large compared to wavelength ($l >> \lambda$). Principles of GO are derived from the treatment of light and given as:

1. Light travels in the form of rays.
2. Light rays satisfy Snell's law of reflection and refraction.
3. Light rays travel along the path of least time e.g. they travel as straight lines in homogenous medium (Fermat's principle).
4. Light intensity between two points is governed by the conservation of energy flux in a tube of rays. [14]

GO is very useful in analysis of reflected and refracted fields in optical region. Wave nature of light is not taken into account because postulates of this method is derived in the limit when wavelength goes to zero (or frequency is infinite). As a result, wave phenomenon such as interference, diffraction and dispersion can't be modeled with this method. In GO, wave direction is specified by a vector normal to the eikonal surfaces which are expressed by the solution of (2.32):

$$\left|\nabla(x,y,z)\right| = \left|\frac{\partial \Psi}{\partial x}\right|^2 + \left|\frac{\partial \Psi}{\partial y}\right|^2 + \left|\frac{\partial \Psi}{\partial z}\right|^2 = n(x,y,z) \tag{2.32}$$

where $\psi(x,y,z)$ is eikonal function and $n(x,y,z)$ is refractive index. If the refractive index of the medium is constant i.e. homogenous medium, then the wave propagates in a direction specified by straight lines. In this case, eikonal surfaces may be parallel planes or concentric spheres as shown in Fig. 2.4 [18]. In order to use GO in electromagnetic problems, amplitude, polarization and phase concepts needs to be introduced.

Amplitude Relation

Amplitude relationship of rays is obtained by imposing the conservation of energy flux in a tube of rays. This can be demonstrated with the aid of Fig.2.5. Here, the light radiated from point source constitutes a ray tube which has cross sectional areas dA_0 and dA at some reference points. Radiation densities at these points are related by:

$$S_1 dA_0 = SdA \tag{2.33}$$

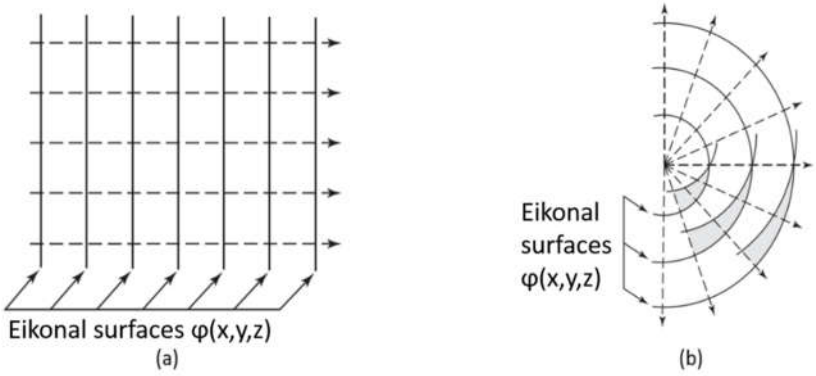

Figure 2.4 Eikonal surfaces in homogenous medium (a) Plane wave (b) Spherical wave [14]

In electromagnetic theory, radiation density is also related with electric field in the far zone (distance from source $> \frac{2D^2}{\lambda^2}$ where D is largest dimension of the radiator) by:

$$S(r,\theta,\phi) = \frac{1}{2\eta}\left|\mathbf{E}(r,\theta,\varphi)\right|^2 \tag{2.34}$$

where η is wave impedance and $\mathbf{E}(r,\theta,\varphi)$ is electric field. Combining (2.33) and (2.34) yields the amplitude relation for GO:

$$\frac{|\mathbf{E}|}{|\mathbf{E}_0|} = \sqrt{\frac{dA_0}{dA}} \tag{2.35}$$

For cylindrical eikonal surfaces (2.35) will be proportional to the distance (radii of curvature) from source point:

$$\frac{|\mathbf{E}|}{|\mathbf{E}_0|} = \sqrt{\frac{dA_0}{dA}} = \frac{\rho_0}{\rho_0 + s} \tag{2.36}$$

If the eikonal surfaces are planar, then R_0 and R_1 can be assumed to be infinite and as a result, (2.35) will be equal to one.

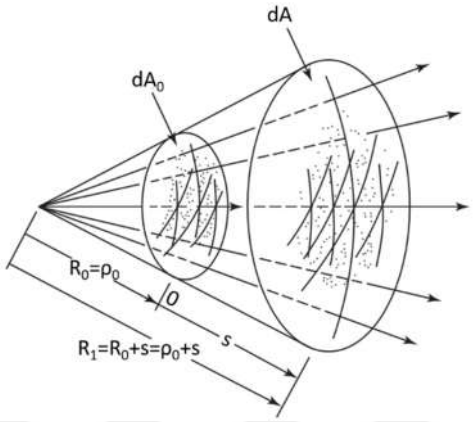

Figure 2.5 Tube of rays [14]

Phase and Polarization Relation

Phase and polarization relation for GO is obtained via Luneberg–Kline high frequency expansion [19] that is given by (2.37) with the aid of Fig. 2.5:

$$\mathbf{E}(s) = \mathbf{E_0}'(0)e^{j\phi_0(0)}\sqrt{\frac{\rho_0}{\rho_0 + s}}e^{-j\beta s} \tag{2.37}$$

Here, the term $\mathbf{E_0}'(0)e^{j\phi_0(0)}$ represents the value of complex electric field at reference point s=0, $\sqrt{\frac{\rho_0}{\rho_0 + s}}$ represents the spatial attenuation due to spreading of wavefront and $e^{-j\beta s}$ represents the phase variation. The polarization of the field is determined by the vector $\mathbf{E_0}'(0)$. Applications of GO in electromagnetic problems can be found in [20].

2.4.2. Physical Optics

Physical optics, introduced by Macdonald (1912), has long been applied to analyze scattering fields from electrically large ($d \geq 10\lambda$) convex bodies. In contrast to GO, the wave nature is preserved in this method and wave phenomenon such as diffraction and interference are modeled. When electromagnetic waves encounter an object, surface or volume currents are induced depending on the electrical properties of the object. These

induced currents are then used in vector potential equations (2.38)-(2.40) to find radiated fields everywhere. PO scattered fields are also calculated in the same way.

$$\mathbf{E}_{\mathbf{A}} = -j\omega\mathbf{A} \text{ (for } \theta \text{ and } \varphi \text{ components only)} \tag{2.38}$$

$$\mathbf{H}_{\mathbf{A}} = \frac{1}{\eta}\mathbf{a}_{\mathbf{r}} \times \mathbf{E}_{\mathbf{A}} \text{ (for } \theta \text{ and } \varphi \text{ components only)} \tag{2.39}$$

$$\mathbf{A} = \frac{\mu}{4\pi}\iint_S \mathbf{J}_{\mathbf{s}}(x', y', z')\frac{e^{j\beta R}}{R}\mathbf{ds'} \tag{2.40}$$

In this method, induced currents are assumed as if they are induced on infinite tangent plane and calculated from the incident electrical and magnetic fields obtained by using GO approximation as:

$$\mathbf{J}_{\mathbf{s}} = 2\mathbf{n} \times \mathbf{H}_{\mathbf{GO}}^{\mathbf{inc}} \tag{2.41}$$

These currents are assumed to be non-zero only in the illuminated portion of the body and set to zero in the shadow region as shown in Fig. 2.6. PO currents are also known as uniform currents because magnitude spectrum of currents induced on infinite-plane is uniform. Similar to GO, PO is most accurate at specular direction but it also gives good results in the vicinity of forward scattering direction in which GO is not applicable.

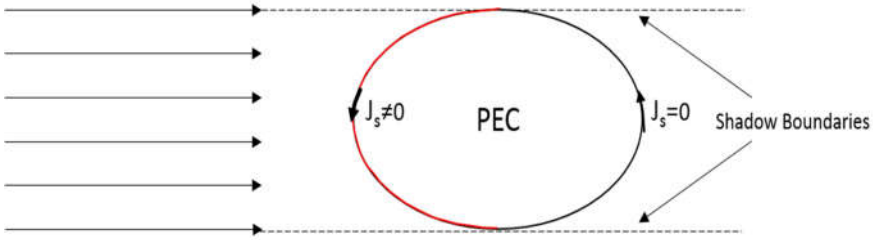

Figure 2.6 Illuminated and Shadow Regions of surface for application of PO.

One of the drawbacks of PO is that it is insensitive to polarization i.e. scattering field is the same for each polarization. In addition to this, its accuracy is poor at points near to discontinuities such as edges, tips and corners because diffraction mechanism is not modeled correctly. Actually, the diffraction modeled in PO is due to abrupt termination of currents near discontinuities and this is not true in reality.

2.4.3. Geometrical Theory of Diffraction

Geometrical Theory of Diffraction (GTD) is introduced by Keller to remove inefficiencies of GO in incident and shadow regions [3]. Besides the usual rays, diffracted ray concept is introduced with GTD. Diffracted rays lie on the surface of cone called as Keller's cone whose half-angle is equal to the angle which incident ray makes with point of discontinuity on the object surface as shown at Fig. 2.7.

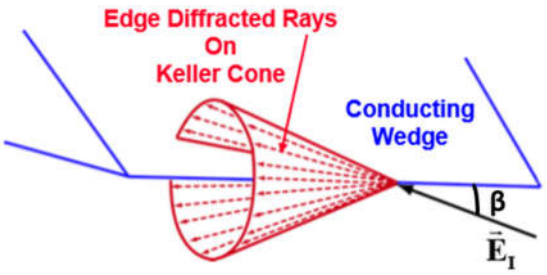

Figure 2.7 Keller cone in GTD [16]

According to GTD, total fields are formed by the GO fields plus diffracted fields and expressed as:

$$\begin{aligned} \mathbf{E} &= \mathbf{E}^{\mathbf{GO}} + \mathbf{E}^{\mathbf{GTD}} \\ \mathbf{H} &= \mathbf{H}^{\mathbf{GO}} + \mathbf{H}^{\mathbf{GTD}} \end{aligned} \tag{2.42}$$

where $\mathbf{E}^{\mathbf{GO}}$, $\mathbf{H}^{\mathbf{GO}}$ are GO total fields and $\mathbf{E}^{\mathbf{GTD}}$, $\mathbf{H}^{\mathbf{GTD}}$ are diffracted fields derived by GTD. The postulates of the GTD are the same as those of GO but also include following ones for diffracted fields:

1. Diffracted rays satisfy Fermat's principle.
2. Diffracted rays are linearly related to the incident field at diffraction point by diffraction coefficient.

As a consequence of the postulates given above, diffracted rays are expressed with the aid of Fig. 2.8 as:

$$\mathbf{E_d}(s) = \mathbf{E_i}(Q_D) \cdot \overline{\mathbf{D}}\, A(s', s) e^{-j\beta s} \tag{2.43}$$

where $\mathbf{E}_d(s)$, $\mathbf{E}_i$ are diffracted and incident fields and $\overline{\mathbf{D}}$ is diffraction coefficient (usually dyadic) derived from the appropriate canonical problem by subtracting GO solution from

exact total field solution [14]. The term $A(s',s)$ is called as spatial attenuation factor and expressed by (2.44) for plane, cylindrical and spherical waves:

$$A(s',s)=\begin{cases}\dfrac{1}{\sqrt{s}} & \text{for plane wave}\\ \dfrac{1}{\sqrt{\rho}},\ \rho=s\sin\beta_0 & \text{for cylindrical wave}\\ \sqrt{\dfrac{s'}{s(s+s')}} & \text{for spherical wave}\end{cases} \tag{2.44}$$

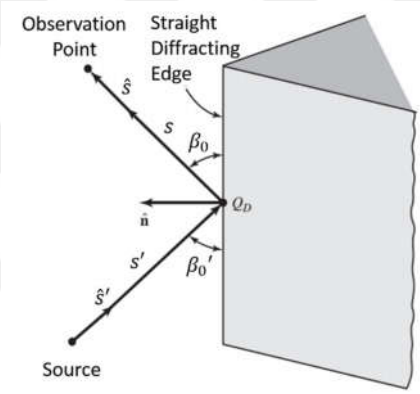

Figure 2.8 Edge diffraction scenario for [14]

GTD can be used to analyze scattered fields from complex shapes. To accomplish this, complex shape is partitioned into canonical geometries. The total field is then calculated via superposition of the fields formed by each canonical geometry. Diffraction coefficient for various canonical geometries as well as detailed explanation of GTD can be found in [3], [14] and [21].

2.4.4. Physical Theory of Diffraction

Physical theory of diffraction is a current based high frequency asymptotic method and can be seen as an extension of PO. According to PTD, induced currents are formed by uniform and non-uniform components. Uniform components are actually physical optics currents which are assumed to be induced on an infinite tangent plane. Non-uniform (fringe) currents, on the other hand, are formed due to the discontinuities of object surface such as edges, tips, corners and any other inhomogeneities of the material. Fig. 2.9 demonstrates

the currents induced on perfectly reflecting tangent plane. As can be seen, non-uniform currents are concentrated in the vicinity of discontinuity.

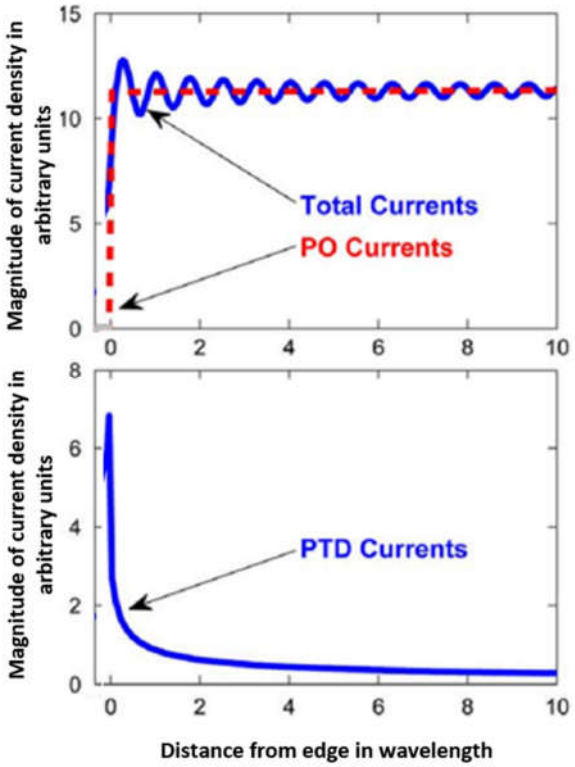

Figure 2.9 Total, uniform (PO) and non-uniform (PTD) currents on half-plane

In PTD, total scattered field is expressed by the sum of the field radiated by uniform (PO) and non-uniform (fringe) currents as:

$$\begin{aligned} \mathbf{E} &= \mathbf{E}^{PO} + \mathbf{E}^{fringe} \\ \mathbf{H} &= \mathbf{H}^{PO} + \mathbf{H}^{fringe} \end{aligned} \tag{2.45}$$

In accordance with (2.45) fringe fields are found by subtracting PO solution from exact total fields i.e. fields determined by canonical problems. As stated previously, diffraction is considered a local phenomenon in high frequencies. Hence, complex targets can be partitioned into canonical geometries to analyze radiated scattered field with PTD. The drawback of this approach is that interactions between discontinuities are difficult to model because canonical problems with multiple discontinuities are limited. The interested reader is referred to [5], [6] and [22] for further information.

2.5. Numerical Methods in Electromagnetics

2.5.1. Method of Moments

Integral equations are encountered very frequently in electromagnetics, e.g. scattered fields are found from current density via well-known radiation equations [14] that are actually an integral equations. Method of moments is an integral equation based frequency domain method and particularly used in antenna radiation and wave scattering problems. In this method, integral equation is converted to matrix equation by representing unknown function as the sum of basis functions. MoM can be formulated mathematically by:

$$L\mathbf{F} = \mathbf{g} \tag{2.46}$$

where the function **g** is known excitation (e.g. incident electric or magnetic field), **F** is the unknown function (e.g. current density) which needs to be determined and L is a linear operator (e.g integral). Expanding unknown function **F** in series form yields:

$$\mathbf{F} = \sum_{m}^{N} \alpha_m \mathbf{F_m}. \tag{2.47}$$

Here, α_m 's are the unknown coefficients and $\mathbf{F_m}$'s are the known basis functions. Substituting (2.47) into (2.46) and using the linearity of operator L, one can obtain:

$$L\mathbf{F} = L\sum_{m}^{N} \alpha_m \mathbf{F_m} = \sum_{m}^{N} \alpha_m L\mathbf{F_m} = \mathbf{g}. \tag{2.48}$$

Equation (2.48) has N unknowns and can be solved if it is transformed into a system of N linearly independent equations with N unknowns. This can be accomplished by multiplying both sides of (2.48) by a set of testing functions T_is and taking inner product of (2.48) against each T_i:

$$\sum_{m}^{N} \alpha_m \left\langle \mathbf{T_i}, L\mathbf{F_m} \right\rangle = \left\langle \mathbf{T_i}, \mathbf{g} \right\rangle \;\; i = 1, 2, ..N \tag{2.49}$$

The testing functions T_i s are generally selected to be equal to basis functions i.e. $F_i = T_i$ and this selection is known as Galerkin method. Equation (2.49) can be re-written in matrix form as:

$$[A][\alpha] = [G] \tag{2.50}$$

where

$$A_{mn} = \langle \mathbf{T_m}, L\mathbf{F_n} \rangle \tag{2.51}$$

$$G_m = \langle \boldsymbol{T_m}, \boldsymbol{g} \rangle \tag{2.52}$$

The unknown expansion coefficients α_ms are then found by:

$$[\alpha] = [A]^{-1}[G] \tag{2.53}$$

in case of the matrix [A] is not equal to zero, i.e. [A] is not non-singular. Once expansion coefficients are known, the solution for **F** is found by (2.47). It is important to choose basis functions which approximate to the exact solution with as less as possible terms. For example, if the unknown function **F** oscillates throughout a particular region, using pulse functions may not be a good choice [23]. The most common basis functions are pulse functions, triangular functions and piecewise sinusoidal functions. These are illustrated in Fig. 2.10.

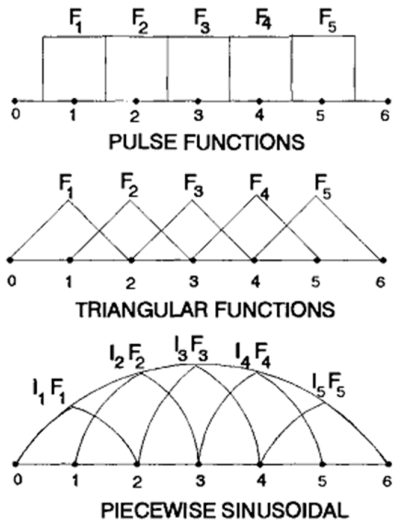

Figure 2.10 Base functions used in MoM [24].

The implementation of MoM requires order of N^3 operations and order of N^2 computer memory storage. Detailed information and application of MoM to various problems can be found in [9], [23] and [25].

2.5.2. Finite Element Method

Finite element method is a very popular frequency domain based numeric method used to solve electromagnetic boundary value problems. In this method, the whole simulation region is divided into smaller sub-regions, called elements. For two-dimensional problems, the most common element type is triangle and for three-dimensional problems the most common element types are tetrahedron and hexahedron. These are illustrated in Fig.2.11.

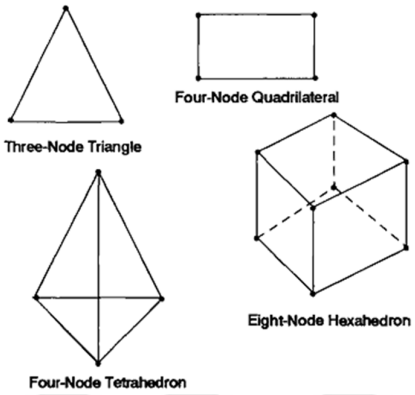

Figure 2.11 Elements used in FEM [24]

The unknown quantity (e.g. field, current, voltage, etc.) in an element is interpolated by node values using shape (interpolation) functions. For example, the field inside a triangular element "e" is expressed by:

$$F^e(x,y) = N_1^e F_1^e + N_2^e F_2^e + N_3^e F_3^e \tag{2.54}$$

where F_1, F_2, F_3 are the field values at the nodes of triangle and N_1, N_2, N_3 are the shape functions of nodes. Shape functions should be equal to one at corresponding node and zero at another node e.g. $N_e^1 = 1$ at node 1 and $N_e^1 = 1$ at node 2. The next step is to obtain linear equations for a single element from the differential equation. This is accomplished by using either variational or weighted-residual metho. In the variational method, linear equations are obtained by minimizing a functional which represents the energy associated with the problem. This process involves taking partial derivatives of the functional with respect to each of the dependent variables and setting them to zero [26]. The weighted-residual method works directly on the differential equation and does not require any functional. The residual is formed by collecting all terms of the differential equation at one side. It is then multiplied by appropriate weight (testing) function and integrated over the

domain of the element. If the weight function is selected to be same as the shape function then this selection is known as Galerkin's method. Once linear equations for single element is obtained, global matrix system of equations that describe the solution of the problem needs to be assembled. Finally, appropriate BC e.g. Dirichlet is imposed to the assembled global matrix system and it is solved via linear algebra techniques such as Lower Upper (LU) decomposition.

The memory required for the FEM method is proportional to number of unknowns or elements O(N). This is very low in contrast to other numerical methods such as FDTD and MoM. In addition to this, complex structures are easily modeled with FEM without need to change the procedure. Similar to FDTD, implementation of perfectly matched layers (PEC) or absorbing BCs (ABC) are required to use this method in radiation and scattering problems. The reader is referred to [10], [26], [27] and [28] for detailed explanation of FEM and its applications.

2.5.3. Finite Difference Time Domain Method

FDTD method, introduced by Yee in 1966 [8], is arguably the simplest of numerical methods used to solve electromagnetic problems. It is based on simple formulations on time domain. Yee's idea was to divide simulation space into rectangular cells to form a grid and then solve differential form of the Maxwell's equations around these cells by using second-order central differences. FDTD has been used to solve various types of problems including scattering, radar cross section, cell phone radiation over human head and geological applications. Although being time domain method, frequency domain responses can also be obtained via Fourier transform. In this section we briefly explain FDTD method because the majority of the work done in this thesis is performed by this method.

Since FDTD is based on discretizing time and simulation space, it is useful to start with the concept of numerical derivative. Taylor series expansion of the multivariable function $f(x,t)$ around the specified time t_0 can be written as:

$$f(x,t) = f(x,t_0) + (t-t_0)\frac{\partial f(x,t_0)}{\partial t} + \frac{1}{2}(t-t_0)^2\frac{\partial^2 f(x,t_0)}{\partial^2 t} + \ldots \tag{2.55}$$

If the function $f(x,t)$ is sampled in time with Δt intervals we can write (2.55) as follows:

$$f\left(x,t_0+\Delta t\right)=f\left(x,t_0\right)+\left(\Delta t\right)\frac{\partial f\left(x,t_0\right)}{\partial t}+\frac{1}{2}\left(\Delta t\right)^2\frac{\partial^2 f\left(x,t_0\right)}{\partial t^2}+\ldots \tag{2.56}$$

After re-arranging terms the following expression is obtained for time-derivative:

$$\frac{\partial f(x,t_0)}{\partial t}=\frac{(f(x,t_0+\Delta t)-f(x,t_0))}{\Delta t}-\frac{1}{2}\Delta t\frac{\partial^2 f(x,t_0)}{\partial t^2}-\ldots \tag{2.57}$$

Similar steps can be used to obtain expression for spatial derivative. The terms in the Taylor series extend to infinity and needs to be truncated at some point. Omitting the terms that contain the orders of Δt in (2.57) yields:

$$\frac{\partial(x,t_0)}{\partial t}\approx\frac{(f(x,t_0+\Delta t)-f(x,t_0))}{\Delta t} \tag{2.58}$$

This approximation is called first-order forward difference approximation of the derivative of the function $f(x,t)$ with respect to t. The term "first-order" comes from the fact that we omitted the terms multiplied by the orders of Δt starting from the first-order in the equation (2.57). The term "forward" comes from the fact that, one forward time $f(x,t_0+\Delta t)$ is used to evaluate derivative.

Similarly, the expansion of $f(x,t_0-\Delta t)$ around the point t_0 gives:

$$f(x,t_0-\Delta t)=f(x,t_0)-(\Delta t)\frac{\partial f(x,t_0)}{\partial t}+\frac{1}{2}(\Delta t)^2\frac{\partial^2 f(x,t_0)}{\partial t^2}-\ldots \tag{2.59}$$

Leaving the first-order derivative alone yields:

$$\frac{\partial f(x,t_0)}{\partial t}=\frac{(f(x,t_0)-f(x,t_0-\Delta t))}{\Delta t}+\frac{1}{2}\Delta t\frac{\partial^2 f(x,t_0)}{\partial t^2}-\ldots \tag{2.60}$$

Neglecting the terms multiplied with the powers of Δt in (2.60), first-order backward approximation of the derivative of the function $f(x,t)$ with respect to t is obtained:

$$\frac{\partial f(x,t_0)}{\partial t}\approx\frac{(f(x,t_0)-f(x,t_0-\Delta t))}{\Delta t} \tag{2.61}$$

The third most common form of numerical derivative is obtained by averaging the forward and backward difference expressions such that

$$f(x,t_0+\Delta t)-f(x,t_0-\Delta t)=2\Delta t\frac{\partial f(x,t_0)}{\partial t}+\frac{1}{3}(\Delta t)^3\frac{\partial^3 f(x,t_0)}{\partial t^3}-... \tag{2.62}$$

Rearranging terms in (2.62) yields the following expression:

$$\frac{\partial f(x,t_0)}{\partial t}=\frac{f(x,t_0+\Delta t)-f(x,t_0-\Delta t)}{2\Delta t}-\frac{(\Delta t)^2}{6}\frac{\partial^3 f(x,t_0)}{\partial t^3}+... \tag{2.63}$$

As can be observed from the above equation, there is no term multiplied with the first-order of Δt. The order of Δt starts from two and thus this scheme is called as second-order centered difference approximation. Numerical approximation of the derivative with this scheme is obtained in a similar manner by neglecting the terms that include powers of Δt and it is given by equation (2.64). The error introduced in this difference approximation is less than the first-order forward or backward difference approximations. For example, if the time step Δt is reduced to half of its value, the error reduced by a factor of four.

$$\frac{\partial f(x,t_0)}{\partial t}\approx\frac{f(x,t_0+\Delta t)-f(x,t_0-\Delta t)}{2\Delta t} \tag{2.64}$$

2.5.3.1. 3D FDTD Algorithm

As stated previously, Yee's algorithm approximates the derivatives in the differential form of Maxwell's equations (2.1)-(2.4) with second-order centered differences. Application of finite differences requires specifying spatial and temporal location of field components. Fig. 2.12 shows the spatial arrangement of field components in a cubical cell also known as Yee's cell. In this arrangement, electric fields are placed at the centers of the edges of Yee cell and magnetic fields are placed at the center of the faces of the Yee cell. In other words, magnetic field components are surrounded by four electric field components and electric field components are surrounded by four magnetic field components. Instead, one can rearrange Yee cell so that location of the magnetic and electric field components are interchanged. But first arrangement has advantage because of the fact that boundary conditions imposed on electric field are more commonly encountered than those for magnetic field. Therefore, placing mesh boundaries so that they pass through electric field

vectors is required with the first arrangement [29]. In addition to spatial arrangement, Yee assumed that magnetic field components are calculated at half time steps slightly after electric field components.

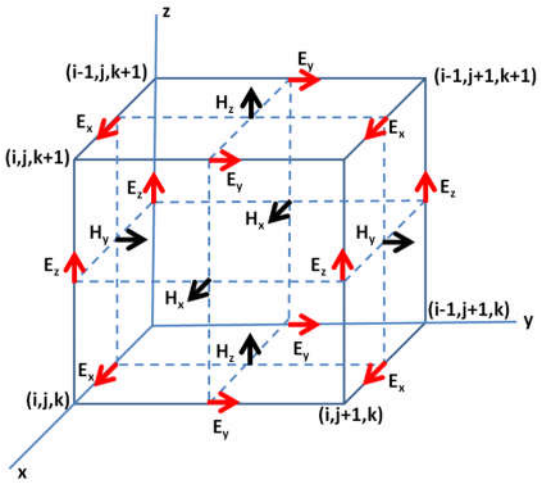

Figure 2.12 Yee Cell

Derivation of algorithm starts with the open form of Maxwell's curl equations e.g. Faraday law;

$$\nabla x\mathbf{E} = det\begin{vmatrix} i & j & k \\ \frac{\partial}{\partial x} & \frac{\partial}{\partial y} & \frac{\partial}{\partial z} \\ E_x & E_y & E_z \end{vmatrix} = \left(\frac{\partial E_z}{\partial y} - \frac{\partial E_y}{\partial z}\right)\vec{\mathbf{i}} + \left(\frac{\partial E_x}{\partial z} - \frac{\partial E_z}{\partial x}\right)\vec{\mathbf{j}} + \left(\frac{\partial E_y}{\partial x} - \frac{\partial E_x}{\partial y}\right)\vec{\mathbf{k}} = -\mu_0 \frac{\partial \mathbf{H}}{\partial t} \tag{2.65}$$

Here magnetic current density **M** and electric current density **J** are omitted. Equating corresponding components of i, j and k on each side of (2.65) yields the three coupled scalar equations:

$$\frac{\partial H_x}{\partial t} = \frac{1}{\mu}\left[\frac{\partial E_y}{\partial z} - \frac{\partial E_z}{\partial y}\right] \tag{2.66}$$

$$\frac{\partial H_y}{\partial t} = \frac{1}{\mu}\left[\frac{\partial E_z}{\partial x} - \frac{\partial E_x}{\partial z}\right] \tag{2.67}$$

$$\frac{\partial H_y}{\partial t} = \frac{1}{\mu}\left[\frac{\partial E_z}{\partial x} - \frac{\partial E_x}{\partial z}\right] \tag{2.68}$$

Repeating the same process for Ampere's law (2.4) yields:

$$\frac{\partial E_x}{\partial t} = \frac{1}{\epsilon}\left[\frac{\partial H_z}{\partial y} - \frac{\partial H_y}{\partial z}\right] \tag{2.69}$$

$$\frac{\partial E_y}{\partial t} = \frac{1}{\epsilon}\left[\frac{\partial H_x}{\partial z} - \frac{\partial H_z}{\partial x}\right] \tag{2.70}$$

$$\frac{\partial E_z}{\partial t} = \frac{1}{\epsilon}\left[\frac{\partial H_y}{\partial x} - \frac{\partial H_x}{\partial y}\right] \tag{2.71}$$

Derivatives of the equations (2.66)-(2.71) can be replaced by second-order centered differences. By doing so, the equations (2.72)-(2.77) are obtained for 3D FDTD algorithm

$$H_x\Big|_{i,j+\frac{1}{2},k+\frac{1}{2}}^{n+\frac{1}{2}} = H_x\Big|_{i,j+\frac{1}{2},k+\frac{1}{2}}^{n-\frac{1}{2}} + \frac{\Delta t}{\mu_{i,j+\frac{1}{2},k+\frac{1}{2}}}\left[\frac{E_y\Big|_{i,j+\frac{1}{2},k+1}^{n} - E_y\Big|_{i,j+\frac{1}{2},k}^{n}}{\Delta z} - \frac{E_z\Big|_{i,j+1,k+\frac{1}{2}}^{n} - E_z\Big|_{i,j,k+\frac{1}{2}}^{n}}{\Delta y}\right] \tag{2.72}$$

$$H_y\Big|_{i+\frac{1}{2},j,k+\frac{1}{2}}^{n+\frac{1}{2}} = H_y\Big|_{i+\frac{1}{2},j,k+\frac{1}{2}}^{n-\frac{1}{2}} + \frac{\Delta t}{\mu_{i+\frac{1}{2},j,k+\frac{1}{2}}}\left[\frac{E_z\Big|_{i+1,j,k+\frac{1}{2}}^{n} - E_z\Big|_{i,j,k+\frac{1}{2}}^{n}}{\Delta x} - \frac{E_x\Big|_{i+\frac{1}{2},j,k+1}^{n} - E_x\Big|_{i+\frac{1}{2},j,k}^{n}}{\Delta z}\right] \tag{2.73}$$

$$H_z\Big|_{i+\frac{1}{2},j+\frac{1}{2},k}^{n+\frac{1}{2}} = H_z\Big|_{i+\frac{1}{2},j+\frac{1}{2},k}^{n-\frac{1}{2}} + \frac{\Delta t}{\mu_{i+\frac{1}{2},j+\frac{1}{2},k}}\left[\frac{E_x\Big|_{i+\frac{1}{2},j+1,k}^{n} - E_x\Big|_{i+\frac{1}{2},j,k}^{n}}{\Delta y} - \frac{E_y\Big|_{i+1,j+\frac{1}{2},k}^{n} - E_y\Big|_{i,j+\frac{1}{2},k}^{n}}{\Delta x}\right] \tag{2.74}$$

$$E_x\Big|_{i+\frac{1}{2},j,k}^{n+1} = E_x\Big|_{i+\frac{1}{2},j,k}^{n} + \frac{\Delta t}{\epsilon_{i+\frac{1}{2},j,k}}\left[\frac{H_z\Big|_{i+\frac{1}{2},j+\frac{1}{2},k}^{n+\frac{1}{2}} - H_z\Big|_{i+\frac{1}{2},j-\frac{1}{2},k}^{n+\frac{1}{2}}}{\Delta y} - \frac{H_y\Big|_{i+\frac{1}{2},j,k+\frac{1}{2}}^{n+\frac{1}{2}} - H_y\Big|_{i+\frac{1}{2},j,k-\frac{1}{2}}^{n+\frac{1}{2}}}{\Delta z}\right] \quad (2.75)$$

$$E_y\Big|_{i,j+\frac{1}{2},k}^{n+1} = E_y\Big|_{i,j+\frac{1}{2},k}^{n} + \frac{\Delta t}{\epsilon_{i,j+\frac{1}{2},k}}\left[\frac{H_x\Big|_{i,j+\frac{1}{2},k+\frac{1}{2}}^{n+\frac{1}{2}} - H_x\Big|_{i,j+\frac{1}{2},k-\frac{1}{2}}^{n+\frac{1}{2}}}{\Delta z} - \frac{H_z\Big|_{i+\frac{1}{2},j+\frac{1}{2},k}^{n+\frac{1}{2}} - H_z\Big|_{i-\frac{1}{2},j+\frac{1}{2},k}^{n+\frac{1}{2}}}{\Delta x}\right] \quad (2.76)$$

$$E_z\Big|_{i,j,k+\frac{1}{2}}^{n+1} = E_z\Big|_{i,j,k+\frac{1}{2}}^{n} + \frac{\Delta t}{\epsilon_{i,j,k+\frac{1}{2}}}\left[\frac{H_y\Big|_{i+\frac{1}{2},j,k+\frac{1}{2}}^{n+\frac{1}{2}} - H_y\Big|_{i-\frac{1}{2},j,k+\frac{1}{2}}^{n+\frac{1}{2}}}{\Delta x} - \frac{H_x\Big|_{i,j+\frac{1}{2},k+\frac{1}{2}}^{n+\frac{1}{2}} - H_x\Big|_{i,j-\frac{1}{2},k+\frac{1}{2}}^{n+\frac{1}{2}}}{\Delta y}\right] \quad (2.77)$$

Field components are represented in compact form i.e. $H_x\Big|_{i,j+\frac{1}{2},k+\frac{1}{2}}^{n+\frac{1}{2}} = H_x(i, j+\frac{1}{2}, k+\frac{1}{2}, n+\frac{1}{2})$ is used. Here, superscript n is used for time step and subscript i, j, k is used for spatial location. Time step is explicit in FDTD algorithm i.e. magnetic fields are calculated before/after the electric fields. However, spatial step is implicit and fractions cannot be used as an array index in high-level programming languages. The following procedures should be followed to overcome this issue:

The indexes of the necessary H values should follow below rules when it comes to calculating E values:

- When the H index has a +1/2 assume its value 0
- When the H index has a -1/2 assume its value -1

The indexes of the necessary E values should follow below rules when it comes to calculating H values:

- When the E index has a -1/2 assume its value 0

- When the E index has a +1/2 assume its value +1

Selection of time step and spatial step requires specific attention in FDTD algorithm and this topic will be explained later in this chapter. A flowchart of complete FDTD algorithm is shown at Fig. 2.13.

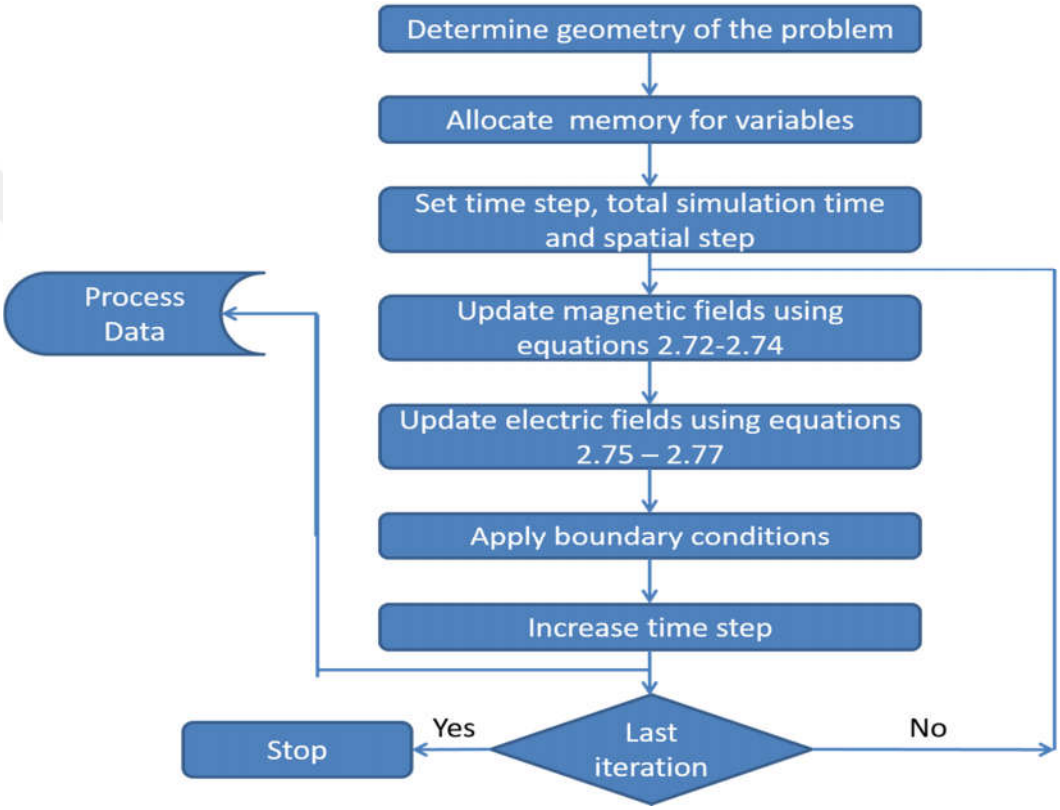

Figure 2.13 Flowchart of FDTD Algorithm

2.5.3.2. Reduction to 2D TE and TM Modes

When both the structure being modeled and the excitation does not change with respect to specific direction e.g. z direction, then the derivatives in Maxwell's curl equations (2.3) and (2.4) with respect to that direction vanish. The resulting equations can then be split into two uncoupled groups which are known as TE and TM. Assuming that there is no variation in z direction, these two groups are presented in (2.78) and (2.79).

$$\left.\begin{aligned} \frac{\partial H_x}{\partial t} &= -\frac{1}{\mu}\frac{\partial E_z}{\partial y} \\ \frac{\partial H_y}{\partial t} &= \frac{1}{\mu}\frac{\partial E_z}{\partial x} \\ \frac{\partial E_z}{\partial t} &= \frac{1}{\epsilon}\left[\frac{\partial H_y}{\partial x} - \frac{\partial H_x}{\partial y}\right] \end{aligned}\right\} TM_z \tag{2.78}$$

$$\left.\begin{aligned} \frac{\partial E_x}{\partial t} &= \frac{1}{\epsilon}\frac{\partial H_z}{\partial y} \\ \frac{\partial E_y}{\partial t} &= -\frac{1}{\epsilon}\frac{\partial H_z}{\partial x} \\ \frac{\partial H_z}{\partial t} &= \frac{1}{\mu}\left[\frac{\partial E_x}{\partial y} - \frac{\partial E_y}{\partial x}\right] \end{aligned}\right\} TE_z \tag{2.79}$$

2D FDTD update equations for TM_z and TE_z modes can be obtained similar to that for 3D by replacing partial derivatives with their second-order centered difference approximations. For the sake of completeness, they are given in equations (2.80) through (2.85):

TE_z Mode

$$H_z\Big|_{i+\frac{1}{2},j+\frac{1}{2}}^{n+\frac{1}{2}} = H_z\Big|_{i+\frac{1}{2},j+\frac{1}{2}}^{n-\frac{1}{2}} + \frac{\Delta t}{\mu_{i+\frac{1}{2},j+\frac{1}{2}}}\left[\frac{E_x\big|_{i+\frac{1}{2},j+1}^{n} - E_x\big|_{i+\frac{1}{2},j}^{n}}{\Delta y} - \frac{E_y\big|_{i+1,j+\frac{1}{2}}^{n} - E_y\big|_{i,j+\frac{1}{2}}^{n}}{\Delta x}\right] \tag{2.80}$$

$$E_x\Big|_{i+\frac{1}{2},j}^{n+1} = E_x\Big|_{i+\frac{1}{2},j}^{n} + \frac{\Delta t}{\epsilon_{i+\frac{1}{2},j}}\left[\frac{H_z\Big|_{i+\frac{1}{2},j+\frac{1}{2}}^{n+\frac{1}{2}} - H_z\Big|_{i+\frac{1}{2},j-\frac{1}{2}}^{n+\frac{1}{2}}}{\Delta y}\right] \tag{2.81}$$

$$E_y\Big|_{i,j+\frac{1}{2}}^{n+1} = E_y\Big|_{i,j+\frac{1}{2}}^{n} - \frac{\Delta t}{\epsilon_{i,j+\frac{1}{2}}}\left[\frac{H_z\Big|_{i+\frac{1}{2},j+\frac{1}{2}}^{n+\frac{1}{2}} - H_z\Big|_{i-\frac{1}{2},j+\frac{1}{2}}^{n+\frac{1}{2}}}{\Delta x}\right] \tag{2.82}$$

TM_z Mode

$$H_x\Big|_{i,j+\frac{1}{2}}^{n+\frac{1}{2}} = H_x\Big|_{i,j+\frac{1}{2}}^{n-\frac{1}{2}} - \frac{\Delta t}{\mu_{i,j+\frac{1}{2}}}\left[\frac{E_z\big|_{i,j+1}^{n} - E_z^n\big|_{i,j}}{\Delta y}\right] \tag{2.83}$$

$$H_y\Big|_{i+\frac{1}{2},j}^{n+\frac{1}{2}} = H_y\Big|_{i+\frac{1}{2},j}^{n-\frac{1}{2}} + \frac{\Delta t}{\mu_{i+\frac{1}{2},j}}\left[\frac{E_z\big|_{i+1,j}^{n} - E_{z\,i,j}^{n}}{\Delta x}\right] \tag{2.84}$$

$$E_z\big|_{i,j}^{n+1} = E_z\big|_{i,j}^{n} + \frac{\Delta t}{\epsilon_{i,j}}\left[\frac{H_y\Big|_{i+\frac{1}{2},j}^{n+\frac{1}{2}} - H_y\Big|_{i-\frac{1}{2},j}^{n+\frac{1}{2}}}{\Delta x} - \frac{H_x\Big|_{i,j+\frac{1}{2}}^{n+\frac{1}{2}} - H_y\Big|_{i,j-\frac{1}{2}}^{n+\frac{1}{2}}}{\Delta y}\right] \tag{2.85}$$

Working with two-dimensional models is relatively easier than three-dimensional ones. The simulation time can be drastically reduced because in general less computational resources (e.g. memory) are needed. If the structure being modeled has a uniform cross section, the solution of the problem can be handled in 2D by considering cross sectional area instead of volume. The resulting two-dimensional problem can be further decomposed into TE and TM modes and solved separately. The total solution in 2D is obtained by summing the solutions of TE and TM modes. For normal incidence, the two and three-dimensional scattered fields are related by (2.86):

$$E_{3D} \approx \left(E_{2D}\frac{le^{j\pi/4}}{\sqrt{\lambda\rho}}\right) \tag{2.86}$$

where l is the length of target and ρ is the distance from target to observation point [14].

2.5.3.3. Numerical Dispersion

Wave dispersion expresses the relationship between wavelength and frequency. For an electromagnetic wave in vacuum, the frequency is proportional with wavelength and expressed by (2.87):

$$\lambda = \frac{c}{f} \text{ or } \frac{\omega}{c} = k \tag{2.87}$$

Finite difference approximation used in FDTD algorithm can cause non-physical dispersion leading the phase velocity of numerical wave to be different from its actual value. The factors that contribute to numerical dispersion are expressed by numerical dispersion relation. This expression will be derived hereafter for 2D FDTD algorithm because of its simplicity. Extension of this expression to 3D algorithm is straightforward and will also be given at the end of this section. It is obvious that, following traveling wave equations are the solutions of TM_z mode update equations (2.83-2.85):

$$H_x\big|_{I,J}^{n} = H_{x0}e^{j\left(\omega n\Delta t - k_x I\Delta x - k_y J\Delta y\right)} \tag{2.88}$$

$$H_y\big|_{I,J}^{n} = H_{y0}e^{j\left(\omega n\Delta t - k_x I\Delta x - k_y J\Delta y\right)} \tag{2.89}$$

$$E_z\big|_{I,J}^{n} = E_{z0}e^{j\left(\omega n\Delta t - k_x I\Delta x - k_y J\Delta y\right)} \tag{2.90}$$

where k_x and k_y are the x and y components of the numerical wave vector k. Substituting (2.88) and (2.90) into (2.83) yields the following equation:

$$\begin{aligned}&\left(\begin{array}{l} H_{x0}e^{j(\omega n\Delta t)}e^{j\left(\omega\Delta t\frac{1}{2}\right)}e^{-j(k_x I\Delta x)}e^{-j\left(k_y I\Delta y\right)}e^{-j\left(k_y\frac{1}{2}\Delta y\right)} - \\ H_{x0}e^{j(\omega n\Delta t)}e^{-j\left(\omega\frac{1}{2}\Delta t\right)}e^{-j(k_x I\Delta x)}e^{-j\left(k_y J\Delta y\right)}e^{-j\left(k_y\frac{1}{2}\Delta y\right)}\end{array}\right)/\Delta t \\ &= -\frac{1}{\mu\Delta y}\left(\begin{array}{l} E_{z0}e^{j(\omega n\Delta t)}e^{-j(k_x I\Delta x)}e^{-j(k_y J\Delta y)}e^{-j(k_y\Delta y)} - \\ E_{z0}e^{j(\omega n\Delta t)}e^{-j(k_x I\Delta x)}e^{-j(k_y J\Delta y)}\end{array}\right)\end{aligned} \tag{2.91}$$

Dividing both sides of the (2.91) by the common factor $e^{j(\omega n\Delta t)}e^{-j(k_x I\Delta x)}e^{-j\left(k_y\left(J+\frac{1}{2}\right)\Delta y\right)}$ gives:

$$H_{x0}\left(\frac{e^{j\left(\omega\Delta t\frac{1}{2}\right)}-e^{-j\left(\omega\Delta t\frac{1}{2}\right)}}{\Delta t}\right) = -\frac{1}{\mu\Delta y}E_{z0}\left(e^{-j(k_y\frac{1}{2}\Delta y)}-e^{+j(k_y\frac{1}{2}\Delta y)}\right) \tag{2.92}$$

Additional simplification can be achieved by using Euler's formula in (2.92). The resulting expression is given below:

$$H_{x0} = \frac{\Delta t}{\mu \Delta y} E_{z0} \frac{\sin(\frac{k_y \Delta y}{2})}{\sin(\frac{\omega \Delta t}{2})} \tag{2.93}$$

Similar expressions are obtained for H_y, E_z by using (2.89)-(2.91) into (2.84) and (2.85). The resulting equations are given in (2.94) and (2.95):

$$H_{y0} = -\frac{\Delta t}{\mu \Delta x} E_{z0} \frac{\sin(\frac{k_x \Delta x}{2})}{\sin(\frac{\omega \Delta t}{2})} \tag{2.94}$$

$$E_{z0} \sin\left(\frac{\omega \Delta t}{2}\right) = \frac{\Delta t}{\epsilon}\left[\frac{H_{x0}}{\Delta y} \sin\left(\frac{k_y \Delta y}{2}\right) - \frac{H_{y0}}{\Delta x} \sin\left(\frac{\mathrm{k}_x \Delta x}{2}\right)\right] \tag{2.95}$$

Finally, substituting (2.93) and (2.94) into (2.95) and making some algebraic manipulations leads to equation (2.96) which is known the general numerical dispersion relation for TM_z mode:

$$\left(\frac{1}{v_p \Delta t} \sin\left(\frac{\omega \Delta t}{2}\right)\right)^2 = \left(\frac{1}{\Delta x} \sin\left(\frac{\mathrm{k}_x \Delta x}{2}\right)\right)^2 + \left(\frac{1}{\Delta y} \sin\left(\frac{\mathrm{k}_y \Delta y}{2}\right)\right)^2 \tag{2.96}$$

where $v_p = \sqrt{\mu \epsilon}$ is the speed of light in the material which is characterized by ϵ and μ. This equation can be further simplified by assuming $\Delta x = \Delta y = \Delta$ and substituting $k_x = k\cos(\phi)$ and $k_y = k\sin(\phi)$ into (2.96) as shown below:

$$\left(\frac{\Delta}{v_p \Delta \mathrm{t}}\right)^2 \sin^2\left(\frac{\omega \Delta t}{2}\right) = \sin^2\left(\frac{\Delta \mathrm{k} cos(\phi)}{2}\right) + \sin^2\left(\frac{\Delta \mathrm{k} sin(\phi)}{2}\right) \tag{2.97}$$

Leaving ω alone in the left side of (2.97) and dividing both sides by k yields to below equation which is similar to (2.87):

$$\frac{\omega}{k} = \overline{v_p} = \frac{2}{k\Delta \mathrm{t}} \sin^{-1}\left(\frac{v_p \Delta t}{\Delta} \sqrt{\sin^2\left(\frac{k\cos(\phi)\Delta}{2}\right) + \sin^2\left(\frac{k\sin(\phi)\Delta}{2}\right)}\right) \tag{2.98}$$

where $\overline{v_p}$ is the phase velocity of the wave in FDTD grid. It is obvious that both Δ and

Δt affects numerical dispersion and should be carefully selected. The dependence of $\overline{v_p}$ on propagation angle ϕ is called grid anisotropy and it is demonstrated in Figs 2.14 and 2.15 for $\Delta t = \dfrac{\Delta}{2v_p}$ and $\Delta t = \dfrac{\Delta}{\sqrt{2}v_p}$ respectively. It is obvious that grid anisotropy is reduced by increasing the resolution i.e. decreasing cell size. It will be equal to ideal case for $\phi = 45°$ and $\Delta t = \dfrac{\Delta}{\sqrt{2}v_p}$ in 2D. Apart from that, numerical dispersion error cannot be totally eliminated because we are restricted to work with finite grid cells. For this reason, numerical dispersion error is inherited to FDTD algorithm, but this error is very small even for $\lambda/5$ resolution. Extension of numerical dispersion relation to 3D is simply performed by adding third dimension to (2.98) as given below:

$$\frac{\omega}{k} = \overline{v_p} = \frac{2}{k\Delta t}\sin^{-1}\left(\frac{v_p \Delta t}{\Delta}\sqrt{\sin^2\left(\frac{\tilde{k}_x \Delta}{2}\right) + \sin^2\left(\frac{\tilde{k}_y \Delta}{2}\right) + \sin^2\left(\frac{\tilde{k}_z \Delta}{2}\right)}\right) \qquad (2.99)$$

In this case, grid anisotropy will be equal to ideal case for $\tilde{k}_x = \tilde{k}_y = \tilde{k}_z = \tilde{k}\sqrt{3}$ i.e. propagation along a diagonal of cubic cell with time step $\Delta t = \dfrac{\Delta}{\sqrt{3}v_p}$.

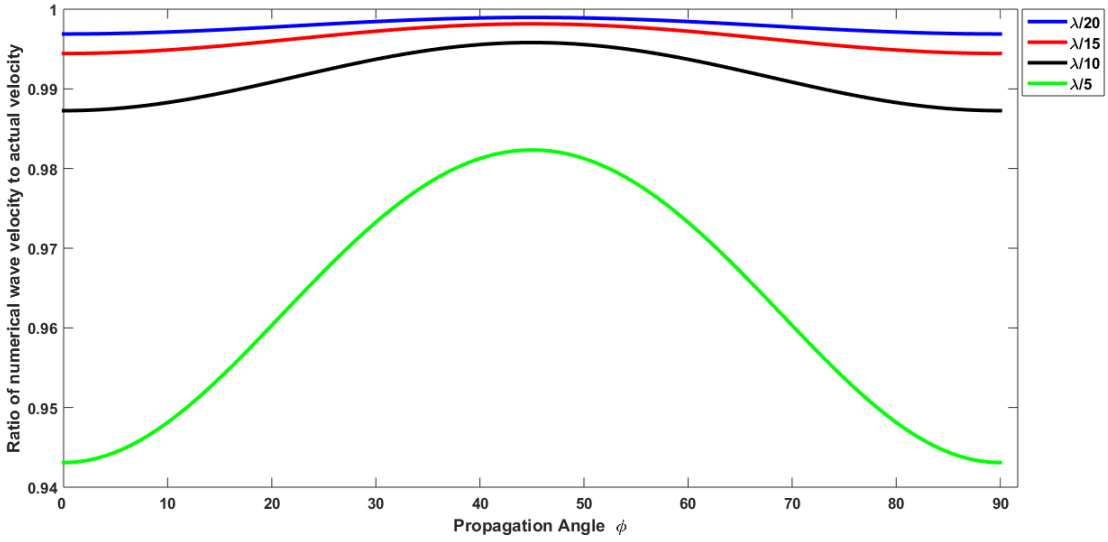

Figure 2.14 Grid anisotropy in 2D FDTD simulation for $\Delta t = \Delta / 2v_p$

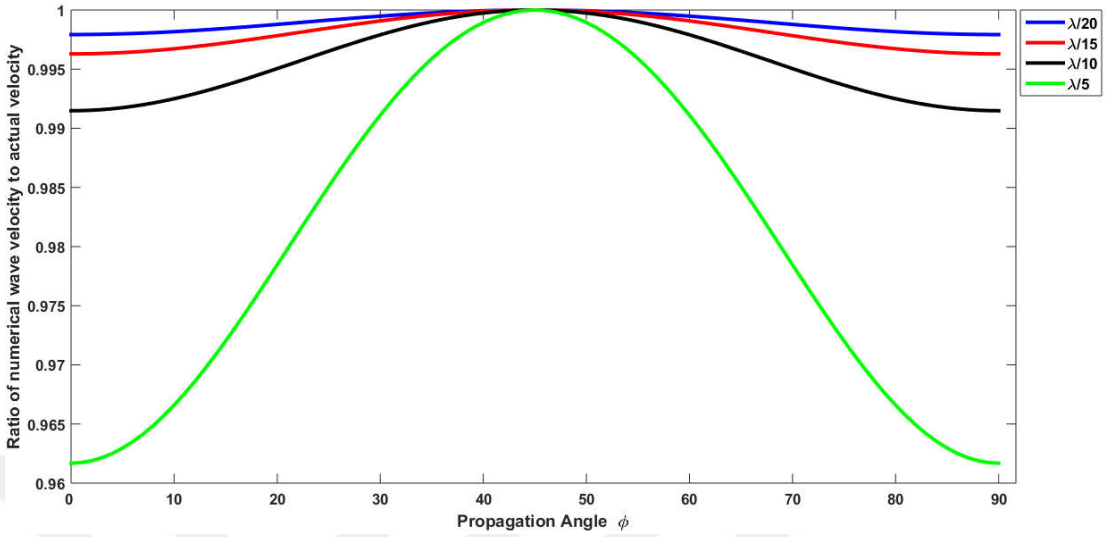

Figure 2.15 Grid anisotropy in 2D FDTD simulation for $\Delta t = \Delta / \sqrt{2} v_p$

2.5.3.4.Stability

Selection of time step Δt affects not only grid anisotropy but also stability of FDTD algorithm. To demonstrate this, numerical angular frequency is allowed to have imaginary part in the solution of wave equation as shown below for equation (2.90):

$$E_z\Big|_{I,J}^{n} = E_{z0} e^{j\left(\left(\omega_{real} + j\omega_{imag}\right) n\Delta t - \hat{k}_x I\Delta x - \hat{k}_y J\Delta y\right)} = E_{z0} e^{\left(-\Delta t n \omega_{imag}\right)} e^{j\left(\omega_{real} n\Delta t - \hat{k}_x I\Delta x - \hat{k}_y J\Delta y\right)} \quad (2.100)$$

If the term ω_{imag} in equation (2.100) is positive, then the amplitude of the wave decreases with time. On the other hand, if ω_{imag} is negative, the amplitude of the wave exponentially increases with time and eventually becomes infinite. Numerical angular frequency expression for 2D was given before in equation (2.98). By inspecting this equation, it can be seen that if the term inside the arcsine function has value between 0 and 1, numerical angular frequency consists only real part and stable propagation is guaranteed. The upper bound of the expression in square root is given by:

$$\sqrt{\frac{1}{\Delta x^2}\sin^2\left(\frac{\hat{k}\cos(\phi)\Delta \mathrm{x}}{2}\right) + \frac{1}{\Delta y^2}\sin^2\left(\frac{\hat{k}\sin(\phi)\Delta \mathrm{y}}{2}\right)} \le \sqrt{\frac{1}{\Delta x^2} + \frac{1}{\Delta y^2}} \quad (2.101)$$

Therefore, we need to consider the following equation:

$$0 \le v_p \Delta t \sqrt{\frac{1}{\Delta x^2} + \frac{1}{\Delta y^2}} \le 1 \tag{2.102}$$

To ensure stability, time step Δt should be selected as:

$$\Delta t \le \frac{1}{v_p \sqrt{\frac{1}{\Delta x^2} + \frac{1}{\Delta y^2}}} \tag{2.103}$$

If the same cell size is used in both x and y dimensions i.e. $\Delta x = \Delta y = \Delta$, equation (2.103) can be written as:

$$\Delta t \le \frac{\Delta}{v_p \sqrt{2}} \tag{2.104}$$

The meaning of (2.104) is that electromagnetic wave can travel at most one cell diagonally in one time step in 2D. Similar expression is obtained for 3D case by adding third dimension to (2.103):

$$\Delta t \le \frac{1}{v_p \sqrt{\frac{1}{\Delta x^2} + \frac{1}{\Delta y^2} + \frac{1}{\Delta z^2}}} \tag{2.105}$$

In this case, equation (2.105) states that electromagnetic wave can travel at most one cubic cell diagonally in one time step.

2.5.3.5. Perfectly Matched Layer Boundary Condition

Scattering and radiation problems require the simulation space to be extended to infinity. Due to the finite nature of computers we cannot use infinite number of cells. Even if we are interested in near fields, we need to enlarge total simulation space to prevent reflections from the boundaries. However, increasing total simulation space increases the computational burden excessively. So far, several methods proposed to overcome this difficulty [29] - [31]. These methods split into two groups, one is called absorbing boundary conditions (ABC), and the other is called radiation boundary conditions (RBC).

RBCs require the storage of field components more than one time step back depending on the order of accuracy. Hence, they can cause out of memory errors for large problems.

Furthermore, since they are a function of incident angle, they can give spurious reflections for grazing angles.

On the other hand, ABCs don't require the storage of field components more than one time step back, and give more accurate results compared to RBCs. Among ABCs, the perfectly matched layer (PML) boundaries are very popular and easy to implement. PML is a finite-thickness special lossy medium which is placed at the terminals of the computational space to create perfectly matching condition for all angles and frequencies. There are several types of PMLs found in literature such as uniaxial PML (UPML), convolutional PML (CPML) and split-field PML (SPML). Detailed comparison of PML types can be found in [31]. In this dissertation, we preferred to use UPML because of its simplicity. Therefore this type of PML will be explained hereafter. We will start by reviewing electromagnetic field behaviour at the boundary of two dissimilar media to explain the theory behind all kind of PMLs.

Considering a TM_z polarized field shown in Fig. 2.16, incident electric field is written in phasor form as:

$$\mathbf{E_i} = \mathbf{z}e^{-(j\boldsymbol{k_i}\cdot\boldsymbol{r})} = \mathbf{z}e^{-j\left(k_i\cos(\theta_i)x + k_i\sin(\theta_i)y\right)} = \mathbf{z}e^{-j\left(k_{ix}x + k_{iy}y\right)} \tag{2.106}$$

The corresponding incident magnetic field can be obtained simply by using phasor form of Faraday's law as shown below:

$$\begin{aligned}\mathbf{H_i} = -\frac{1}{j\omega u_1}\nabla\times\mathbf{E_i} &= -\frac{1}{j\omega\mu_1}\begin{vmatrix}\mathbf{x} & \mathbf{y} & \mathbf{z}\\ \partial/\partial x & \partial/\partial y & \partial/\partial z\\ 0 & 0 & e^{-j\left(k_{ix}x+k_{iy}y\right)}\end{vmatrix}\\ &= -\frac{1}{j\omega\mu_1}\left(-jk_{iy}\mathbf{x} + jk_{ix}\mathbf{y}\right)e^{-j\left(k_{ix}x+k_{iy}y\right)}\\ &= \left[\mathbf{x}\frac{k_{iy}}{\omega\mu_1} - \mathbf{y}\frac{k_{ix}}{\omega\mu_1}\right]e^{-j\left(k_{ix}x+k_{iy}y\right)}\end{aligned} \tag{2.107}$$

Assuming that reflected field also exists in region 1, we can express its electric field component as:

$$\mathbf{E_r} = -\mathbf{z}\Gamma e^{-j\left(-k_{ix}x+k_{iy}y\right)} \tag{2.108}$$

where $\Gamma = \frac{|\mathbf{E_r}(0,y)|}{|\mathbf{E_i}(0,y)|}$ is the reflection coefficient. Similarly, reflected magnetic field is obtained by using (2.108) in phasor form of Faraday law. Total field in region 1 equals to the sum of incident and reflected fields and it is given by (2.109) and (2.110) for electric and magnetic field respectively:

$$\mathbf{E_1} = \mathbf{z}\left(e^{-jk_{ix}x} + \Gamma e^{+jk_{ix}x}\right)e^{-jk_{iy}y} \tag{2.109}$$

$$\mathbf{H_1} = \mathbf{x}\frac{k_{iy}}{\omega\mu_1}\left(e^{-j(k_{1x}x)} + \Gamma e^{(k_{1x}x)}\right)e^{-j(k_{1y}y)} + \mathbf{y}\frac{k_{ix}}{\omega\mu_1}\left(-e^{-j(k_{1x}x)} + \Gamma e^{(k_{1x}x)}\right)e^{-j(k_{1y}y)} \tag{2.110}$$

Now we can consider the electromagnetic field in region 2 which is a lossy medium characterized with the parameters; electrical conductivity (σ_2) and magnetic conductivity (σ_m). The transmitted electric field in region 2 is expressed by:

$$\mathbf{E_t} = \mathbf{E_2} = \mathbf{z}\mathrm{T}e^{-j(k_{tx}x + k_{ty}y)} \tag{2.111}$$

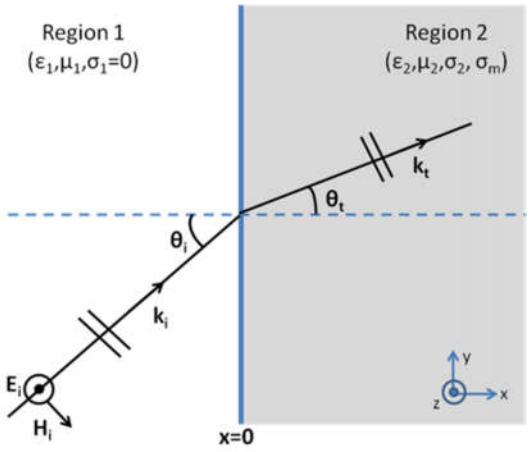

Figure 2.16 Plane wave incident on a lossy medium

where $\mathrm{T} = \frac{|\mathbf{E_T}(0,y)|}{|\mathbf{E_i}(0,y)|}$ is the transmission coefficient. To calculate magnetic field, we need to utilize Faraday's law for lossy medium as shown below:

$$\mathbf{H_t} = -\frac{1}{j\omega\mu_2\left(1+\frac{\sigma_m}{j\omega\mu_2}\right)}\nabla\times\mathbf{E_t} = \begin{bmatrix} \mathbf{x}\dfrac{k_{ty}}{\omega\mu_2\left(1+\dfrac{\sigma_m}{j\omega\mu_2}\right)} \\ -\mathbf{y}\dfrac{k_{tx}}{\omega\mu_2\left(1+\dfrac{\sigma_m}{j\omega\mu_2}\right)} \end{bmatrix} \mathrm{T}e^{-j\left(k_{tx}x+k_{ty}y\right)} \tag{2.112}$$

where $k_{tx} = k_t\cos(\theta)$, $k_{ty} = k_t\sin(\theta)$, $k_t^{\,2} = k_{tx}^{\,2} + k_{ty}^{\,2} = \omega^2\mu_{eff}\epsilon_{eff}$. The relationship between the fields in region 1 and region 2 can be described by boundary conditions given by (2.17)-(2.20). Enforcing the continuity of tangential electric and magnetic fields on the boundary (x=0) yields the following equations:

$$\mathbf{z}\left(1+\Gamma\right)e^{-jk_{iy}y} = \mathbf{z}\mathrm{T}e^{-j\left(k_{ty}y\right)} \tag{2.113}$$

$$\mathbf{y}\frac{k_{ix}}{\omega\mu_1}\left(-1+\Gamma\right)e^{-j\left(k_{1y}y\right)} = -\mathbf{y}\frac{k_{tx}}{\omega u_2\left(1+\dfrac{\sigma_m}{j\omega\mu_2}\right)}\mathrm{T}e^{-j\left(k_{ty}y\right)} \tag{2.114}$$

Reflection and transmission coefficients are easily obtained from (2.113) and (2.114) and given as:

$$\Gamma = \frac{\eta_2\cos\theta_i - \eta_1\cos\theta_t}{\eta_2 cos\theta_i + \eta_1 cos\theta_t} = \frac{\dfrac{k_{tx}}{\omega\epsilon_2\left(1+\dfrac{\sigma_2}{j\omega\epsilon_2}\right)} - \dfrac{k_{ix}}{\omega\epsilon_1}}{\dfrac{k_{tx}}{\omega\epsilon_2\left(1+\dfrac{\sigma_2}{j\omega\epsilon_2}\right)} + \dfrac{k_{ix}}{\omega\epsilon_1}} \tag{2.115}$$

$$\mathrm{T} = 1+\Gamma = \frac{\dfrac{2k_{tx}}{\omega\epsilon_2\left(1+\dfrac{\sigma_2}{j\omega\epsilon_2}\right)}}{\dfrac{k_{tx}}{\omega\epsilon_2\left(1+\dfrac{\sigma_2}{j\omega\epsilon_2}\right)} + \dfrac{k_{ix}}{\omega\epsilon_1}} \tag{2.116}$$

As can be observed from equation (2.115), reflection coefficient will be zero only if the numerator equals to zero. Assuming that the incidence angle equal to zero i.e. $\theta_i = 0$, the expression for reflection coefficient reduces to

$$\Gamma = \frac{\eta_2 - \eta_1}{n_2 + \eta_1} \tag{2.117}$$

where η_1, η_2 are the intrinsic impedances of medium 1 and 2 respectively and expressed by:

$$\eta_2 = \sqrt{\frac{\mu_{eff}}{\epsilon_{eff}}} = \sqrt{\frac{\left(\mu_2\left(1 + \frac{\sigma_m}{j\omega\mu_2}\right)\right)}{\left(\epsilon_2\left(1 + \frac{\sigma_2}{j\omega\epsilon_2}\right)\right)}} \tag{2.118}$$

$$\eta_1 = \sqrt{\frac{\mu_1}{\epsilon_1}} \tag{2.119}$$

In this case, perfectly matched transmission ($\Gamma = 0$) is obtained by choosing constitutive parameters of medium 1 and 2 as $\mu_1 = \mu_2$, $\epsilon_1 = \epsilon_2$ and $\sigma_m = \frac{\sigma\mu_1}{\epsilon_1}$. Unfortunately, the numerator of the equation (2.115) cannot be zero for any oblique angle and there will always be reflected field in region 1.

Uniaxial Perfectly Matched Layer (UPML)

Among different versions of PMLs, UPML is arguably simplest to understand and has been broadly used in the FDTD simulations. In UPML, artificial anisotropic uniaxial absorbing material, which is composed of both electric and magnetic permittivity sensors, is placed in computational domain as shown in Fig 2.17. The main advantage of the UPML over other types of PMLs is that FDTD algorithm does not require any modifications and can be used in both computational and PML region.

To analyze UPML, we can assume that a TE_z polarized wave propagating through the region 2 ($x > 0$) that is formed by an anisotropic uniaxial material whose electrical permittivity and magnetic permeability are expressed by rank-2 tensors as:

$$\overline{\overline{\varepsilon_2}} = \epsilon_2 \begin{bmatrix} a & 0 & 0 \\ 0 & b & 0 \\ 0 & 0 & b \end{bmatrix} \qquad \overline{\overline{\mu_2}} = \mu_2 \begin{bmatrix} c & 0 & 0 \\ 0 & d & 0 \\ 0 & 0 & d \end{bmatrix} \tag{2.120}$$

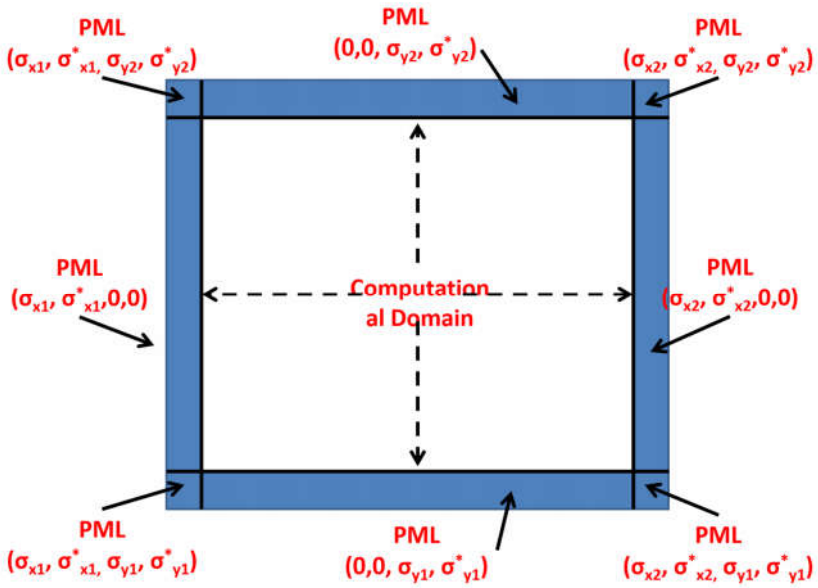

Figure 2.17 Placement of PML in FDTD Computational Domain

As we did previously for TM mode, we can write total electric and magnetic fields in the region 1 and region 2 as:

$$\mathbf{H}_1 = \mathbf{z}\mathbf{H}_0\left(1+\Gamma e^{j(2k_{1x}x)}\right)e^{-j\left(k_{1x}x+k_{1y}y\right)} \tag{2.121}$$

$$\mathbf{E}_1 = \mathbf{H}_0\left[-\mathbf{x}\frac{k_{1y}}{\omega\epsilon_1}\left(1+\Gamma e^{j(2k_{1x}x)}\right)+\mathbf{y}\frac{k_{1x}}{\omega\epsilon_1}\left(1-\Gamma e^{j(2k_{1x}x}\right)\right]e^{-j\left(k_{1x}x+k_{1y}y\right)} \tag{2.122}$$

$$\mathbf{H}_2 = \mathbf{z}\mathbf{H}_0 \mathrm{T} e^{-j\left(k_{2x}x+k_{2y}y\right)} \tag{2.123}$$

$$\mathbf{E}_2 = \mathbf{H}_0\left[-\mathbf{x}\frac{k_{2y}}{\omega\epsilon_2 a}+\mathbf{y}\frac{k_{2x}}{\omega\epsilon_2 b}\right]\mathrm{T}e^{-j\left(k_{2x}x+k_{2y}y\right)} \tag{2.124}$$

Enforcing the continuity of tangential magnetic and electric fields at the interface (x=0) yields:

$$\begin{gathered}\mathbf{H}_1(0,\mathrm{y}) = \boldsymbol{H}_2(0,\mathrm{y}) \\ \mathbf{z}\mathbf{H}_0\left(1+\Gamma\right)e^{-j\left(k_{1y}y\right)} = \mathbf{z}\mathbf{H}_0\mathrm{T}e^{-j\left(k_{2y}y\right)} \rightarrow 1+\Gamma=\mathrm{T}\text{ and } k_{1y}=k_{2y}\end{gathered} \tag{2.125}$$

$$\mathbf{E_1}(0,\mathrm{y}) = \mathbf{E_2}(0,\mathrm{y})$$
$$\mathbf{H_0}\left[\mathbf{y}\frac{k_{1x}}{\omega\epsilon_1}(1-\Gamma)\right]e^{-j(k_{1y}y)} = \mathbf{H_0}\left[\mathbf{y}\frac{k_{2x}}{\omega\epsilon_2 b}\right]\mathrm{T}e^{-j(k_{2y}y)} \tag{2.126}$$
$$\rightarrow \frac{k_{1x}}{\omega\epsilon_1}(1-\Gamma) = \frac{k_{2x}}{\omega\epsilon_2 b}\mathrm{T}$$

The expression for reflection coefficent can be derived from (2.125) and (2.126) as:

$$\Gamma = \frac{k_{1x}\omega\epsilon_2 b - k_{2x}\omega\epsilon_1}{k_{1x}\omega\epsilon_2 b + k_{2x}\omega\epsilon_1} = \frac{k_{1x}\epsilon_2 - k_{2x}\epsilon_1 b^{-1}}{k_{1x}\epsilon_2 + k_{2x}\epsilon_1 b^{-1}} \tag{2.127}$$

The fields in region 2 should satisfy the Maxwell's equations in a general anisotropic medium which can be expressed in phasor form as given below:

$$\mathbf{k_2}\times\mathbf{E} = \omega\overline{\overline{\mu_2}}\mathbf{H} \tag{2.128}$$

$$\boldsymbol{k}_2 x\mathbf{H} = -\omega\overline{\overline{\epsilon_2}}\boldsymbol{E} \tag{2.129}$$

where $\mathbf{k_2} = \mathbf{x}k_{2x} + \mathbf{y}k_{2y}$ is the wave vector in region 2. Combining equations (2.128) and (2.129) leads to second-order differential equation so-called wave equation:

$$\mathbf{k_2} x\left(\left(\overline{\overline{\epsilon_2}}\right)^{-1}\mathbf{k_2}\right)x\,\mathbf{H} + \omega^2\overline{\overline{\mu_2}}\mathbf{H} = 0 \tag{2.130}$$

which can also be written in matrix form as:

$$\begin{bmatrix} \omega^2\mu_2\epsilon_2 c - k_{2y}^2 b^{-1} & k_{2x}k_{2y}b^{-1} & 0 \\ k_{2x}k_{2y}b^{-1} & k_2^2 d - k_{2x}^2 b^{-1} & 0 \\ 0 & 0 & \omega^2\mu_2\epsilon_2 d - k_{2x}^2 b^{-1} - k_{2y}^2 a^{-1} \end{bmatrix}\begin{bmatrix} \mathbf{H_x} \\ \mathbf{H_y} \\ \mathbf{H_z} \end{bmatrix} = 0 \tag{2.131}$$

Assuming the TE_z polarization (H_x,H_y=0), (2.131) reduces to:

$$\omega^2\mu_2\epsilon_2 d - k_{2x}^2 b^{-1} - k_{2y}^2 a^{-1} = 0 \tag{2.132}$$

Solution of the equation (2.132) is actually dispersion relation for anisotropic uniaxial medium and gives the relationship between wave-vectors k_{2x}, k_{2y} and angular frequency.

Since $k_{1y} = k_{2y}$ for all incident angles as given by (2.125), x-component of wave vector can be expressed as:

$$k_{2x} = \sqrt{\omega^2 \epsilon_2 \mu_2 bd - k_{1y}^2 a^{-1} b} \tag{2.133}$$

To achive reflectionless transmission at the boundary, the nominator of equation (2.127) should be equal to zero i.e. $k_{2x} = bk_{1x}$. This can be achived by choosing $\epsilon_1 = \epsilon_2$, $\mu_1 = \mu_2$, $d = b$ and $a^{-1} = b$ as given below:

$$k_{2x} = \sqrt{\omega^2 \epsilon_1 \mu_1 b^2 - k_{1y}^2 b^2} = b\sqrt{k_1^2 - k_{1y}^2} = bk_{1x} \tag{2.134}$$

The field components in region 2 are then expressed by

$$\mathbf{H_2} = \mathbf{z}\mathbf{H_0} e^{-j\left(bk_{1x}x + k_{1y}y\right)} \tag{2.135}$$

$$\mathbf{E_2} = \mathbf{H_0}\left[-\mathbf{x}\frac{k_{1y}}{\omega\epsilon_2 a} + \mathbf{y}\frac{k_{1x}}{\omega\epsilon_2}\right] e^{-j\left(bk_{1x}x + k_{1y}y\right)} \tag{2.136}$$

As can be observed from (2.135) or (2.136), selection of $b = 1 - \frac{\sigma_x}{j\omega\epsilon_1}$ yields exponentially attenuating wave for all incident wave angles and k_{1x}. The same analysis can be repeated for TM_z mode. In this case we need to replace b with d and a with c and set $c^{-1} = d$ to achieve reflectionless propagation. In summary, if the permittivity ($\overline{\overline{\epsilon}}$) and permeability tensors ($\overline{\overline{\mu}}$) are of the form:

$$\overline{\overline{\epsilon_2}} = \epsilon_1 \overline{\overline{s}}; \quad \overline{\overline{\mu_2}} = \mu_2 \overline{\overline{s}}; \quad \overline{\overline{s}} = \begin{bmatrix} s_x^{-1} & 0 & 0 \\ 0 & s_x & 0 \\ 0 & 0 & s_x \end{bmatrix} \tag{2.137}$$

where $s_x = K_x + \frac{\sigma_x}{j\omega\epsilon_1}$, then the lossy layer perfectly matches to computational domain and provides exponentially attenuating propagation along x direction. Here the parameter K_x is introduced for allowing non-unity real part. Similar expression is obtained for other dimensions e.g by changing K_x, σ_x with K_y, σ_y in (2.137) for y dimension. The whole

computational area can be covered by placing individual layers to the terminals of each dimension of computational space. A more general expression of tensor $\overline{\overline{s}}$ is given by (2.138):

$$\begin{aligned}\overline{\overline{\boldsymbol{s}}} &= \begin{bmatrix} s_x^{-1} & 0 & 0 \\ 0 & s_x & 0 \\ 0 & 0 & s_x \end{bmatrix}\begin{bmatrix} s_y^{-1} & 0 & 0 \\ 0 & s_y & 0 \\ 0 & 0 & s_y \end{bmatrix}\begin{bmatrix} s_z^{-1} & 0 & 0 \\ 0 & s_z & 0 \\ 0 & 0 & s_z \end{bmatrix} \\ &= \begin{bmatrix} s_x^{-1}s_y s_z & 0 & 0 \\ 0 & s_x s_y^{-1} s_z & 0 \\ 0 & 0 & s_x s_y s_z^{-1} \end{bmatrix}\end{aligned} \tag{2.138}$$

The values of s_x, s_y and s_z are only non-zero at corresponding boundaries e.g. $\sigma_x = \sigma_z = 0$ at $y = 0$ and $y = y_{tot}$.

UPML Algorithm

To derive an algorithm for UPML, we can start by using the tensor introduced previously in the matrix form of Ampere's law (in phasor form) as follows:

$$\begin{bmatrix} \frac{\partial H_z}{\partial y} - \frac{\partial H_y}{\partial z} \\ \frac{\partial H_x}{\partial z} - \frac{\partial H_z}{\partial x} \\ \frac{\partial H_y}{\partial x} - \frac{\partial H_x}{\partial y} \end{bmatrix} = j\omega\epsilon \begin{bmatrix} s_x^{-1}s_y s_z & 0 & 0 \\ 0 & s_x s_y^{-1} s_z & 0 \\ 0 & 0 & s_x s_y s_z^{-1} \end{bmatrix}\begin{bmatrix} E_x \\ E_y \\ E_z \end{bmatrix} \tag{2.139}$$

Expansion of (2.139) yields three equations for electric field components and the first among them is given by:

$$\frac{\partial H_z}{\partial y} - \frac{\partial H_y}{\partial z} = j\omega\epsilon \left[\frac{\left(K_y + \frac{\sigma_y}{j\omega\epsilon}\right)\left(K_z + \frac{\sigma_z}{j\omega\epsilon}\right)}{\left(K_x + \frac{\sigma_x}{j\omega\epsilon}\right)} \right] E_x \tag{2.140}$$

Converting of (2.140) from phasor domain to time domain introduces integral operation because of the term $j\omega\epsilon + \sigma_x$ in the denominator. However, integral operation is

computationally expensive especially for large problems. To overcome this difficulty, an interim field **D** that is expressed by (2.141) can be used in (2.139) instead of the electric field components as shown by (2.142):

$$\begin{aligned} D_x &= \epsilon \frac{s_z}{s_x} E_x \\ D_y &= \epsilon \frac{s_x}{s_y} E_y \\ D_z &= \epsilon \frac{s_y}{s_z} E_z \end{aligned} \tag{2.141}$$

$$\begin{bmatrix} \frac{\partial H_z}{\partial y} - \frac{\partial H_y}{\partial z} \\ \frac{\partial H_x}{\partial z} - \frac{\partial H_z}{\partial x} \\ \frac{\partial H_y}{\partial x} - \frac{\partial H_x}{\partial y} \end{bmatrix} = j\omega \begin{bmatrix} s_y & 0 & 0 \\ 0 & s_z & 0 \\ 0 & 0 & s_x \end{bmatrix} = \begin{bmatrix} D_x \\ D_y \\ D_z \end{bmatrix} \tag{2.142}$$

Equation (2.142) is then transformed from phasor domain to time domain by using the property $\frac{\partial}{\partial t} \leftrightarrow j\omega$ easily. The resulting time domain equation can be discretized using centered difference approximation similar to FDTD algorithm. The components of interim fields **D** are assumed to be at the same location as electric fields components. For the sake of completeness, their discrete forms are presented in (2.143)-(2.145):

$$\begin{aligned} D_x \Big|_{i+\frac{1}{2},j,k}^{n+1} &= \left(\frac{2\epsilon K_y - \sigma_y \Delta t}{2\epsilon K_y + \sigma_y \Delta t} \right) D_x \Big|_{i+\frac{1}{2},j,k}^{n} \\ &+ \frac{2\epsilon \Delta t}{2\epsilon K_y + \sigma_y \Delta t} \left[\frac{H_z \Big|_{i+\frac{1}{2},j+\frac{1}{2},k}^{n+\frac{1}{2}} - H_z \Big|_{i+\frac{1}{2},j-\frac{1}{2},k}^{n+\frac{1}{2}}}{\Delta y} - \frac{H_y \Big|_{i+\frac{1}{2},j,k+\frac{1}{2}}^{n+\frac{1}{2}} - H_y \Big|_{i+\frac{1}{2},j,k-\frac{1}{2}}^{n+\frac{1}{2}}}{\Delta z} \right] \end{aligned} \tag{2.143}$$

$$D_y\Big|_{i,j+\frac{1}{2},k}^{n+1} = \left(\frac{2\epsilon K_z - \sigma_z \Delta t}{2\epsilon K_z + \sigma_z \Delta t}\right) D_y\Big|_{i,j+\frac{1}{2},k}^{n} + \frac{2\epsilon \Delta t}{2\epsilon K_z + \sigma_z \Delta t}\left[\frac{H_x\Big|_{i,j+\frac{1}{2},k+\frac{1}{2}}^{n+\frac{1}{2}} - H_x\Big|_{i,j+\frac{1}{2},k-\frac{1}{2}}^{n+\frac{1}{2}}}{\Delta z} - \frac{H_z\Big|_{i+\frac{1}{2},j+\frac{1}{2},k}^{n+\frac{1}{2}} - H_z\Big|_{i-\frac{1}{2},j+\frac{1}{2},k}^{n+\frac{1}{2}}}{\Delta x}\right] \tag{2.144}$$

$$D_z\Big|_{i,j,k+\frac{1}{2}}^{n+1} = \left(\frac{2\epsilon K_x - \sigma_x \Delta t}{2\epsilon K_x + \sigma_x \Delta t}\right) D_z\Big|_{i,j,k+\frac{1}{2}}^{n} + \frac{2\epsilon \Delta t}{2\epsilon K_x + \sigma_x \Delta t}\left[\frac{H_y\Big|_{i+\frac{1}{2},j,k+\frac{1}{2}}^{n+\frac{1}{2}} - H_y\Big|_{i-\frac{1}{2},j,k+\frac{1}{2}}^{n+\frac{1}{2}}}{\Delta x} - \frac{H_x\Big|_{i,j+\frac{1}{2},k+\frac{1}{2}}^{n+\frac{1}{2}} - H_x\Big|_{i,j-\frac{1}{2},k+\frac{1}{2}}^{n+\frac{1}{2}}}{\Delta y}\right] \tag{2.145}$$

Once interim fields are calculated, we need to convert them back to electric field components. This can be accomplished easily via (2.41) e.g. the following conversion formula is obtained for x-component of electric field:

$$D_x = \epsilon \frac{s_z}{s_x} E_x \rightarrow j\omega K_x D_x + \frac{\sigma_x}{\epsilon} D_x = j\omega \epsilon K_x E_x + \sigma_z E_x \tag{2.146}$$

Converting (2.146) from phasor domain to time domain leads to:

$$K_x \frac{\partial D_x}{\partial t} + \frac{\sigma_x}{\epsilon} D_x = \epsilon K_z \frac{\partial E_x}{\partial t} + \sigma_z E_x. \tag{2.147}$$

The above equation can also be discretized by using central difference approximation as shown below:

$$E_x\Big|_{i+\frac{1}{2},j,k}^{n+1} = \left(\frac{2\epsilon K_z - \sigma_z \Delta t}{2\epsilon K_z + \sigma_z \Delta t}\right) E_x\Big|_{i+\frac{1}{2},j,k}^{n} + \frac{1}{\epsilon}\left(\frac{2\epsilon K_x + \sigma_x \Delta t}{2\epsilon K_z + \sigma_z \Delta t}\right) D_x\Big|_{i+\frac{1}{2},j,k}^{n+1} - \frac{1}{\epsilon}\left(\frac{2\epsilon K_x - \sigma_x \Delta t}{2\epsilon K_z + \sigma_z \Delta t}\right) D_x\Big|_{i+\frac{1}{2},j,k}^{n} \tag{2.148}$$

The same analysis can be repeated for the remaining components of electric fields, and discrete form of them are presented in (2.149) and (2.150):

$$\begin{aligned} E_y\Big|_{i,j+\frac{1}{2},k}^{n+1} &= \left(\frac{2\epsilon K_x-\sigma_x\Delta t}{2\epsilon K_x+\sigma_x\Delta t}\right)E_y\Big|_{i,j+\frac{1}{2},k}^{n} \\ &+\frac{1}{\epsilon}\left(\frac{2\epsilon K_y+\sigma_y\Delta t}{2\epsilon K_x+\sigma_x\Delta t}\right)D_y\Big|_{i,j+\frac{1}{2},k}^{n+1}-\frac{1}{\epsilon}\left(\frac{2\epsilon K_y-\sigma_y\Delta t}{2\epsilon K_x+\sigma_x\Delta t}\right)D_y\Big|_{i,j+\frac{1}{2},k}^{n} \end{aligned} \tag{2.149}$$

$$\begin{aligned} E_z\Big|_{i,j,k+\frac{1}{2}}^{n+1} &= \left(\frac{2\epsilon K_y-\sigma_y\Delta t}{2\epsilon K_y+\sigma_y\Delta t}\right)E_z\Big|_{i,j,k+\frac{1}{2}}^{n} \\ &+\frac{1}{\epsilon}\left(\frac{2\epsilon K_z+\sigma_z\Delta t}{2\epsilon K_y+\sigma_y\Delta t}\right)D_z\Big|_{i,j,k+\frac{1}{2}}^{n+1}-\frac{1}{\epsilon}\left(\frac{2\epsilon K_z-\sigma_z\Delta t}{2\epsilon K_y+\sigma_y\Delta t}\right)D_z\Big|_{i,j,k+\frac{1}{2}}^{n} \end{aligned} \tag{2.150}$$

Thus far, we are concerned with the electric field components. The magnetic fields can also be calculated in a similar manner by writing the curl operator of equation (2.128) in matrix form as follows:

$$\begin{bmatrix} \frac{\partial E_z}{\partial y}-\frac{\partial E_y}{\partial z} \\ \frac{\partial E_x}{\partial z}-\frac{\partial E_z}{\partial x} \\ \frac{\partial E_y}{\partial x}-\frac{\partial E_x}{\partial y} \end{bmatrix} = -j\omega\mu\begin{bmatrix} s_x^{-1}s_y s_z & 0 & 0 \\ 0 & s_x s_y^{-1} s_z & 0 \\ 0 & 0 & s_x s_y s_z^{-1} \end{bmatrix} = \begin{bmatrix} H_x \\ H_y \\ H_z \end{bmatrix} \tag{2.151}$$

In this case an auxiliary field $\mathbf{B}$ that is expressed by (2.152) is introduced to avoid integral operation. Using this auxiliary field $\mathbf{B}$ in (2.151) leads to (2.153) that can be converted to time domain easily by using the transformation $\frac{\partial}{\partial t}\leftrightarrow j\omega$:

$$\begin{aligned} B_x &= \mu\frac{s_z}{s_x}H_x \\ B_y &= \epsilon\frac{s_x}{s_y}H_y \\ B_z &= \epsilon\frac{s_y}{s_z}H_z \end{aligned} \tag{2.152}$$

$$\begin{bmatrix} \dfrac{\partial E_z}{\partial y} - \dfrac{\partial E_y}{\partial z} \\ \dfrac{\partial E_x}{\partial z} - \dfrac{\partial E_z}{\partial x} \\ \dfrac{\partial E_y}{\partial x} - \dfrac{\partial E_x}{\partial y} \end{bmatrix} = -j\omega \begin{bmatrix} s_y & 0 & 0 \\ 0 & s_z & 0 \\ 0 & 0 & s_x \end{bmatrix} = \begin{bmatrix} B_x \\ B_y \\ B_z \end{bmatrix} \tag{2.153}$$

The resulting time domain equation can be discretized by replacing partial derivatives with their second-order central differences. By doing so, the following update equations are obtained for interim field components:

$$\begin{aligned} B_x\Big|_{i,j+\frac{1}{2},k+\frac{1}{2}}^{n+\frac{1}{2}} &= \left(\frac{2\epsilon K_y - \sigma_y \Delta t}{2\epsilon K_y + \sigma_y \Delta t}\right) B_x\Big|_{i,j+\frac{1}{2},k+\frac{1}{2}}^{n-\frac{1}{2}} \\ &+ \left(\frac{2\epsilon \Delta t}{2\epsilon K_y + \sigma_y \Delta t}\right) \left[\begin{array}{l} \dfrac{E_y\big|_{i,j+\frac{1}{2},k+1}^{n} - E_y\big|_{i,j+\frac{1}{2},k}^{n}}{\Delta z} \\ -\dfrac{E_z\big|_{i,j+1,k+\frac{1}{2}}^{n} - E_z\big|_{i,j,k+\frac{1}{2}}^{n}}{\Delta y} \end{array}\right] \end{aligned} \tag{2.154}$$

$$\begin{aligned} B_y\Big|_{i+\frac{1}{2},j,k+\frac{1}{2}}^{n+\frac{1}{2}} &= \left(\frac{2\epsilon K_z - \sigma_z \Delta t}{2\epsilon K_z + \sigma_z \Delta t}\right) B_y\Big|_{i+\frac{1}{2},j,k+\frac{1}{2}}^{n-\frac{1}{2}} \\ &+ \left(\frac{2\epsilon \Delta t}{2\epsilon K_z + \sigma_z \Delta t}\right) \left[\begin{array}{l} \dfrac{E_z\big|_{i+1,j,k+\frac{1}{2}}^{n} - E_z\big|_{i,j,k+\frac{1}{2}}^{n}}{\Delta x} \\ -\dfrac{E_x\big|_{i+\frac{1}{2},j,k+1}^{n} - E_x\big|_{i+\frac{1}{2},j,k}^{n}}{\Delta z} \end{array}\right] \end{aligned} \tag{2.155}$$

$$\begin{aligned} B_z\Big|_{i+\frac{1}{2},j+\frac{1}{2},k}^{n+\frac{1}{2}} &= \left(\frac{2\epsilon K_x - \sigma_x \Delta t}{2\epsilon K_x + \sigma_x \Delta t}\right) B_z\Big|_{i+\frac{1}{2},j+\frac{1}{2},k}^{n-\frac{1}{2}} \\ &+ \left(\frac{2\epsilon \Delta t}{2\epsilon K_x + \sigma_x \Delta t}\right) \left[\begin{array}{l} \dfrac{E_x\big|_{i+\frac{1}{2},j+1,k}^{n} - E_x\big|_{i+\frac{1}{2},j,k}^{n}}{\Delta y} \\ -\dfrac{E_y\big|_{i+1,j+\frac{1}{2},k}^{n} - E_y\big|_{i,j+\frac{1}{2},k}^{n}}{\Delta x} \end{array}\right] \end{aligned} \tag{2.156}$$

The relationship between the interim field **B** and magnetic field **H** is similar to that of interim field **D** and **E** and can be given e.g. for the x component as:

$$B_x = \mu \frac{s_z}{s_x} H_x \; or \; s_x B_x = \mu s_z H_x \rightarrow j\omega K_x B_x + \frac{\sigma_x}{\epsilon} B_x = j\omega\mu K_z H_x + \frac{\sigma_z}{\epsilon} \mu H_x \quad (2.157)$$

Equation (2.157) is in phasor domain and needs to be expressed in time domain to be used within FDTD algorithm. The resulting time domain equations can then be discretized by using central difference approximation. Equations (2.158)-(2.160) gives discretized forms of these equations.

$$\begin{aligned} H_x \Big|_{i,j+\frac{1}{2},k+\frac{1}{2}}^{n+\frac{1}{2}} &= \left(\frac{2\epsilon K_z - \sigma_z \Delta t}{2\epsilon K_z + \sigma_z \Delta t} \right) H_x \Big|_{i,j+\frac{1}{2},k+\frac{1}{2}}^{n-\frac{1}{2}} \\ &+ \frac{1}{\mu} \left(\frac{2\epsilon K_x + \sigma_x \Delta t}{2\epsilon K_z + \sigma_z \Delta t} \right) B_x \Big|_{i,j+\frac{1}{2},k+\frac{1}{2}}^{n+\frac{1}{2}} - \frac{1}{\mu} \left(\frac{2\epsilon K_x - \sigma_x \Delta t}{2\epsilon K_z + \sigma_z \Delta t} \right) B_x \Big|_{i,j+\frac{1}{2},k+\frac{1}{2}}^{n-\frac{1}{2}} \end{aligned} \quad (2.158)$$

$$\begin{aligned} H_y \Big|_{i+\frac{1}{2},j,k+\frac{1}{2}}^{n+\frac{1}{2}} &= \left(\frac{2\epsilon K_x - \sigma_x \Delta t}{2\epsilon K_x + \sigma_x \Delta t} \right) H_y \Big|_{i+\frac{1}{2}j,k+\frac{1}{2}}^{n-\frac{1}{2}} \\ &+ \frac{1}{\mu} \left(\frac{2\epsilon K_y + \sigma_y \Delta t}{2\epsilon K_x + \sigma_x \Delta t} \right) B_y \Big|_{i+\frac{1}{2},j,k+\frac{1}{2}}^{n+\frac{1}{2}} - \frac{1}{\mu} \left(\frac{2\epsilon K_y - \sigma_y \Delta t}{2\epsilon K_x + \sigma_x \Delta t} \right) B_y \Big|_{i+\frac{1}{2},j,k+\frac{1}{2}}^{n-\frac{1}{2}} \end{aligned} \quad (2.159)$$

$$\begin{aligned} H_z \Big|_{i+\frac{1}{2},j+\frac{1}{2},k}^{n+\frac{1}{2}} &= \left(\frac{2\epsilon K_y - \sigma_y \Delta t}{2\epsilon K_y + \sigma_y \Delta t} \right) H_z \Big|_{i+\frac{1}{2}j+\frac{1}{2},k}^{n-\frac{1}{2}} \\ &+ \frac{1}{\mu} \left(\frac{2\epsilon K_z + \sigma_z \Delta t}{2\epsilon K_y + \sigma_y \Delta t} \right) B_z \Big|_{i+\frac{1}{2},j+\frac{1}{2},k}^{n+\frac{1}{2}} - \frac{1}{\mu} \left(\frac{2\epsilon K_z - \sigma_z \Delta t}{2\epsilon K_y + \sigma_y \Delta t} \right) B_y \Big|_{i+\frac{1}{2},j+\frac{1}{2},k}^{n-\frac{1}{2}} \end{aligned} \quad (2.160)$$

In summary, implementation of UPML algorithm requires two steps for updating individual electric and magnetic fields. In the first step interim fields are calculated by using (2.143)-(2.145) or (2.154)-(2.156). Then in the second step, electric and magnetic fields are calculated from the interim fields by using (2.148)-(2.150) or (2.158)-(2.160). Fig. 2.18 shows three snapshots that is taken at different time steps to demonstrate the PML boundary condition in Gaussian source-excited 2D TM_z mode. An ideal PML is reflectionless, if the parameters are selected properly as described before. However, due to the discretization of PML equations, significant spurious reflections may occur. To overcome this problem, multilayer PML is used. The term multilayer means that the conductivity profile of lossy layer changes with spatial increment. There are several methods in literature to create such a multilayer PML [32], [33] but arguably the most

effective one is obtained by polynomial grading in which conductivity profile is expressed as:

$$\sigma(x) = \sigma_{max}\left(\frac{d-x}{d}\right)^{m}. \tag{2.161}$$

Here d is the thickness of the PML and σ_{max} is the maximum value of the conductivity which is expressed as:

$$\sigma_{max} = \frac{m+1}{200\pi\sqrt{\epsilon_r}\Delta}. \tag{2.162}$$

The parameter m is generally taken as 3 or 4.

2.5.3.6.Modeling PEC Objects

Modeling objects accurately plays important role in FDTD simulations. Standard FDTD algorithm explained so far uses staircase approximation to model objects. We can examine staircase approximation for TM_z mode and TE_z mode separately in 2D simulations as follows: when modeling a PEC in TM_z mode, if E_z node falls within the PEC, it is set to zero and if H_z node falls within the PEC in TE_z mode, all surrounding electric fields are set to zero. Anyhow, magnetic fields are updated in the usual way for both 3D and 2D. Although this approach is very simple to use, it can lead to significant errors for slanted or curved objects as shown in Fig. 2.19 for TE_z mode. Here, critical cells located at the boundary of PEC object are marked with "x". As it is seen, staircase approximation of missile radome is very poor and sharp corners resulted from the staircase approximation lead to diffracted fields that don't exist in reality. The amount of staircase error can be reduced by increasing resolution (i.e. decreasing cell size) but this increases computational burden significantly. To overcome this difficulty, several methods are proposed in the past decade [34] - [36]. One solution to this problem is to use non-uniform meshing [34]. In this method, smaller cells are used around the object boundaries. Although this approach is simple to implement, total number of cells and computational burden will still be unacceptable for complex objects. The second and more robust solution is called as contour-path or Dey-Mittra modeling. This approach is based on deforming Yee cells in specific regions to conform boundaries of PEC object [36].

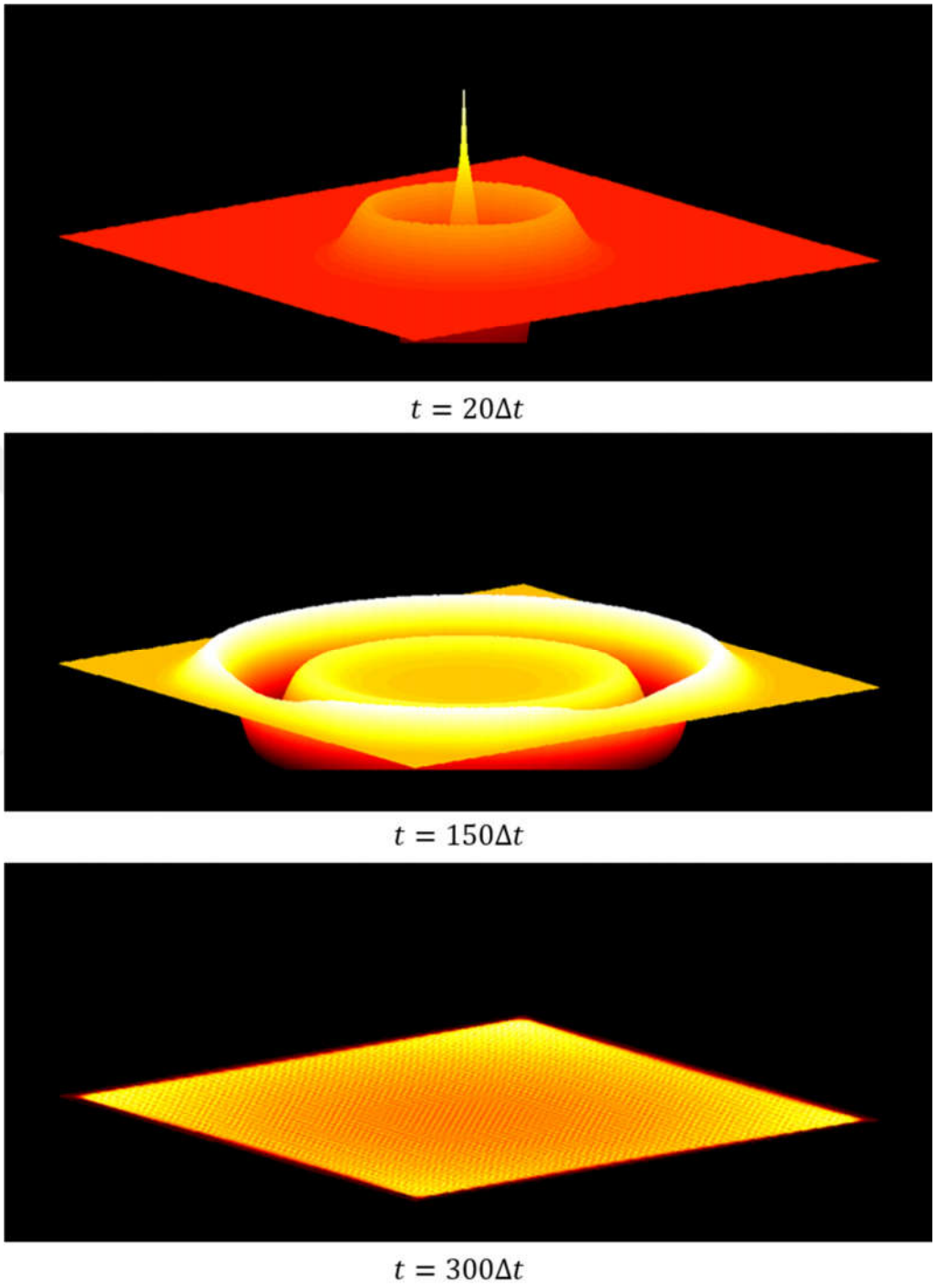

Figure 2.18 Snapshots of 2D FDTD Simulation for TM_z mode

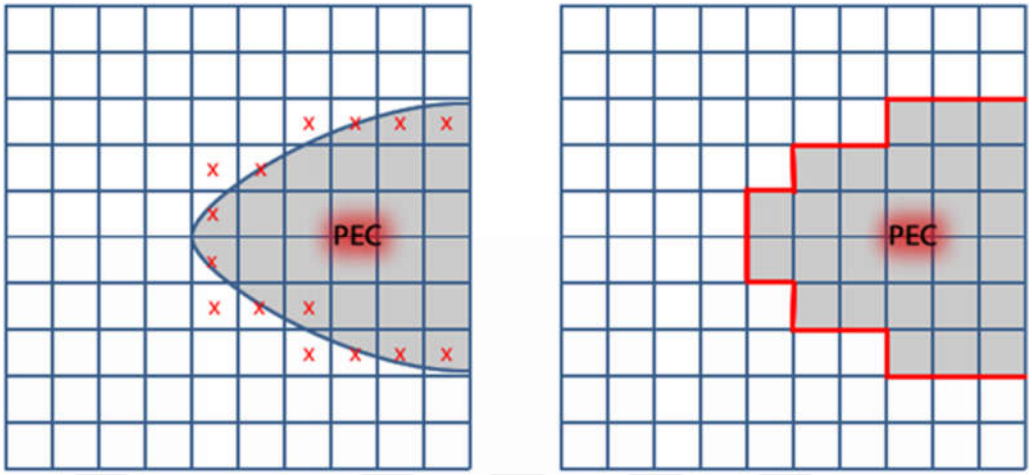

Figure 2.19 Staircase modeling of missile radome [30]

To understand conformal modeling, it is intructive to investigate three different scenarios presented in Fig. 2.20. In all scenarios TE_z polarization is assumed and the PEC is located at the right of the cell cut. In Fig.2.20 (a), slanted object cross slightly into top right cell. If the ratio $s/\Delta x\Delta y$ is less than R_1 which is specific parameter based on numerical stability, this penetration can be neglected and all four surrounding electric fields are set to zero in top right cell. On the other hand, a significant portion of the top left cell does not reside within PEC material. Hence this cell is neither treated as PEC nor non-PEC. The update equations for this cell is obtained by applying Faraday's law and integrating along the contour of area A_1 as given by (2.163):

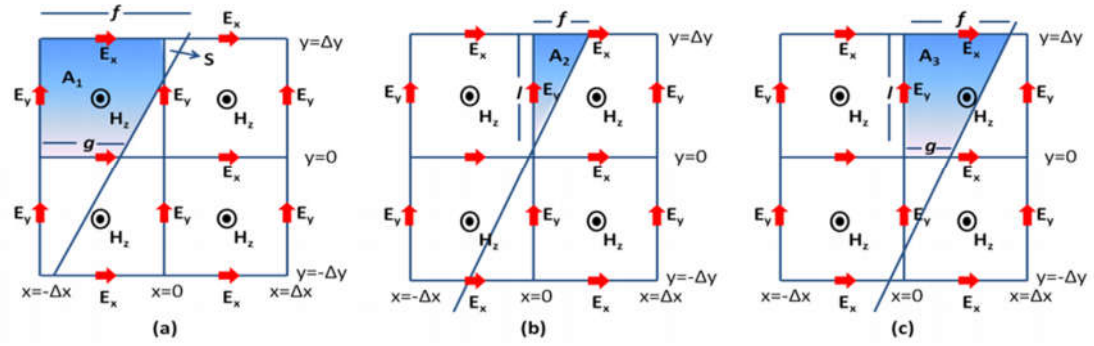

Figure 2.20 Three different scenarios for conformal modeling [37]

$$H_z^{n+\frac{1}{2}}\left(-\frac{\Delta x}{2},\frac{\Delta y}{2}\right)=H_z^{n-\frac{1}{2}}\left(-\frac{\Delta x}{2},\frac{\Delta y}{2}\right)+\frac{\Delta t}{\mu_0 A_1}\begin{pmatrix}E_y^n\left(-\Delta x,\frac{\Delta y}{2}\right)\Delta y+E_x^n\left(-\frac{\Delta x}{2},\Delta y\right)f\\-E_x^n\left(-\frac{\Delta x}{2},0\right)g\end{pmatrix} \quad (2.163)$$

In Fig. 2.20 (b) the ratio of $A_2/(\Delta x\Delta y)$ is larger than R_1. Even the H_z component resides within PEC, the area A_2 should be excluded from PEC region. This can be accomplished by applying Faraday's law to the top right cell and integrating over the contour of area A_2. Noting that two electric field components reside within PEC set to zero, we have:

$$H_z^{n+\frac{1}{2}}\left(\frac{\Delta x}{2},\frac{\Delta y}{2}\right)=H_z^{n-\frac{1}{2}}\left(\frac{\Delta x}{2},\frac{\Delta y}{2}\right)+\frac{\Delta t}{\mu_0 A_2}\left(E_y^n\left(0,\frac{\Delta y}{2}\right)l+E_x^n\left(\frac{\Delta x}{2},\Delta y\right)f\right) \quad (2.164)$$

Finally for the part (c) of Fig. 2.20, applying Faraday's law and integrating along over the contour of area A_3 gives:

$$H_z^{n+\frac{1}{2}}\left(\frac{\Delta x}{2},\frac{\Delta y}{2}\right)=H_z^{n-\frac{1}{2}}\left(\frac{\Delta x}{2},\frac{\Delta y}{2}\right)+\frac{\Delta t}{\mu_0 A_3}\begin{pmatrix}E_y^n\left(0,\frac{\Delta y}{2}\right)\Delta y+E_x^n\left(\frac{\Delta x}{2}+\Delta y\right)f\\-E_x^n\left(\frac{\Delta x}{2},0\right)g\end{pmatrix} \quad (2.165)$$

For all scenarios, electric fields are updated as in conventional Yee's algorithm. The parameter R_1 specifies the smallest area which is included for specification of integration contour. Typically, the choice $R_1=0.025$ require %30 reduction of time step below the normal limit to ensure stability. The stability analysis of Day-Mittra conformal techniques can be found in [38]. The advantage of using contour-path modeling over staircase approximation is demonstrated in Fig. 2.21. Here, diffracted fields from a wedge of 80° apex angle that is illuminated by a line source located at 60° from the tip, is considered. It is obvious that, the fields in the vicinity of wedge diverge (shown in dashed circle) in staircase approximation. On the other hand, Day-Mittra conformal technique gives very precise result in everywhere.

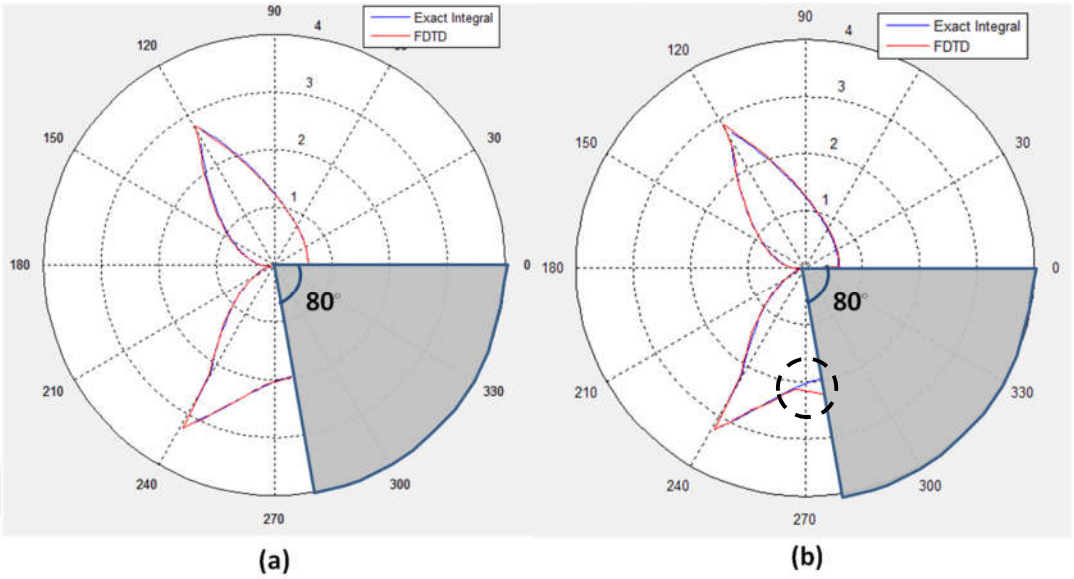

Figure 2.21 Comparison of Dey-Mittra (a) and staircase (b) modeling in wedge diffraction problem

3. DOUBLE TIP DIFFRACTION MODELING

Diffraction is a wave phenomenon and defined as the bending of a wave around the edges of an aperture or obstacle. It can be best explained by Huygen's principle with the aid of Fig.3.1. The principle states that every point on a wavefront, which is a set of equiphase points on propagating wave, may be considered as a source of secondary spherical wavelets which spread out in the forward direction at the speed of light [39]. The new wavefront is the tangential surface to all of these secondary wavelets. The direction of the propagating wave is determined by a vector which is perpendicular to the surface of wavefront at each point e.g. wavefront of point source is sphere and the wave radiates spherically.

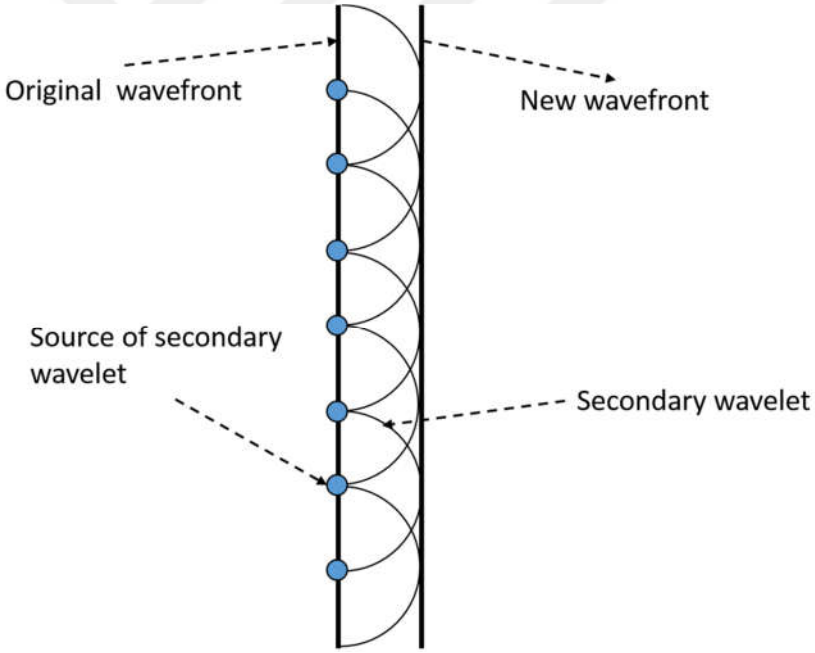

Figure 3.1 Huygen's Principle

To show relationship between Huygen's principle and diffraction, let's assume that incidence plane wave hits a perfectly reflecting obstacle with an aperture as shown at Fig.3.2. Let's further assume that aperture size is much smaller than wavelength of the incidence wave. When the wave hits non-apertured portion, it will be reflected back. When it comes to aperture, the points on the wavefront creates wavelets and these wavelets form a new wavefront which spreads beyond the obstacle. This phenomenon is known as diffraction and the resulting wavefront is called as diffracted wave. As the wavelength

becomes larger than object the diffraction tends to be stronger. Hence, for constant size objects such as hills and mountains, it can be stated that lower frequency waves diffract more than higher frequency waves, in other words, if there exists e.g a mountain between transmitter and receiver, using lower frequency signals (e.g. AM band) provide better signal reception than higher frequency signals (e.g. FM band).

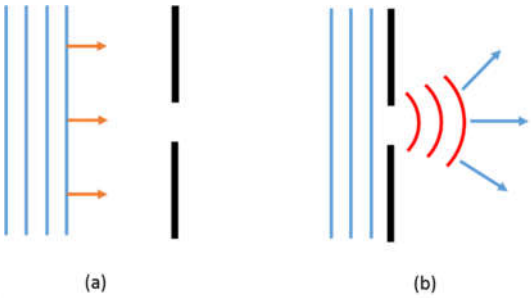

Figure 3.2 Plane wave diffraction by perfectly reflecting object with aperture: (a) Before the wave hits object, (b) After the wave hits the object

Diffraction is important in communication problems because it is the only source of transmitted signal in shadow regions. The other reason diffraction is important is that it represents the principal source of radar signals that return at all angles other than those producing specular reflections. Hence, designer of low observable targets should minimize diffraction effects by avoiding discontinuities at the object surface and material. Diffraction is also important in the way of electromagnetic compatibility (EMC). Unwanted radiation can diffract from the discontinuity and affect other parts of the device. Therefore, product designers should consider diffraction effects and use shielding techniques to protect critical components of the system. An interesting discussion on the diffraction can be found in [40].

Theoretical analysis of diffraction is very complicated and exact diffraction models are only available for limited number of geometries such as wedges, long-thin cylinders and spheres. High frequency asymptotic (HFA) methods, such as geometric theory of diffraction (GTD), uniform theory of diffraction (UTD), and physical theory of diffraction (PTD) has long been used to analyze diffracted fields when the wavelength is small compared to object size [5], [41] - [45]. A useful MATLAB-based virtual tool has been introduced for the use of HFA modeling in the classical wedge problem [46]. Backscattering from a wedge with different boundary conditions is also modeled

analytically [47]. Diffraction modeling has also been investigated numerically [15], [48] - [51]. Diffracted waves and diffraction coefficients are extracted with the FDTD method using time-gating in [52]. A more general multi-step FDTD approach is also used in diffraction modeling [49], [50]. Similarly it is shown in [15], [51] that the MoM is also successful in diffraction modeling. Double diffraction has also been investigated analytically and numerically [53] - [62]. The double wedge or double tip is a canonical geometry which arises in many practical structures. The analysis via a spectral extension of the UTD has been described, which yields closed-form expressions for the field doubly diffracted in the far zone by the edges of two interacting wedges illuminated by a plane wave in [54], [55]. The UTD has been extended to include double diffraction by an arbitrary configuration of two wedges and a scalar double diffraction coefficient is defined in [56]. An HFA analysis of the scattering by a double impedance wedge via the extended spectral ray method and diffraction coefficients were derived for up to and including the triple diffraction mechanism in [60]. A time domain single diffraction solution of a wedge type obstacle is extended to double diffraction and the resulting waveform is compared with the corresponding solution in the frequency domain by applying the inverse Fourier transform of the waveform in [62].

In this dissertation, a novel time-domain based double tip diffraction modeling approach is introduced by FDTD method. In parallel, MoM-based model is also developed in our group; hence it is included to this chapter. An analytical solution using a spectral approach for the problem of scattering by two-dimensional (2D) semi-infinite or finite polygonal objects with an imperfectly reflective surface, illuminated by a plane wave can be found in [63].

3.1. Double Tip Diffraction Structure

The structure shown in Fig. 3.3 is used in double tip diffraction modeling. The polar coordinates ρ, φ, z are used. It is a non-penetrable rectangular object infinite along z and excited with a line source. The problem has a translational symmetry along z therefore can be investigated in 2D on the xy plane. The origin is chosen at midpoint of the top edge with length L therefore the top boundary extends from $(-L/2, 0)$ to $(+L/2, 0)$ on the axis. The lengths of left and right boundaries are infinite $(d_L = d_R \to \infty)$. The line source is

assumed only in the first quadrant $(0 \le \varphi_0 \le \pi/2)$ because of the structural symmetry. The dashed circle with radius ρ shows the locations of receivers. 360 receivers are located on this circle which yields $\Delta\varphi = 1°$ angular resolution. Under these assumptions, top boundary reflected fields exist for the receivers located between the lines L_1 and L_2, while side boundary (specular) reflections occur only for the receivers between the lines L_3 and L_4. Incident fields do not exist in the shadow region bounded by the left side of the structure and the line SB. The two tips are responsible for the creation of the diffracted fields which exist everywhere. Note that Fig. 3.3 shows the reflection and shadow regions for $\rho_0 \cos\varphi_0 > L/2$. Mathematically, the problem is postulated via the 2D wave equation in polar coordinates:

$$\left\{\frac{1}{\rho}\frac{\partial}{\partial\rho}\left(\rho\frac{\partial}{\partial\rho}\right)+\frac{1}{\partial^2}\frac{\partial^2}{\partial\varphi^2}+k^2\right\}u=\frac{I_0}{\rho}\delta(\rho-\rho_0)\delta(\varphi-\varphi_0) \tag{3.1}$$

where k is the wave number, I_0 is the line current amplitude, (ρ_0,φ_0) and (ρ,φ) specify the source and the observation points, respectively, $\delta(\cdot)$ is the Dirac delta function. The related non-penetrable BCs are $u=0$ (TM case) or $\partial u/\partial n = 0$ (TE case) on the structure. Radiation condition also applies.

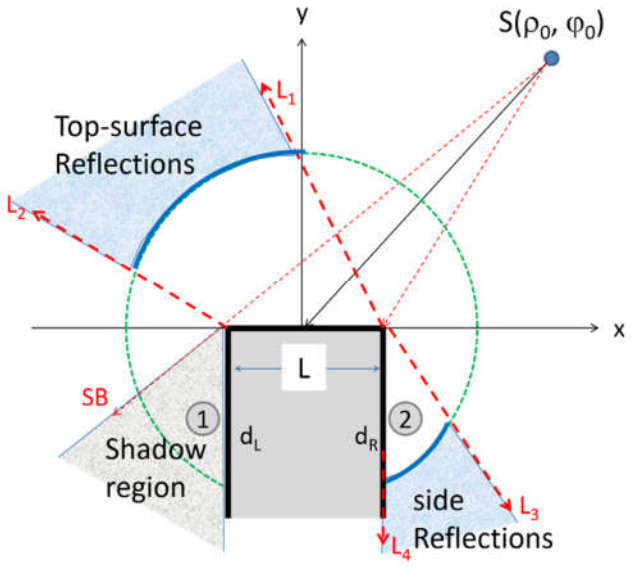

Figure 3.3 Double tip structure (Structure-1)

In the limit when the lengths of left and right boundaries goes to zero the structure yields another canonical scattering problem; the infinite strip problem. This is pictured in Fig. 3.4. The tips marked with number 1 and 2 are responsible for the creation of the diffracted fields. In this case, reflected fields only exist for the receivers located between the lines L_1 and L_2. The region between the lines SB_1 and SB_2 is the shadow region where no incident field exists. The incident, scattered, and diffracted field components all exist elsewhere.

Note also that, the structure in Fig. 3.3 also reduces to (vertical) half-plane problem when $L \to 0$ meaning that three important canonical problems can be investigated at the same time once numerical models are established for the Structure-1 in the figure. Electromagnetic line source may be the z component of either electric field intensity ($u = E_z$, TM case) or magnetic field intensity ($u = H_z$, TE case). In the case of acoustic waves, these conditions refer to acoustically soft ($\mathrm{TM} \to \mathrm{SBC}$) and hard ($\mathrm{TE} \to \mathrm{HBC}$) boundary conditions, respectively.

Note that, the word scattering represents all types of waves generated from EM (incident) wave-object interaction (e.g., reflections, refractions, diffractions, creeping waves, whispering gallery waves, etc.). The addition of scattered and incident fields yields total fields. Diffractions occur from edge and/or tip type discontinuities.

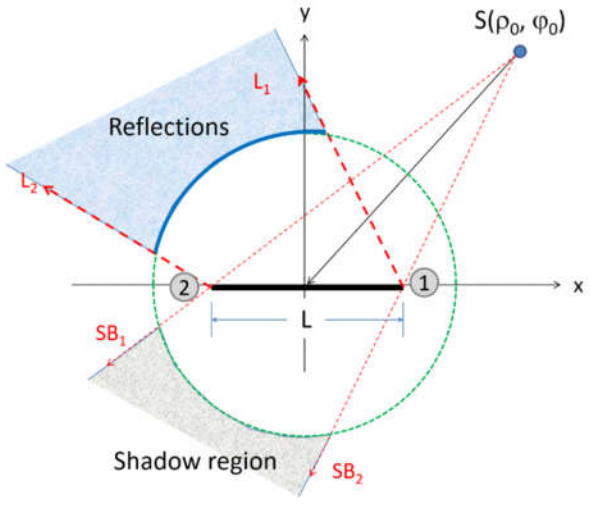

Figure 3.4 Infinite strip problem (Structure-2)

3.2. FDTD Model

The FDTD method has been used in the calculation of diffraction coefficients and there are many studies in modeling diffraction from various wedges [49], [50], [52]. The multi-step FDTD approach introduced in [49] is extended here for the calculation of double tip diffractions. The incident, reflected, and diffracted fields are separated in the time and then total and/or diffracted fields vs. angle are obtained by the application of Fast Fourier Transform (FFT). For the structure in Fig. 3.3, diffracted fields are extracted with the following 4 steps:

1) Run the FDTD simulation with the structure and record transient responses at the specified number of receivers on the observation circle. This will yield total fields.

2) Remove the structure, re-run the FDTD simulation in free space and record transient responses at the same receivers. This will yield incident fields.

3) Replace the structure with infinite-plane (in other words, extend the top edge of the structure infinitely on the horizontal axis) and re-run the FDTD simulations. Recorded fields will include only incident and reflected fields on the upper half-plane. Use them only for the receivers located between the lines L_1 and L_2.

4) Extend the right side of the structure infinitely on the vertical direction and repeat step 3. Recorded fields will include only incident and reflected fields on the right half-plane. Use them only for the receivers located between the lines L_3 and L_4.

Once time variations of the fields for the four steps are obtained incident and reflected fields are extracted in regions where they exist and only time variations of diffracted fields are left at the receivers on the observation circle. Diffracted fields at a specified frequency can then be extracted by the application of FFT on all receivers' data. Note that, only the first three steps are enough to extract diffracted field data for the infinite strip shown in Fig. 3.4. Moreover, only the first two steps are enough to obtain scattered field.

Also note that, the incident field is a pulse in time therefore broadband diffraction characteristic can be obtained via a single FDTD simulation. Once incident and diffracted pulses are recorded, discrete/fast Fourier transform (DFT/FFT) can be applied and diffraction coefficient vs. frequency and/or diffraction coefficients vs. angle variations can

be obtained. The 2D FDTD models used for TM and TE polarizations on the xy -plane contain sets of H_x, H_y, E_z and E_x, E_y, H_z components, respectively. The update equations for these polarizations are given in section 2.5.3.2.

3.3. MoM Model

A similar multi-step MoM is also used in diffraction modeling as described in [15], [51]. Here, the method is extended to double tip diffraction problem. In this model, the three boundaries of Structure-1 in Fig. 3.3 are divided into small segments (where segment lengths are much smaller than the wavelength). Although $d_L = d_R \to \infty$, they have to be finite in numerical algorithms. Side boundary lengths between $10\lambda - 100\lambda$ are enough depending on the parameters of the problem at hand. The length of top boundary is finite. The currents on each segment are assumed to be constant. In the standard MoM, the source-excited segment fields are calculated, the matrix system is built, and the segment currents are calculated numerically from the solution of the derived system of equations [51]. The segment-scattered fields at the observer are then accumulated.

Necessary MoM equations (with the time dependence) in this procedure are:

$$\begin{aligned} V_m &= -E_z^{inc}(\boldsymbol{\rho}_\mathbf{m}) = -e_0 H_0^{(1)}(k\,|\,\boldsymbol{\rho}_\mathbf{m} - \boldsymbol{\rho}_0\,|) \text{ (SBC)} \\ V_m &= -H_z^{inc}(\boldsymbol{\rho}_\mathbf{m}) = -h_0 H_0^{(1)}(k\,|\,\boldsymbol{\rho}_\mathbf{m} - \boldsymbol{\rho}_0\,|) \text{ (HBC)} \end{aligned} \tag{3.2}$$

where V_m denotes the field at matching points ($\boldsymbol{\rho}_\mathbf{m}$) on each segment and the impedance matrix is obtained by:

$$Z_{mn} \cong \begin{cases} -\dfrac{k\eta_0\Delta}{4} H_0^{(1)}(k\,|\,\boldsymbol{\rho}_\mathbf{m} - \boldsymbol{\rho}_\mathbf{n}\,|), & m \neq n \\ -\dfrac{k\eta_0\Delta}{4}\left[1 + i\dfrac{2}{\pi}\log\left(\dfrac{\gamma k\Delta}{4e}\right)\right], & m = n \end{cases} \text{ (SBC)}$$

$$Z_{mn} \cong \begin{cases} -\dfrac{ik\Delta}{4} H_0^{(1)}(k\,|\,\boldsymbol{\rho}_\mathbf{m} - \boldsymbol{\rho}_\mathbf{n}\,|)(\hat{\mathbf{n}}_\mathbf{n} \cdot \hat{\boldsymbol{\rho}}_\mathbf{nm}), & m \neq n \\ 0.5, & m = n \end{cases} \text{ (HBC)} \tag{3.3}$$

where Δ is the segment length, $\eta_0 \approx 120\pi$ is the intrinsic impedance of free space, $H_0^{(1)}$ and $H_1^{(1)}$ are the first kind Hankel functions with order zero and one, respectively,

$\gamma \approx 1.781$ is the exponential of the Euler constant, $\hat{\mathbf{n}}_\mathbf{n}$ denotes the unit normal vector of the segment at $\boldsymbol{\rho}_\mathbf{n}$,and $\hat{\boldsymbol{\rho}}_{\mathbf{nm}}$ is the unit vector in the direction from source $\boldsymbol{\rho}_\mathbf{n}$ to the receiving element $\boldsymbol{\rho}_\mathbf{m}$. While considering the effects of segment currents, the scattered fields are:

$$\begin{aligned} E_z^{sc}(\boldsymbol{\rho}) &\cong -\frac{k\eta_0\Delta}{4}\sum_{n=1}^{2N+M} I_n H_0^{(1)}(k\,|\boldsymbol{\rho}-\boldsymbol{\rho}_\mathbf{n}|) \quad \text{(SBC)} \\ H_z^{sc}(\boldsymbol{\rho}) &\cong -\frac{ik\Delta}{4}\sum_{n=1}^{2N+M} I_n H_1^{(1)}(k\,|\boldsymbol{\rho}-\boldsymbol{\rho}_\mathbf{n}|)\times(\hat{\mathbf{n}}_\mathbf{n}\cdot\hat{\boldsymbol{\rho}}_\mathbf{n}) \quad \text{(HBC)} \end{aligned} \tag{3.4}$$

The MoM procedure is implemented as follows: The fields upon segments in (3.2) are calculated by using the free space Green's function. The impedance matrix in (3.3) is formed. Then, the source-induced segment currents are obtained. Finally, scattered fields in (3.4) on the chosen observation points are calculated from the superposition of segment radiations using the Green's function.

The direct wave from the source to the receiver and scattered waves from all segments to the receiver are added and total wave at the receiver is obtained. For the structure in Fig. 3.3, MoM computed diffracted fields are extracted with the following 3 steps:

1) Run the MoM simulation with the structure and record the scattered fields at the specified number of receivers on the observation circle.

2) Replace the structure with infinite-plane (in other words, extend the top edge of the structure infinitely on the horizontal axis) and re-run the MoM simulations. Recorded scattered fields will include only reflected fields on the upper half-plane. Use them only for the receivers located between the lines L_1 and L_2.

3) Extend the right side of the structure infinitely in the vertical direction and repeat step 2. Recorded scattered fields will include only reflected fields on the right half-plane. Use them only for the receivers located between the lines L_3 and L_4. Only the first two steps are enough to extract diffracted field data for the infinite strip (Structure-2) shown in Fig. 3.4. In addition, MoM directly yields scattered fields therefore only the first step is enough for the extraction of scattered fields.

3.4. Examples and Comparisons

This section presents several comparisons. Note that, diffracted fields presented in the following examples contain single and double tip diffractions from both tips. Fig. 3.5 illustrates single and double diffracted waves from the left tip. The right tip also contributes the same single and double diffracted waves.

Note that, standard free space FDTD and MoM algorithms are used here. The FDTD space is terminated with UPML absorbing boundary as explained in section 2.5.3.5 and edges are directly extended into these layers. This is how infinite length structure is simulated. On the other hand, edges are truncated in MoM so that and are finite, but the lengths of the truncated edges are long enough to simulate. One needs to check if the first segment beyond the truncation has negligible induced current. Beyond the truncation, this (i.e., the simulation of the infinite edges) is achieved if the scattered field at the nearest receiver, caused by the segment currents is less than a specified value corresponding to the stated accuracy and/or error. Relative accuracy of 1% or less is used to generate all examples. Additionally, the examples given in this section present total, diffracted, and scattered fields around Structure-1, Structure-2, and for the vertical half-plane for a given line source at 30 MHz. Source and observer radial distances are 100 m ($\rho_0 = 10\lambda$) and 80 m ($\rho_0 = 8\lambda$), respectively. The polarizations and angle of incidences are mentioned in figure captions.

In Fig. 3.6; total, diffracted, and scattered fields around the tip of a vertical half-plane, simulated with both FDTD and MoM approaches, are given. Here, the angle of incidence is $\varphi_0 = 30°$. The top side of Structure-1 is taken as $L = \lambda/10$. As observed in the total field plot, the ripples in the angular region $-30° \le \varphi \le 210°$ correspond to the interference of incident and diffracted fields, the ripples in the angular region $270 \le \varphi \le 330°$ correspond to the interference of incident, diffracted, and reflected fields. The dominant diffraction occurs along the two critical boundaries Incident Shadow Boundary (ISB) and reflection shadow boundary (RSB). On the other hand, forward scattering and specular reflections dominate the scattered fields.

Figs. 3.7–3.9 belong to Structure-1. Total, diffracted and scattered fields, simulated with both FDTD and MoM approaches for different illumination angles and top surface lengths are shown in Figs. 3.7 and 3.8. Only total and diffracted fields are given in Fig. 3.9. Note

that, there are two tips and four critical boundaries. The diffracted fields along these boundaries and their interference for different top surface lengths are observed.

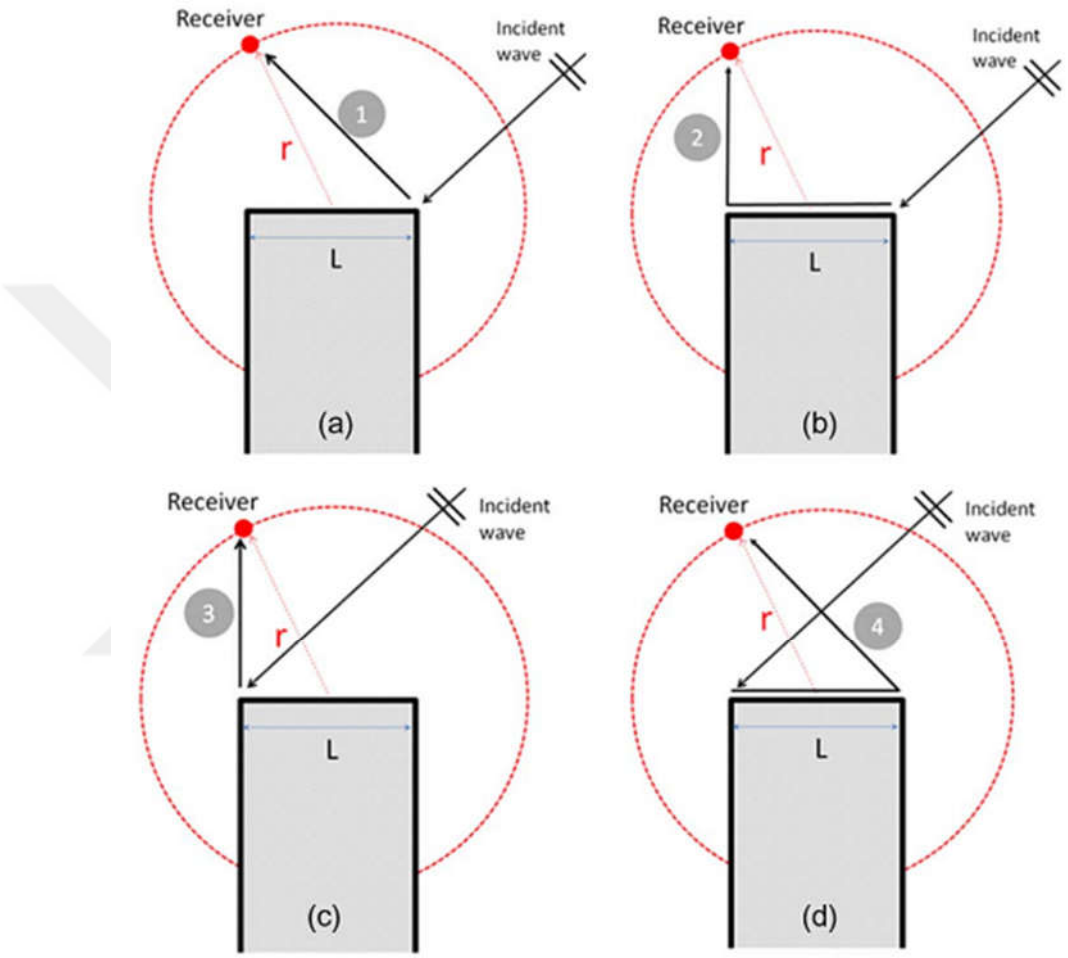

Figure 3.5 Single and double tip diffractions; (a) single diffraction from right tip, (b) double diffractions from RL-tips, (c) single diffraction from left tip, (d) double diffractions from LR-tips

Figs. 3.10–3.12 belongs to the FDTD and MoM simulation results for the Structure-2 (infinite strip). Scattered fields are also included in Figs. 3.11 and 3.12. As observed angular variations of total, scattered, and diffracted fields for different angles of illumination with different top surface lengths, the forward scattering and specular reflections dominate the scattering fields, but, as mentioned above, dominant diffractions are observed along critical boundaries. On the other hand, interference of the double diffractions may change the picture significantly depending on the angle of illumination

and top surface lengths. Note that, different discretizations are required in MoM simulations for the TM (SBC) and TE (HBC) polarizations. Infinite sides of Structure-1 are approximated by 10λ long finite sides for the TM polarization. On the other hand, up to 100λ long side-lengths may be required for the TE polarization (because ill-conditioned matrices may be obtained in this polarization). The segment lengths are chosen to be $\lambda/20$ for this polarization. The FDTD cell sizes are taken as $\lambda/20$ in both polarizations.

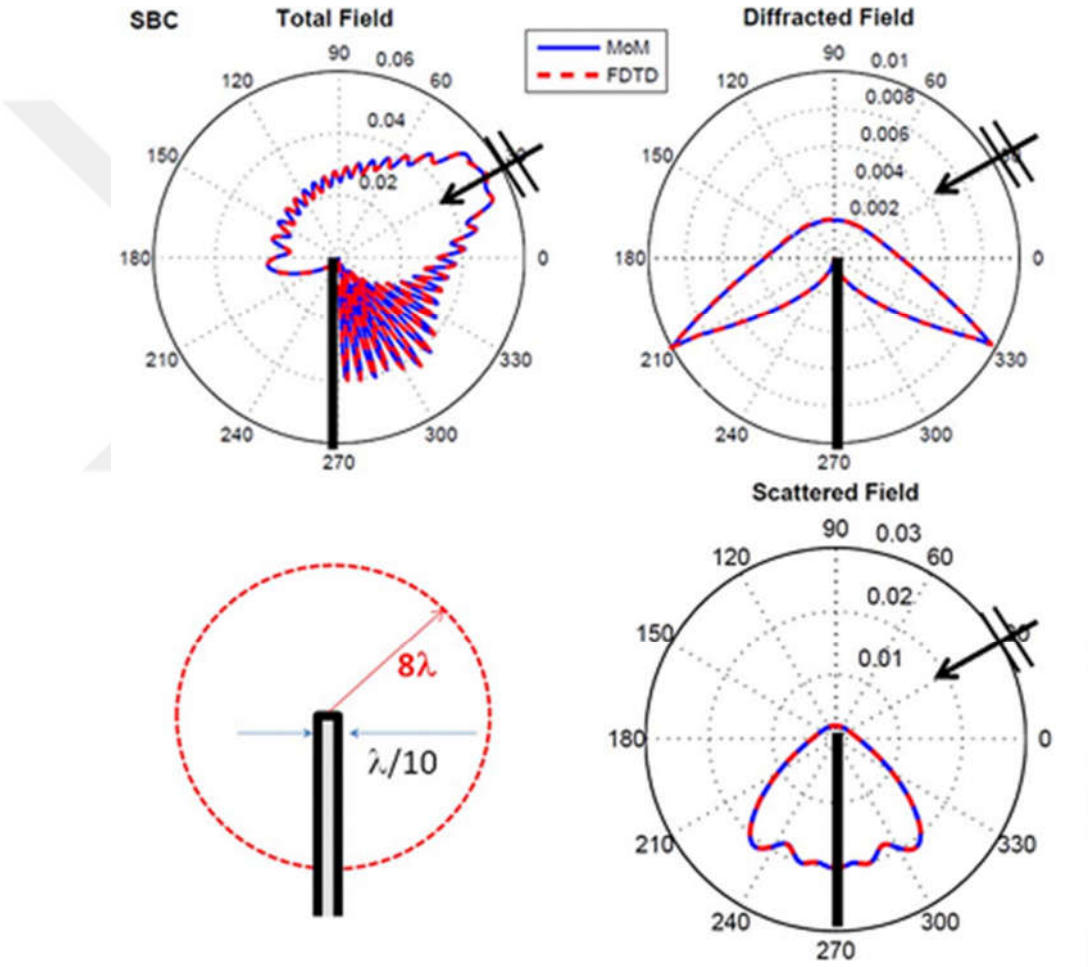

Figure 3.6 Total, diffracted, and scattered fields around Structure-1; $L=\lambda/10$, $\rho_0=10\lambda$, $\varphi_0=30°$, $\rho=8\lambda$, $f=30MHz$, TM/SBC case; Solid: MoM, Dashed: FDTD.

The source is above the horizontal plane in these examples, but it can be located arbitrarily anywhere in the angular domain. In this case, one has to pay attention to the infinite boundaries in both FDTD and MoM procedures. In other words, when a plane (or

cylindrical) wave of incidence below the horizontal plane is considered, the infinite boundaries must extend well beyond the source.

Note also that, there are highly effective commercial FDTD and MoM packages that can be used in numerical simulation of broad range of EM problems. Unfortunately, they cannot be used in solving the problems discussed in this section. By using a commercial package, total fields can be reproduced, but scattered and/or diffracted fields cannot be discriminated without using the multi-step approach introduced here.

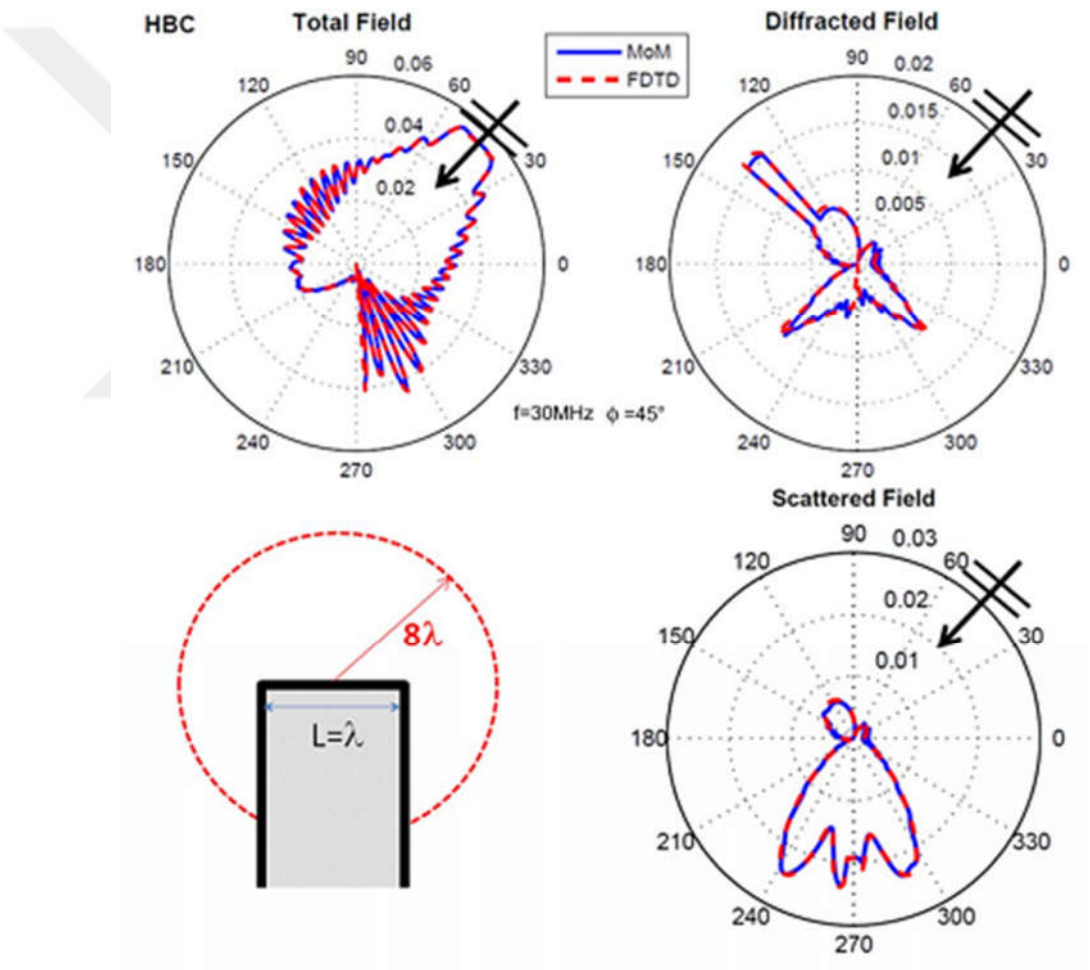

Figure 3.7 Total, diffracted, and scattered fields around Structure-1; $L=\lambda$, $\rho_0=10\lambda$, $\varphi_0=45°$, $\rho=8\lambda$, $f=30MHz$, TE/SBC case; Solid: MoM, Dashed: FDTD.

3.5. Conclusions

Time domain based double tip diffraction modeling is introduced with FDTD method. MoM approach is also discussed. MATLAB-based diffraction algorithm is developed and numerical results are presented. Very good agreement between the results shows that FDTD can be used effectively in double tip diffraction modeling. The novel multi-step multi-tip diffraction modeling introduced here is highly effective for FDTD. It can be extended to 3D. Since the power and beauty of these numerical models is their application capability directly in 3D, distinguishing and discriminating scattered and diffracted fields for the realistic objects in 3D would be very helpful in understanding and designing low-visible objects. Note that, the reader is referred to [64] - [67] for indoor, anechoic chamber measurement results which belong to 2D propagation above flat, perfectly reflecting surface with single and double diffractive obstacles.

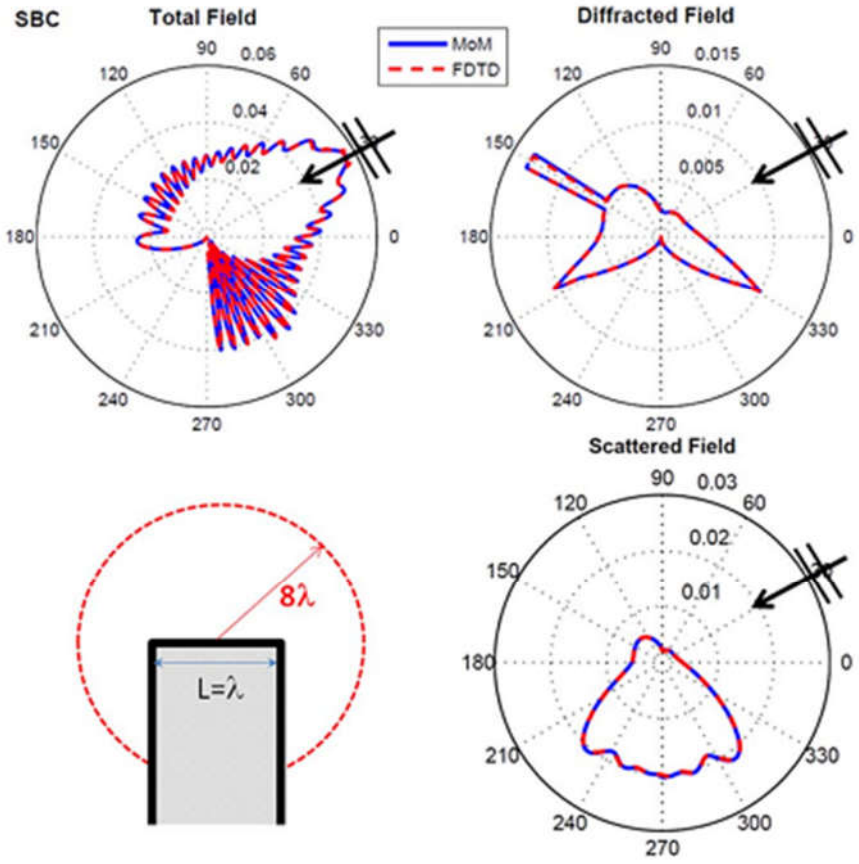

Figure 3.8 Total, diffracted, and scattered fields around Structure-1; $L=\lambda$, $\rho_0=10\lambda$, $\varphi_0=30°$, $\rho=8\lambda$, $f=30MHz$ TM/SBC case; Solid: MoM, Dashed: FDTD.

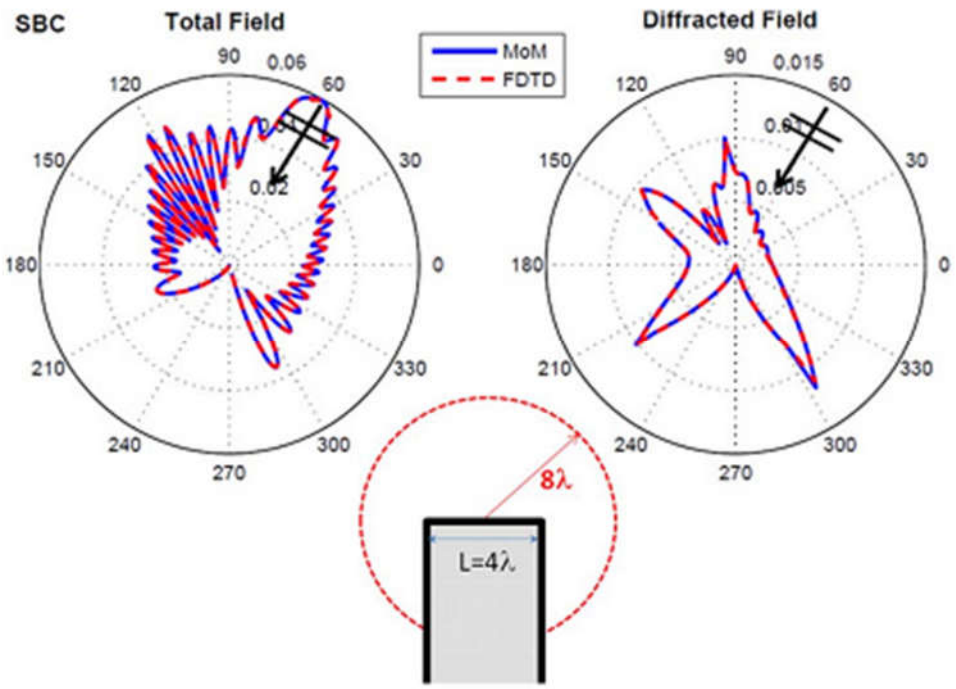

Figure 3.9 Total (Left) and diffracted (Right) fields around Structure-1 $L = 4\lambda$, $\rho_0 = 10\lambda$, $\varphi_0 = 60°$, $\rho = 10\lambda$, $f = 30MHz$ TM/SBC case; Solid: MoM, Dashed: FDTD.

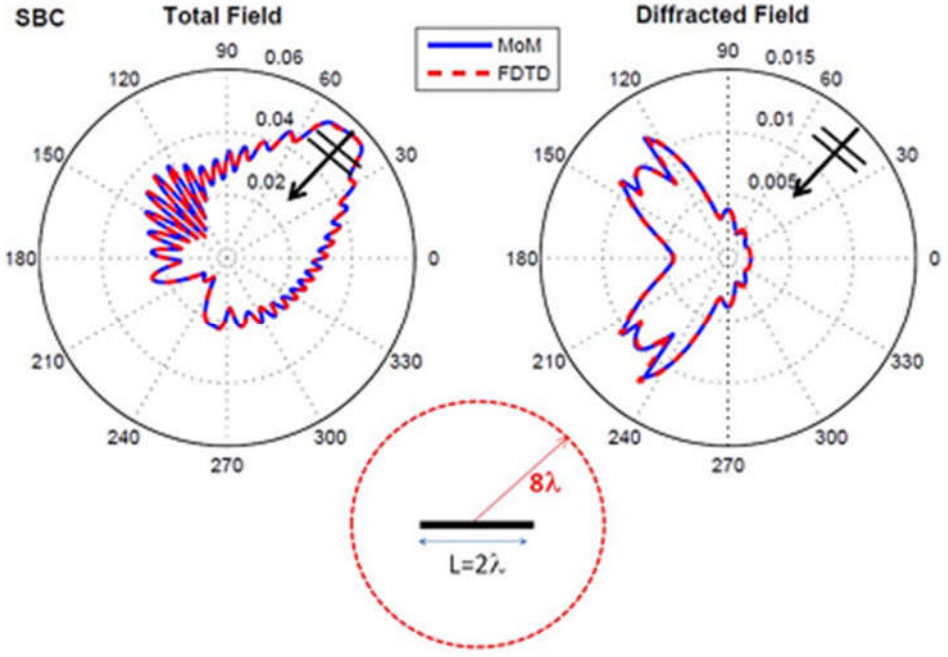

Figure 3.10 Total (Left) and diffracted (Right)fields around Structure-1 $L = 2\lambda$, $\rho_0 = 10\lambda$, $\varphi_0 = 45°$, $\rho = 8\lambda$, $f = 30MHz$ TM/SBC case; Solid: MoM, Dashed: FDTD

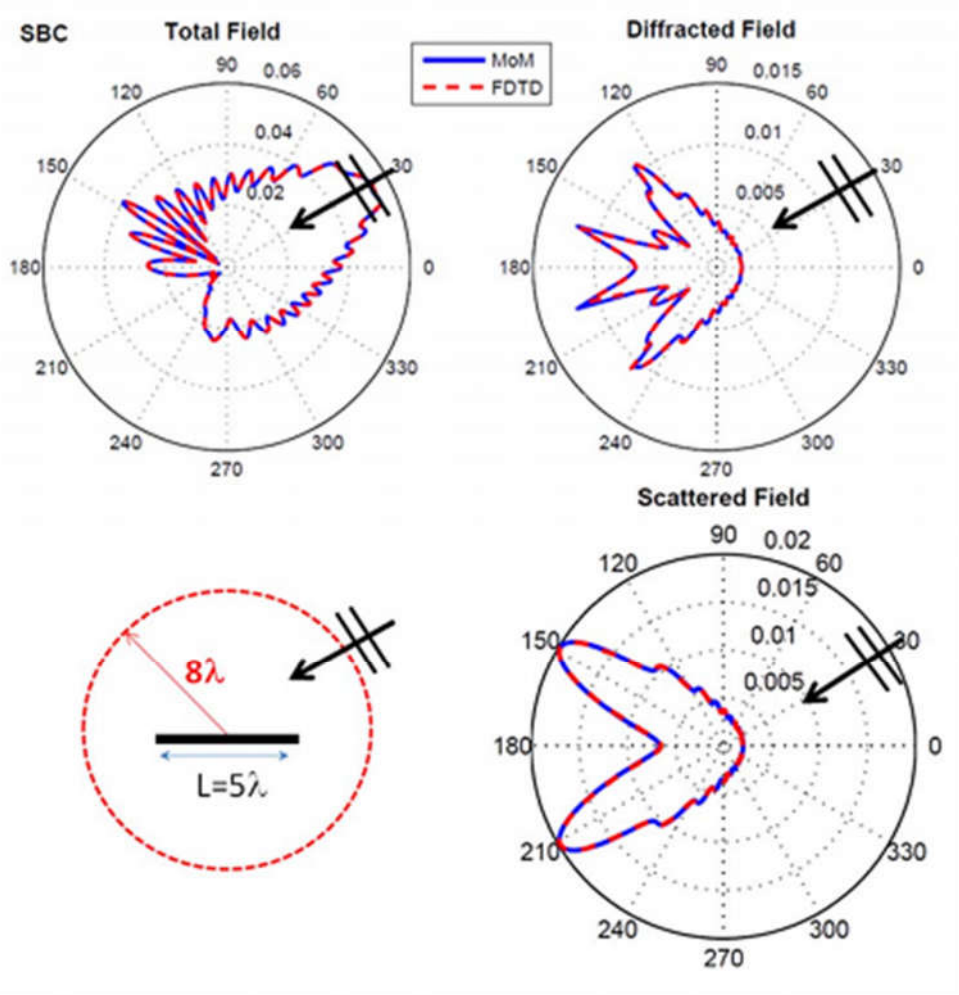

Figure 3.11 Total, diffracted, and scattered fields around Structure-1; $L = 5\lambda$, $\rho_0 = 10\lambda$, $\varphi_0 = 30°$, $\rho = 8\lambda$, $f = 30MHz$ TM/SBC case; Solid: MoM, Dashed: FDTD.

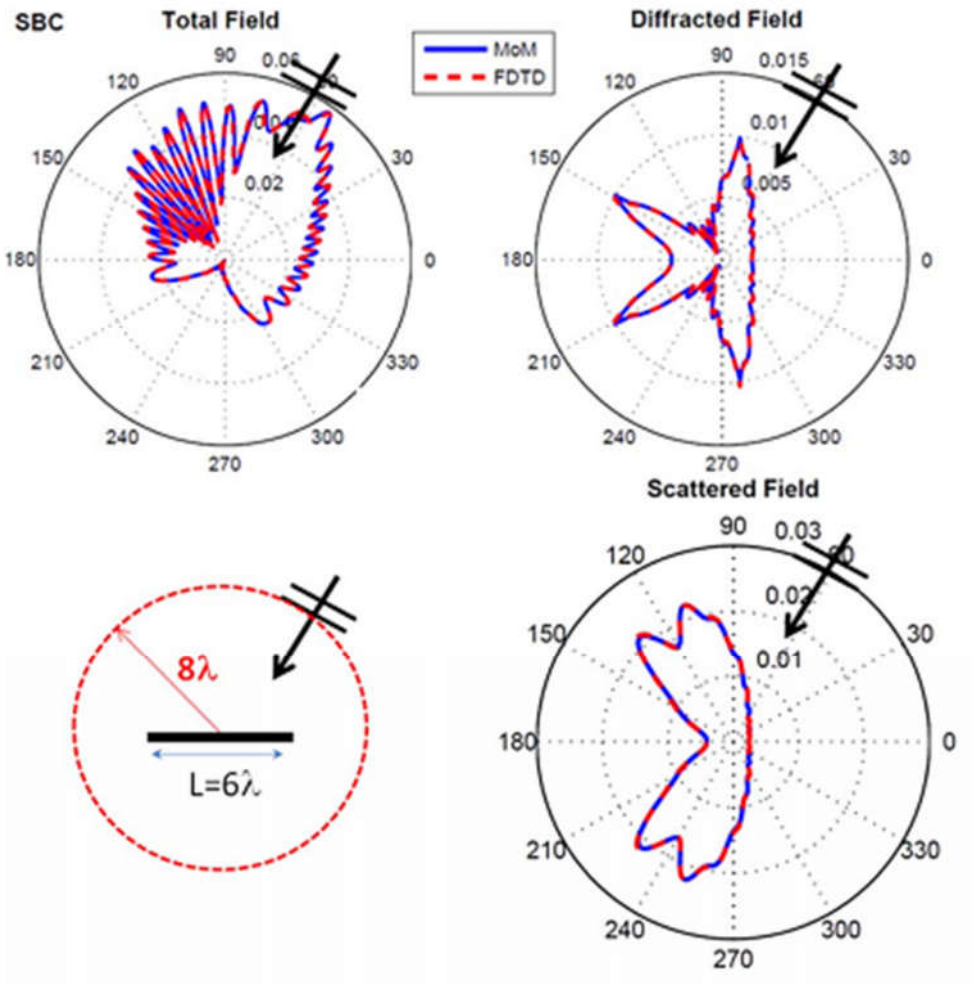

Figure 3.12 Total, diffracted, and scattered fields around Structure-1; $L = 6\lambda$, $\rho_0 = 10\lambda$, $\varphi_0 = 60°$, $\rho = 8\lambda$, $f = 30MHz$ TM/SBC case; Solid: MoM, Dashed: FDTD.

4. DIFFRACTION MODELING BY A SOFT-HARD STRIP

Most materials used in the aircrafts, ships, ballistic missiles are those whose static (d.c.) electrical conductance is very high i.e. on the order of 10^7. In diffraction problems, these materials are considered as perfect electric conductor [5]. In practice there is no real material with infinite conductivity but the assumption of PEC condition is very attractive for analytical and numerical methods because it is easy to model PEC objects. Perfect magnetic conductor (PMC) boundary condition is dual to the PEC boundary condition. There is no real magnetic conductor because there is no magnetic current. However, recent advances in technology have attracted interest in artificial PMCs which are also known as high impedance surfaces. Artificial PMCs are generally realized by using periodic dielectric substrates and multiple metallization patterns [68]. These materials are used in various EM applications e.g. they are used to reduce specific absorption rate (SAR) in mobile phones.

Electromagnetic field behavior on PEC and PMC material boundaries is governed by boundary conditions. For PEC materials, tangential component of electric field satisfies Dirichlet or Soft BC i.e. $\mathbf{E}_{\tan} = 0$ and magnetic field components satisfy Neumann or Hard BC i.e. $\frac{d\mathbf{H}}{dn} = 0$. Similar conditions can be derived for PMC materials by using the duality principle: tangential component of magnetic field satisfies Dirichlet or Soft B.C. and electric field components satisfy or Neumann or Hard BC. In electromagnetic terminology, Soft and Hard boundary conditions correspond to transverse electric (TE) and transverse magnetic (TM) problems with respect to surface normal e.g. in TM mode, tangential electric field components is equal to zero and normal electric field component is non-zero. Various aspects of soft/hard surface modeling were discussed in a special issue [69].

As stated in Chapter 2, electromagnetic diffraction behaves as a local phenomenon at high frequencies (when the wavelength is very small compare to the object size) thus, total diffracted field can be obtained by dividing the object into canonical geometries and summing up their individual contributions. 2D strip geometry is one of the canonical geometries and considered in this dissertation. Here, time domain diffraction model is introduced with FDTD method for a two-dimensional (2D) strip with one face soft (SBC)

and the other hard (HBC) BC and results are compared against existing MoM-based model [70]. Here, for the sake of completeness, the MoM procedure is also included and summarized.

The problem geometry is shown in Fig. 4.1. The cylindrical coordinates ρ,φ,z are used. Since the strip is assumed to be infinite along z direction, the problem can be reduced to two-dimension (2D) and handled in polar coordinates ρ,φ . The width of the strip is L. The origin is chosen at midpoint of the strip therefore the strip extends from edge to edge between $(0,L/2)$ and $(0,-L/2)$ on the y-axis. The numbers 1 and 2 show top and bottom edges, respectively. The left part of the strip has soft boundary condition while the right side has hard boundary condition. The line source is assumed on (ρ_0,φ_0). The dashed circle with radius ρ shows the locations of receivers. 360 receivers are located on this circle which yields $\Delta\varphi=1°$ angular resolution. According to the scenario shown in Fig. 4.1, reflections occur for the receivers located only between the lines L_1 and L_2. The incident field exists everywhere except the shadow region shown in between the lines SB_1 and SB_2. The two tips are responsible for the creation of the diffracted fields which exist everywhere.

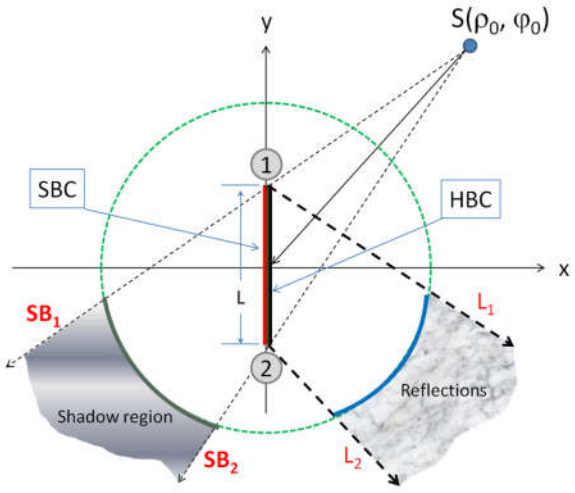

Figure 4.1 The strip structure. The left side is soft ($u = 0$), the right side is hard ($du / dn = 0$). The width of the strip is L. Numbers 1 ($x = 0, y = L/2$) and 2 ($x = 0, y = -L/2$) denote edge points.

We consider here the total and diffracted waves induced on a strip having zero impedance (Dirichlet BC) on one (left) face ($u = 0$) and infinite impedance (Neumann BC) on the

other (right) face $\left(\partial u / \partial n = 0\right)$. The total field $u(\rho,\phi)$ around the strip satisfies the wave equation

$$\left(\frac{\partial^2}{\partial\rho^2}+\frac{1}{\rho}\frac{\partial}{\partial\rho}+\frac{1}{\rho^2}\frac{\partial^2}{\partial\phi^2}+k^2\right)u = I_0\delta\left(\rho-\rho_0\right)\frac{1}{\rho}\delta\left(\phi-\phi_0\right) \tag{4.1}$$

and boundary conditions

$$u = 0 \text{ (SBC) on the left face of the strip,} \tag{4.2}$$

$$\frac{\partial u}{\partial n} = 0 \text{ (HBC) on the right face of the strip,} \tag{4.3}$$

and the Sommerfeld's Radiation Condition (SRC) at infinity:

$$\lim_{p->\infty}\sqrt{k\rho}\left(\frac{\partial u}{\partial\rho}-iku\right)=0, \tag{4.4}$$

under a line source illumination at $u(\rho_0,\varphi_0)$. Here, k is the wave number. Note that, $\partial u / \partial n = \partial u / \partial x$ for the scenario pictured in Fig. 4.1. The source becomes plane wave when $\rho_0 \to \infty$. Plane wave illumination and $\exp(-i\omega t)$ time dependence are assumed in this model.

4.1. FDTD Model

The object under investigation is located in the middle of FDTD space. The space left for the air and termination which simulates the free space is around $3\lambda - 5\lambda$ on both axes. Therefore, any $20\lambda \times 20\lambda$ object can be investigated in this FDTD space. This corresponds far into quasi-optical and optical scattering frequency regime, therefore comparisons with HFA is possible. Due to finite nature of FDTD grid, the strip is modeled as one cell wide as shown in Fig. 4.2. Assuming the left and right faces of the strip at i=N^{th} and i=$(N+1)^{th}$ cells respectively, the SBC and HBC boundary conditions will be satisfied using ($u = 0$ or $E_z(N) = 0$) and $\partial u / \partial n = 0$ or $E_z(N+1) = E_z(N+2)$ respectively, along all vertical cells on the strip. Diffracted fields are extracted from total fields by applying a 3-step procedure similar to [49] as follows:

1) FDTD simulation is run with the strip and time domain values of the fields at the receivers are recorded on the observation circle. Total fields are obtained at the end of this step.
2) The strip is replaced by a full plane (i.e., the strip is extended to infinity vertically on both ends) and the FDTD simulation is re-run. The recorded time domain data at the receivers on the source side only contain incidence and reflected fields.

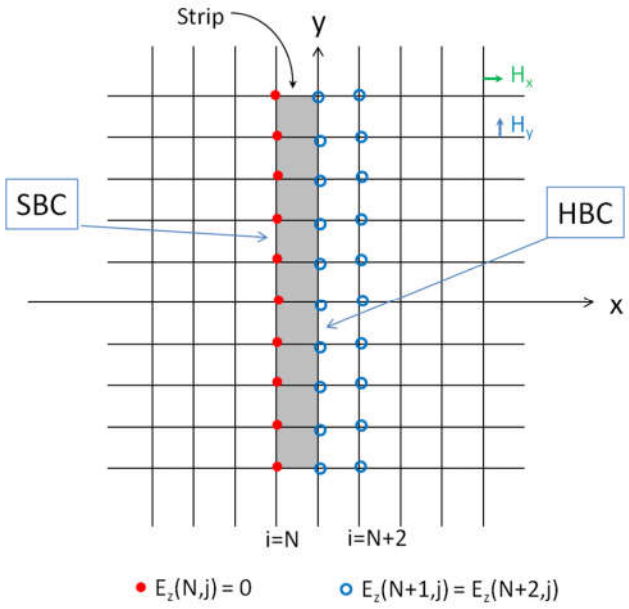

Figure 4.2 FDTD modeling of the SHBC strip (Left Face: SBC, Right face: HBC, Strip width is one FDTD cell).

3) The strip is removed and the FDTD simulation is run in the free space without having any objects. The recorded time domain data at all the receivers include only incident fields.

Once 3-step procedure is completed, the time data obtained from step 2 is subtracted from the time data obtained from step 1 within upper reflection boundaries. The resulting time data contains only incident and diffracted fields (I+D data). Then, the time data obtained from step 3 is subtracted from the I+D data within left or right reflection boundaries depending on the incidence angle. Once this step is completed, only diffracted fields will exist in simulation area. A sample plot for both total and scattered fields around the SHBC strip is shown in Fig. 4.3. Here, the source is a plane wave incident at $45°$ and hits the strip from the hard face. As observed in the top plot, there is a shadow region behind the strip

where only edge-diffracted waves appear. The bottom plot shows that forward scattering and specular reflections are dominant. Edge diffractions are also observable in the figures. Note that, incident fields are subtracted from the top plot and scattered-only fields around the strip are obtained.

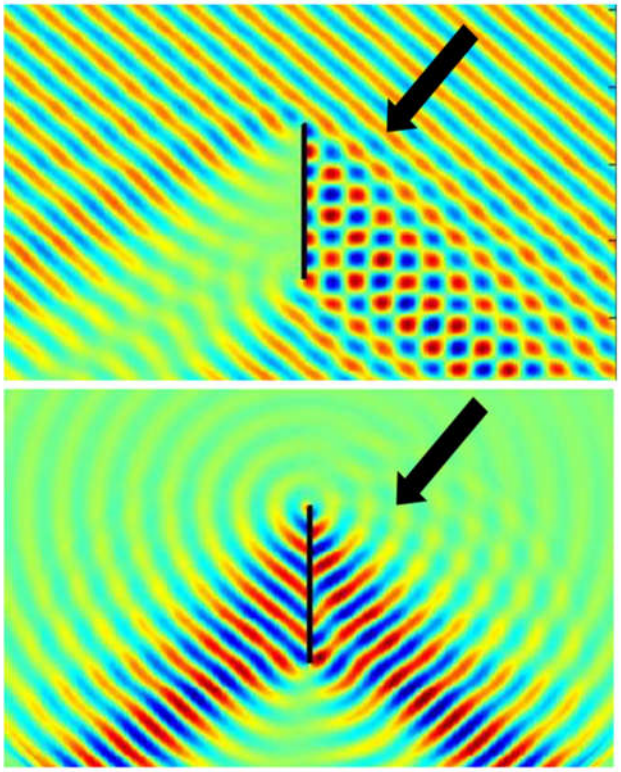

Figure 4.3 FDTD-generated (Top) total and (Bottom) scattered fields around the SHBC strip.

4.2. MoM Model

MoM has recently been successfully used in modeling diffraction from a strip with one face soft, the other hard and compared with physical theory of diffraction (PTD) results [70]. Here, integral equations and the procedure are summarized for the sake of completeness.

In the classical MoM approach, the faces of the strip are divided into small segments. The field $u(\boldsymbol{\rho}')$ and/or its derivative $\hat{n}\cdot\nabla u(\boldsymbol{\rho}') = \partial u(\boldsymbol{\rho}')/\partial n$ with respect to the normal on the surface (C) on each segment are assumed to be constant. The Green function of the problem is postulated via

$$\nabla^2 G(\boldsymbol{\rho},\boldsymbol{\rho}') + k^2 G(\boldsymbol{\rho},\boldsymbol{\rho}') = -\delta(\boldsymbol{\rho}-\boldsymbol{\rho}') \tag{4.5}$$

where $G(\boldsymbol{\rho},\boldsymbol{\rho}')$ is the scalar Green function and the source is represented with the Dirac delta $\delta(\cdot)$; $\boldsymbol{\rho}'$ and $\boldsymbol{\rho}$ show the position of the source and observer, respectively. The field u satisfies homogeneous part of (4.5). The total field is obtained for $\boldsymbol{\rho}' \in C$ and $\boldsymbol{\rho} \in V$ as:

$$u(\boldsymbol{\rho}) = u^{inc}(\boldsymbol{\rho}) + \int_C \left(u(\boldsymbol{\rho}') \frac{\partial G(\boldsymbol{\rho},\boldsymbol{\rho}')}{\partial n} - \frac{\partial u(\boldsymbol{\rho}')}{\partial n} G(\boldsymbol{\rho},\boldsymbol{\rho}') \right) d\rho' \tag{4.6}$$

The form suitable for MoM computations is obtained when the observer is placed on the surface $\boldsymbol{\rho}', \boldsymbol{\rho} \in C$:

$$u^{inc}(\boldsymbol{\rho}) = \frac{u(\boldsymbol{\rho})}{2} - \int_{C-\{\boldsymbol{\rho}=\boldsymbol{\rho}'\}} \left(u(\boldsymbol{\rho}') \frac{\partial G(\boldsymbol{\rho},\boldsymbol{\rho}')}{\partial n} \right) d\rho' + \int_C \left(\frac{\partial u(\boldsymbol{\rho}')}{\partial n} G(\boldsymbol{\rho},\boldsymbol{\rho}') \right) d\rho' \tag{4.7}$$

Here, the Green function and its normal derivative, respectively, are

$$G(\boldsymbol{\rho},\boldsymbol{\rho}') = \frac{i}{4} H_0^{(1)}\left(k\left|\boldsymbol{\rho}-\boldsymbol{\rho}'\right|\right) \tag{4.8}$$

$$\frac{\partial G(\boldsymbol{\rho},\boldsymbol{\rho}')}{\partial n} = \frac{ik}{4} H_1^{(1)}\left(k\left|\boldsymbol{\rho}-\boldsymbol{\rho}'\right|\right) \frac{\boldsymbol{\rho}'-\boldsymbol{\rho}}{\left|\boldsymbol{\rho}-\boldsymbol{\rho}'\right|} \cdot \hat{n} \tag{4.9}$$

A. Backscattering by a Soft Strip (SBC)

The total field on the surface is zero ($u_z = 0$) for non-penetrable soft strip (Dirichlet BC) and the scattered field is

$$u_z^{sct}(\boldsymbol{\rho}) = -\frac{i}{4} \int_C \frac{\partial u_z(\boldsymbol{\rho}')}{\partial n} H_0^{(1)}\left(k\left|\boldsymbol{\rho}-\boldsymbol{\rho}'\right|\right) d\rho' \tag{4.10}$$

If $\boldsymbol{\rho}', \boldsymbol{\rho} \in C$ on the surface, $u_z^{inc} = -u_z^{sct}$ as follows:

$$u_z^{inc}(\boldsymbol{\rho}) = \frac{i}{4} \int_C \frac{\partial u_z(\boldsymbol{\rho}')}{\partial n} H_0^{(1)}\left(k\left|\boldsymbol{\rho}-\boldsymbol{\rho}'\right|\right) d\rho' \tag{4.11}$$

Necessary MoM equations in this procedure are

$$V_m = \sum_{n=1}^{N} Z_{mn} \frac{\partial u_z(\boldsymbol{\rho}_n)}{\partial n} \tag{4.12}$$

where V_m denotes the incident field at matching points $(\boldsymbol{\rho}_m)$

$$V_m = u_z^{inc}(\boldsymbol{\rho}_m) = e^{-ik(x_m \cos\phi_0 + y_m \sin\phi_0)} \tag{4.13}$$

and the impedance matrix is

$$Z_{mn} \approx \frac{i}{4}\Delta s_n \times \begin{cases} H_0^{(1)}\left(k\left|\boldsymbol{\rho}_m - \boldsymbol{\rho}_n\right|\right) & m \neq n \\ 1 + i\frac{2}{\pi}\ln\left(\frac{\gamma k \Delta s_n}{4e}\right) & m = n \end{cases} \tag{4.14}$$

where Δs_n is the nth segment length, $H_0^{(1)}$ is the first kind Hankel function with order zero, $\gamma \approx 1.781$ is the exponential of the Euler constant, $\boldsymbol{\rho}_m$ and $\boldsymbol{\rho}_n$ show the observer and the segment source points, respectively. After obtaining unknown coefficients $\partial u_z\left(\boldsymbol{\rho}_n\right)/\partial n$ from (4.12), the scattered fields are calculated using (4.10).

B. Backscattering by a Hard Strip (HBC)

The total field derivative with respect to normal on the surface is zero ($\partial u_z / \partial n = 0$) for non-penetrable hard strip (Neumann BC) and the scattered field is

$$u_z^{sct}(\boldsymbol{\rho}) = \frac{ik}{4}\int_C \left(u_z(\boldsymbol{\rho}') H_1^{(1)}\left(k\left|\boldsymbol{\rho}' - \boldsymbol{\rho}\right|\right) \frac{\boldsymbol{\rho} - \boldsymbol{\rho}'}{\left|\boldsymbol{\rho}' - \boldsymbol{\rho}\right|} \cdot \hat{n} \right) d\rho' \tag{4.15}$$

where $H_1^{(1)}$ is the first kind Hankel function with order one. If $\boldsymbol{\rho}', \boldsymbol{\rho} \in C$ on the surface,

$$u_z^{inc}(\boldsymbol{\rho}) = \frac{u_z(\boldsymbol{\rho})}{2} - \frac{ik}{4}\int_C \left(u_z(\boldsymbol{\rho}') H_1^{(1)}\left(k\left|\boldsymbol{\rho}' - \boldsymbol{\rho}\right|\right) \frac{\boldsymbol{\rho} - \boldsymbol{\rho}'}{\left|\boldsymbol{\rho}' - \boldsymbol{\rho}\right|} \cdot \hat{n} \right) d\rho' \tag{4.16}$$

Necessary MoM equations in this procedure are

$$V_m = \sum_{n=1}^{N} Z_{mn} u_z(\boldsymbol{\rho}_n) \tag{4.17}$$

where V_m denotes the incident field given in (4.13) at matching points ($\boldsymbol{\rho}_m$) and the impedance matrix is

$$Z_{mn} \approx \begin{cases} -\dfrac{ik}{4}\Delta s_n H_1^{(1)}\left(k\left|\boldsymbol{\rho}_m - \boldsymbol{\rho}_n\right|\right)\dfrac{\boldsymbol{\rho}_m - \boldsymbol{\rho}_n}{\left|\boldsymbol{\rho}_m - \boldsymbol{\rho}_n\right|}\cdot\hat{n}_n & m \neq n \\ 0.5 & m = n \end{cases} \tag{4.18}$$

where $\hat{n}_n$ denotes the unit normal vector of the segment at $\boldsymbol{\rho}_n$. After obtaining unknown coefficients $u_z(\boldsymbol{\rho}_n)$ from (4.17), the scattered fields are calculated using (4.15).

C. Backscattering by a Soft-Hard Strip (SHBC)

If the left side of the strip is soft and the right side of the strip is hard, then (4.6) should be considered where the scattered field is

$$u^{sct}(\boldsymbol{\rho}) = \int_C \left(u(\boldsymbol{\rho}')\frac{\partial G(\boldsymbol{\rho},\boldsymbol{\rho}')}{\partial n} - \frac{\partial u(\boldsymbol{\rho}')}{\partial n} G(\boldsymbol{\rho},\boldsymbol{\rho}') \right) d\rho' \tag{4.19}$$

The rule is to use $u_{x<0} = 0$ (SBC case) for the left side ($x<0$) and $\partial u_{x>0}/\partial x = 0$ (HBC case) for the right side ($x>0$) on the strip. The unknown coefficients are $\partial u_z(\boldsymbol{\rho}_n)/\partial n$ and $u_z(\boldsymbol{\rho}_n)$ for the left and right sides of the strip, respectively.

<u>On the left face of the strip (SBC case):</u>

$$\begin{aligned} u^{inc}(\boldsymbol{\rho})_{x<0} = {} & \frac{i}{4}\int_C \frac{\partial u(\boldsymbol{\rho}')_{x<0}}{\partial n} H_0^{(1)}\left(k\left|\boldsymbol{\rho}-\boldsymbol{\rho}'\right| d\rho'\right) \\ & -\frac{ik}{4}\int_C \left(u(\boldsymbol{\rho}')_{x>0} H_1^{(1)}\left(k\left|\boldsymbol{\rho}'-\boldsymbol{\rho}\right|\right)\frac{\boldsymbol{\rho}-\boldsymbol{\rho}'}{\left|\boldsymbol{\rho}'-\boldsymbol{\rho}\right|}\cdot\hat{n} \right) d\rho' \end{aligned} \tag{4.20}$$

<u>On the right face of the strip (HBC case):</u>

$$\begin{aligned} u^{inc}(\boldsymbol{\rho})_{x>0} = {} & \frac{u(\boldsymbol{\rho})_{x>0}}{2} \\ & -\frac{ik}{4}\int_C \left(u(\boldsymbol{\rho}')_{x>0} H_1^{(1)}\left(k\left|\boldsymbol{\rho}'-\boldsymbol{\rho}\right|\right)\frac{\boldsymbol{\rho}-\boldsymbol{\rho}'}{\left|\boldsymbol{\rho}'-\boldsymbol{\rho}\right|}\cdot\hat{n} \right) d\rho' \\ & +\frac{i}{4}\int_C \frac{\partial u(\boldsymbol{\rho}')_{x<0}}{\partial n} H_0^{(1)}\left(k\left|\boldsymbol{\rho}-\boldsymbol{\rho}'\right| d\rho'\right) \end{aligned} \tag{4.21}$$

The four-step MoM procedure with SHBC is implemented as follows:

1) Source-excited segment fields are calculated using (4.13),

2) The impedance matrix system in (4.14) and (4.17) is built with respect to (4.20) and (4.21),
3) The segment fields and/or its derivatives are calculated numerically from the solution of the derived system of equations,
4) The segment-scattered fields at the observer are then accumulated using (4.18).

4.3. Examples and Comparisons

MATLAB algorithms are developed for both FDTD- and MoM-based diffraction modeling and are run for different sets of parameters. Examples given in Figs. 4.4-4.9 present total and diffracted fields around SBC, HBC, and SHBC strips.

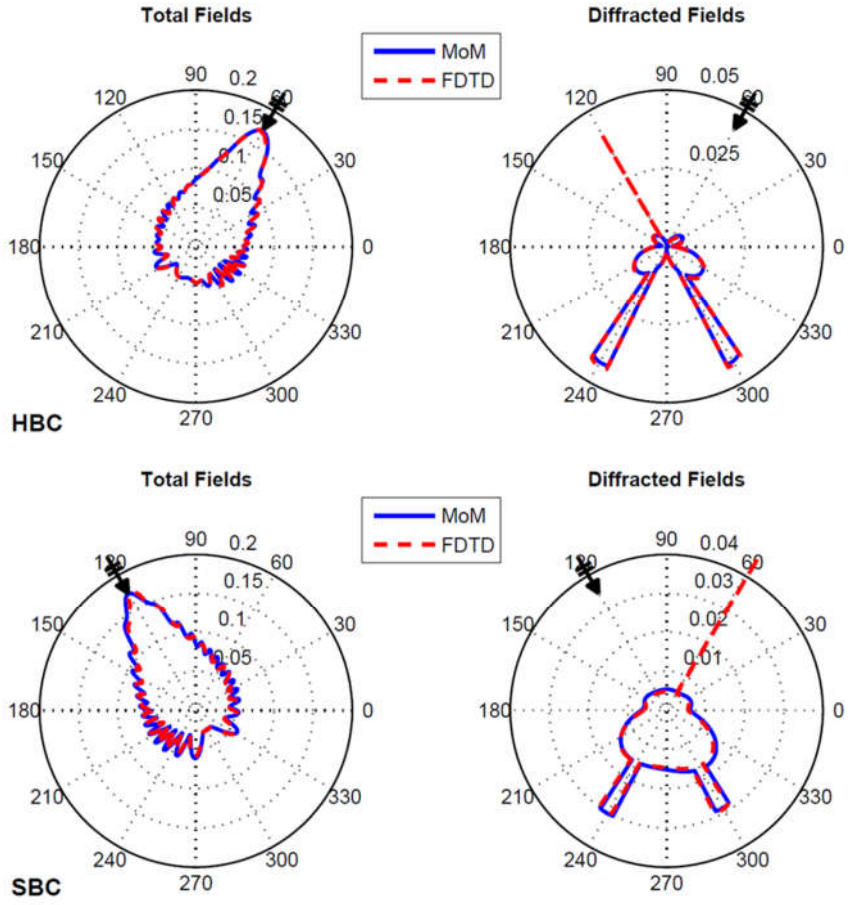

Figure 4.4 Total (Left) and diffracted (right) fields around the strip: (Top) HBC, $\varphi_0 = 60°$, (Bottom) SBC, $\varphi = 120°$ ($f = 30MHz$, $L = \lambda$, $\rho_0 = 8\lambda$, $\rho = 7\lambda$ Solid: MoM, Dashed: FDTD).

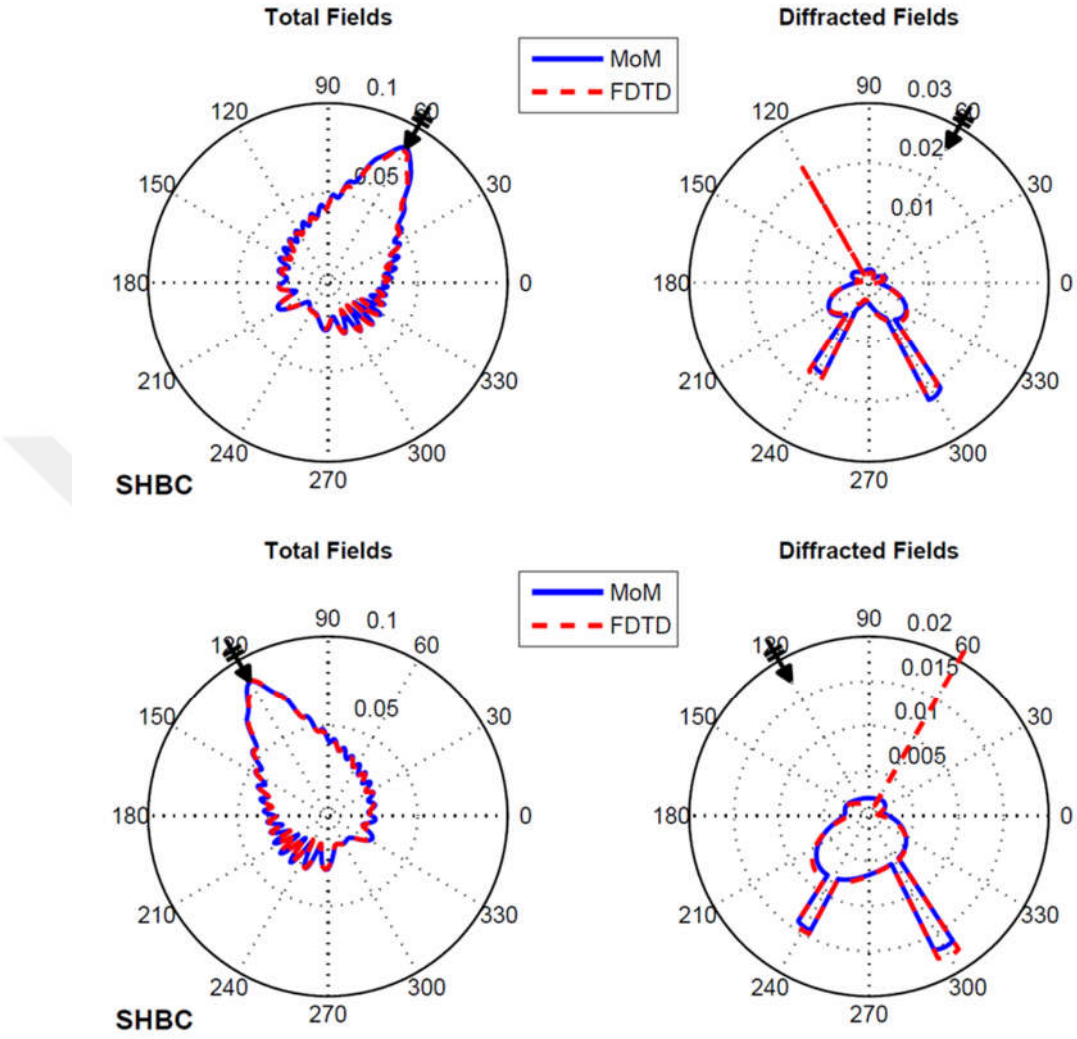

Figure 4.5 Total (Left) and diffracted (right) fields around the SHBC strip: (Top), $\varphi_0 = 60°$, (Bottom), $\varphi_0 = 120°$, ($f = 30MHz$, $L = \lambda$, $\rho_0 = 8\lambda$, $\rho = 7\lambda$ Solid: MoM, Dashed: FDTD).

In Fig. 4.4, total and diffracted fields around both HBC and SBC strips, computed with both FDTD and MoM approaches are shown. The strip size is 10 m and this corresponds to 1-wavelength at 30 MHz. The line source is 8-wavelengths away from the origin. The receivers / observers are located along a circular path having a radius of 7-wavelengths. The agreement is very good, as observed.

The dominant diffraction occurs along the two critical boundaries incident shadow boundary (ISB) and Reflection Shadow Boundary (RSB). Note that, FDTD uses 1-cell thick strip and this causes a strong, non-physical reflections (see, the red line along the specular reflection direction).

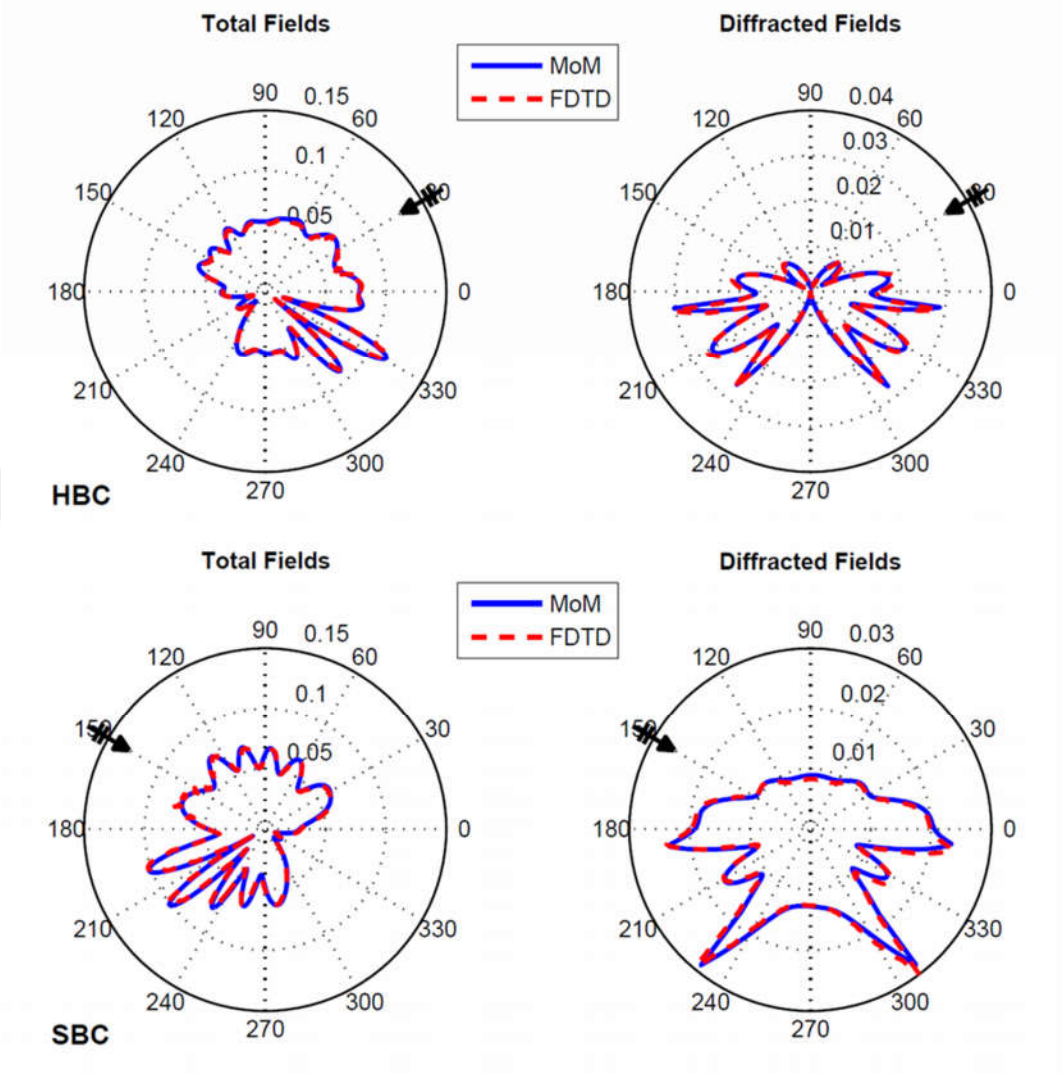

Figure 4.6 Total (Left) and diffracted (right) fields around the strip: (Top) HBC, $\varphi_0 = 30°$, (Bottom) SBC, $\varphi_0 = 150°$, ($f = 30MHz$, $L = 2\lambda$, $\rho_0 = 10\lambda$, $\rho = 3\lambda$ Solid: MoM, Dashed: FDTD).

Figure 4.5 belongs to the same comparisons but for the SHBC strip. Finally, Figs. 4.6-4.9 belong to simulations for 2-wavelength strip. The effects of SHBC strip are shown in Figs. 4.7 and 4.9 compared to SBC and HBC strip in Figs. 4.6 and 4.8, respectively. The FDTD diffracted fields for SBC, HBC and SHBC strip are also shown together in Fig. 4.10. As can be observed from Fig. 4.10, diffraction from hard surfaces is stronger than from soft surfaces. Using SHBC strip does not change the magnitude of diffracted fields significantly at the hard side of strip. On the other hand, the magnitude of diffracted fields at the soft side of strip is almost average of the SBC and HBC diffracted fields.

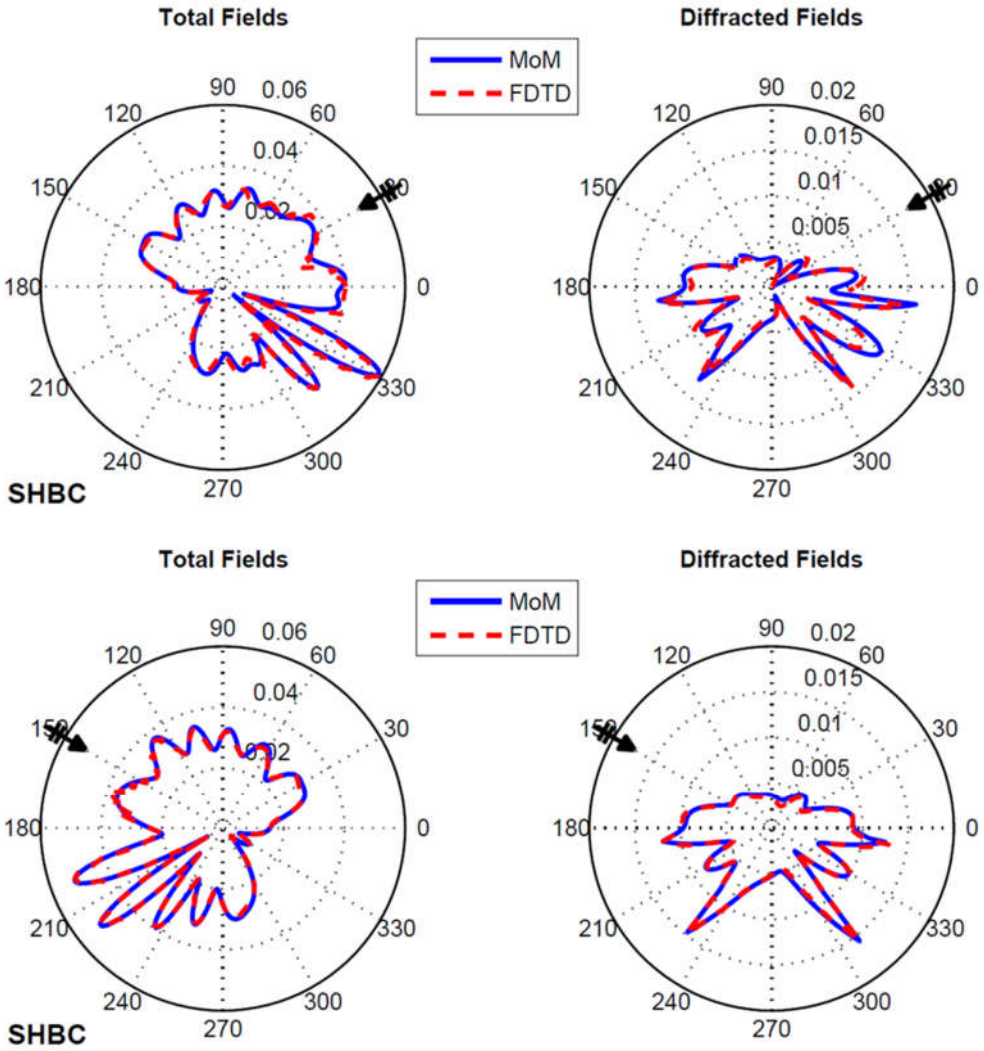

Figure 4.7 Total (Left) and diffracted (right) fields around the SHBC strip: (Top), $\varphi_0 = 30°$, (Bottom), $\varphi_0 = 150°$ ($f = 30MHz$, $L = 2\lambda$, $\rho_0 = 10\lambda$, $\rho = 3\lambda$ Solid: MoM, Dashed: FDTD).

4.4. Conclusions

Diffraction by a strip with one face soft boundary condition and the other hard, is modeled numerically using the FDTD method. Results are compared against MoM. The very good agreement observed between proposed model and existing MoM-based model confirms the validity of proposed model. The advantage of the proposed model over existing MoM-based model is that broadband diffracted fields can be obtained in a single run. Also diffraction from SHBC strip can be analyzed in time step by step. Although the strip

considered does not exist in real life, the results obtained in this section can be used as a future reference.

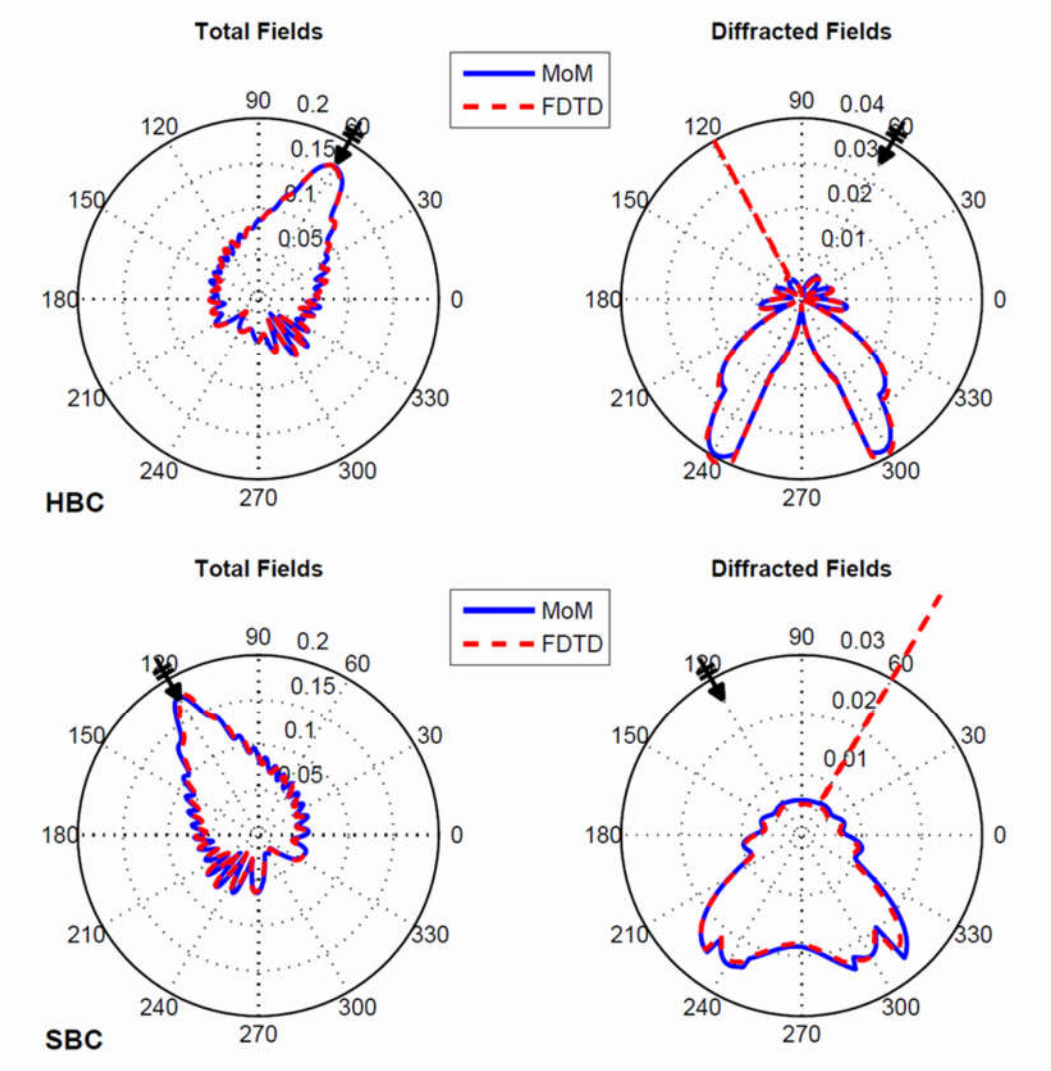

Figure 4.8 Total (Left) and diffracted (right) fields around the trip: (Top) HBC, $\varphi_0 = 60°$, (Bottom) SBC, $\varphi_0 = 120°$ ($f = 30MHz$, $L = 2\lambda$, $\rho_0 = 8\lambda$, $\rho = 7\lambda$ Solid: MoM, Dashed: FDTD).

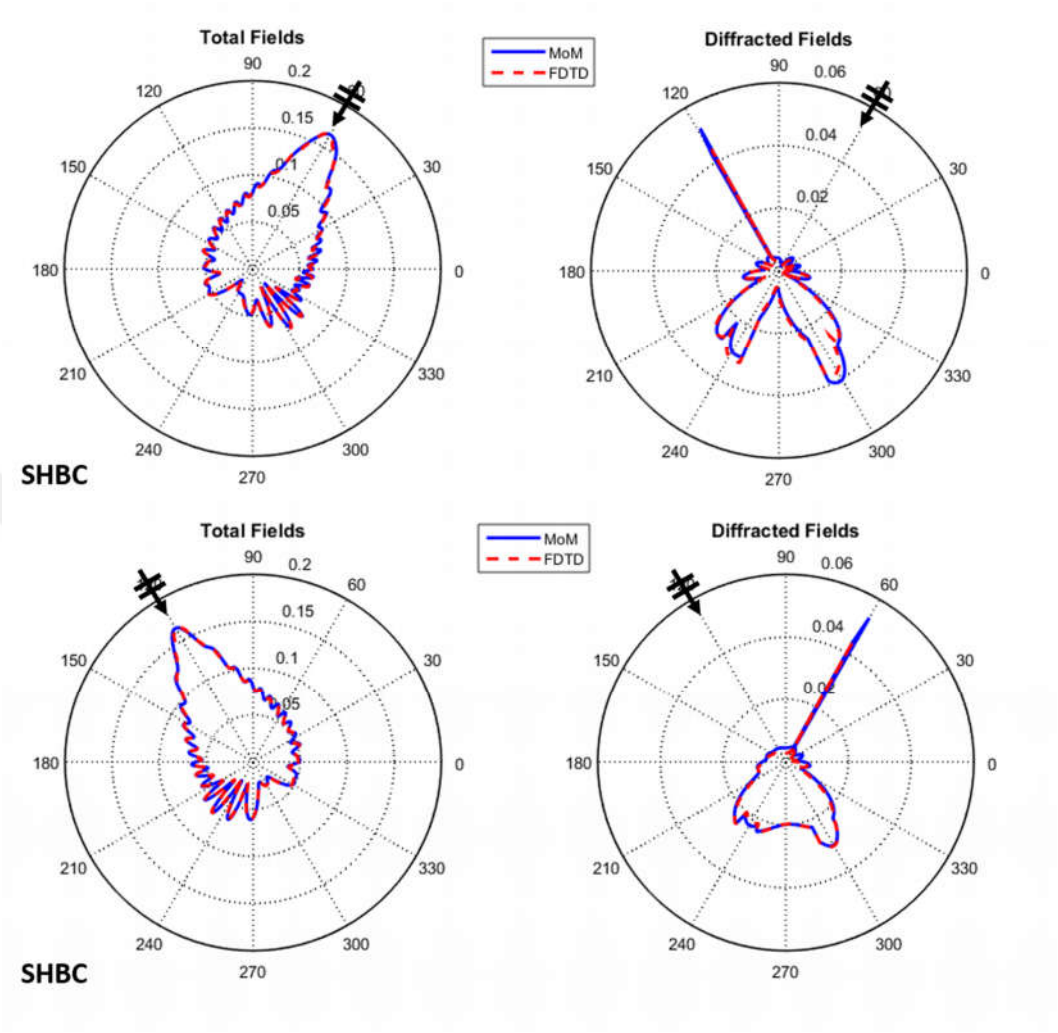

Figure 4.9 Total (Left) and diffracted (right) fields around the SHBC strip: (Top), $\varphi_0 = 60°$, (Bottom), $\varphi_0 = 120°$ ($f = 30MHz$, $L = 2\lambda$, $\rho_0 = 8\lambda$, $\rho = 7\lambda$ Solid: MoM, Dashed: FDTD).

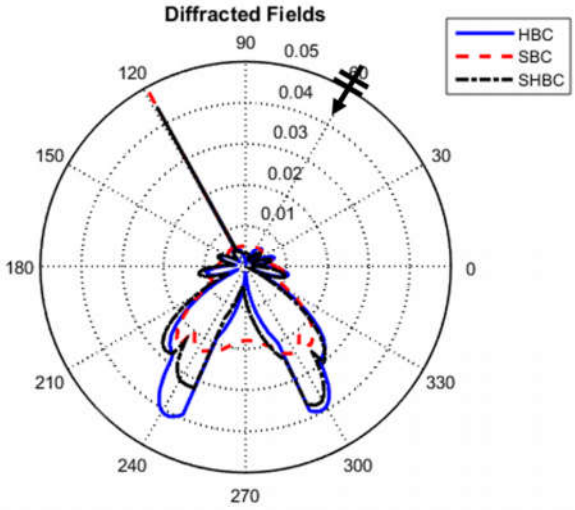

Figure 4.10 FDTD computed diffracted fields around the SHBC strip: $\varphi_0 = 60°$ ($f = 30MHz$, $L = 2\lambda$, $\rho_0 = 8\lambda$, $\rho = 7\lambda$ Solid: MoM, Dashed: FDTD).

5. TIME DOMAIN MODELING OF FRINGE WAVES

When electromagnetic wave encounters an object that has different electrical characteristics from propagating medium, currents are induced in the object body. If the object is comprised of metallic materials as in case of most realistic targets such as aircrafts, ships etc. then the currents are concentrated on the surface and referred to surface currents. These induced currents give rise to scattered field which is formed by diffracted, reflected and refracted fields. For metallic objects, penetration of field inside object body can be neglected and scattered field contains only diffracted and reflected fields. Source-based EM techniques intend to find out induced currents on the scattering objects via the known incident fields. Once these currents are found, scattered fields are easily calculated with well-known radiation integrals (also named as Stratton-Chu equations) [14].

Physical optics (PO), introduced by Macdonald in 1912, is a HFA technique used for the calculations of scattered fields from PEC objects [71]. PO is a source-based technique where currents are assumed to be induced on an infinite PEC plane tangent to the object. PO source-induced currents, which are non-zero only on the illuminated side of object's surface (away from any discontinuity), are named as uniform currents. PO-based scattered fields consist of reflected + diffracted fields and yield inaccurate results for the objects having discontinuities such as sharp edges and/or tips. This is because the magnitude of the induced currents near a discontinuity is not uniformly distributed. In other words, diffraction is not modeled properly with PO's uniform current approximation.

Physical theory of diffraction (PTD) extends PO by introducing fringe (non-uniform) currents. The PTD scattered fields contain contributions of both uniform (PO) currents and non-uniform (fringe) currents [5]. The fields radiated from fringe currents are called fringe waves and they constitute the portion of diffracted fields. Understanding and investigation of fringe waves are critical in broad range of electromagnetic (EM) problems, such as radar cross section, propagation, electromagnetic compatibility modeling and simulation. The canonical wedge structure has long been used for this purpose. For example, exact and asymptotic formulations of fringe waves are given in [6] for a PEC wedge illuminated by a plane wave and in [72] for the line source illumination. A novel MoM-based approach also introduced recently [15].

More information about both PO and PTD can be found in Chapter 2. In this dissertation, a novel FDTD method for the extraction of fringe currents on the canonical PEC wedge structure is proposed. The fringe fields are also computed via Green's function based on FDTD-extracted fringe currents.

The geometry of the problem is shown in Fig.5.1. Here, a 2D PEC wedge with apex angle α is illuminated by a line source located at (ρ_0,φ_0). The tip of the wedge is at the origin. The receivers are located at points (ρ,φ). The incident EM wave hits the wedge and induces surface current. This induced current is comprised of uniform (PO) and non-uniform (Fringe) parts [5]. Non-uniform currents cause fringe fields that constitute the portion of diffracted fields.

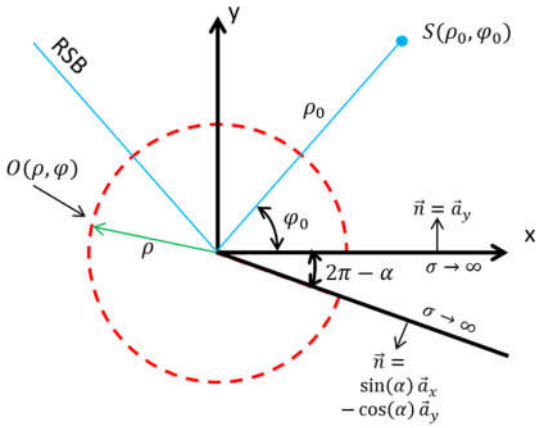

Figure 5.1 Geometry of the problem under single side illumination (SSI) illumination Problem Definition

As indicated in Chapter 2, PTD fringe fields are obtained by subtracting PO diffracted fields from total/exact diffracted fields:

$$u^{fringe} = u^{d,Exact} - u^{d,PO} \tag{5.1}$$

Here, exact diffracted fields $u^{d,exact}$ can be obtained from both integral and series summation representations [5, 6, 73]. Below, the integral solution is given for the sake of completeness for both soft (TM) and hard (TE) boundary condition respectively:

$$\begin{aligned} u_s^d = &\{V_d(-\pi-\varphi+\varphi_0) - V_d(\pi-\varphi+\varphi_0)\} \\ &-\{V_d(-\pi-\varphi-\varphi_0) - V_d(\pi-\varphi-\varphi_0)\} \end{aligned} \tag{5.2}$$

$$u_h^d = \{V_d(-\pi-\varphi+\varphi_0) - V_d(\pi-\varphi+\varphi_0)\} + \{V_d(-\pi-\varphi-\varphi_0) - V_d(\pi-\varphi-\varphi_0)\} \tag{5.3}$$

where

$$V_d\{\beta\} = \frac{1}{2\pi n}\int_0^\infty H_0^{(1)}[kR(it)]\frac{\sin(\beta/n)}{\cosh(t/n)-\cos(\beta/n)}dt \tag{5.4}$$

with $n = \alpha/\pi$ and $R(\eta) = \sqrt{r^2 + r_0^2 + 2rr_0 cos(\eta)}$. PO diffracted fields are given as [4]:

$$u_{s,h}^{d,PO}(r,\varphi) = u^{d,inc} + u_{s,h}^{d,refl} \tag{5.5}$$

where

$$u^{d,inc}(r,\varphi) = \frac{kr\sin(\varphi-\varphi_0)}{4i}\int_0^\infty H_0^{(1)}[k(r_0+r')]H_0^{(1)}(kp^-)\frac{dr'}{\rho^-} \tag{5.6}$$

with $\rho^- = \sqrt{r^2 + r'^2 + 2rr'^2 cos(\varphi-\varphi_0)}$ and

$$u_s^{d,refl}(r,\varphi) = -\frac{1}{4i}kr\sin(\varphi+\varphi_0) \cdot\int_0^\infty H_0^{(1)}[k(r_0+r')]H_1^{(1)}(kp^+)\frac{dr'}{p^+} \tag{5.7}$$

with $\rho^+ = \sqrt{r^2 + r'^2 + 2rr'^2 cos(\varphi+\varphi_0)}$. The term $u_h^{d,refl}$ is used for hard BC and expressed by the opposite of (5.7). Numerical computation of this integral representation is discussed in [74].

5.1. FDTD Model

The source-induced surface currents are modeled using the tangential magnetic fields. On the top surface and for the TM_z mode, this is expressed by

$$\vec{J}_s^{\,top,TM_z} = \vec{a}_y \times H = -\vec{a}_z H_x \tag{5.8}$$

Here, $\vec{a}$ is the unit vector. The field components are not collocated because of the staggered nature of FDTD grid. Hence, spatial averaging can be applied to magnetic fields for approximating their values on the boundaries. As shown in Fig. 5.2, H_x components are

positioned a half-cell ($\Delta y/2$) above and below of top surface; these are used in averaging source-induced surface currents. The bottom surface is not this simple because the normal direction changes according to the position of the E-field. For example, the surface normal is directed along $-\vec{a}_x$ for the boundary between nodes (i+1,j) and (i+1,j-1). Hence, source-induced surface current is obtained by averaging four H_y components located around the boundary, i.e.:

$$J_s^{bot,TM_z}(n,1) = 0.25\begin{bmatrix} H_y(i+1/2, j-1) + H_y(i+1/2, j) \\ +H_y(i+3/2, j-1) + H_y(i+3/2, j) \end{bmatrix} \quad (5.9),$$

where n is time index. For TE_z mode, H_z is used in obtaining source-induced surface currents on both top and bottom surfaces. As seen in Fig.5.3, spatial averaging is also required for this mode.

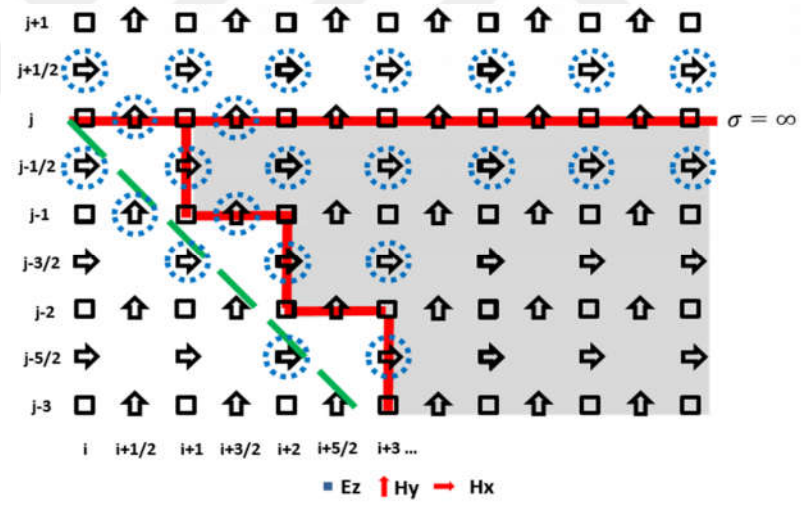

Figure 5.2 An FDTD model of the problem in the TM_z configuration. The magnetic field components used for calculation of surface currents are circled.

The novel 3-step FDTD approach used for the calculation of fringe currents in the time domain is as follows:

1) The FDTD simulation is run for the PEC wedge structure and surface currents are recorded in the time domain. On the top surface, recorded currents contain both uniform and non-uniform parts; on the bottom surface, recorded currents contain only non-uniform currents.

2) Make the wedge angle 180° (i.e., replace wedge with the half-plane), run the FDTD simulation again, and record the surface currents only on the top surface of the wedge. Recorded data contains only uniform (PO) currents.
3) Subtract data recorded in step 2 from step 1 and obtain only non-uniform currents on the top surface.

Note that, this procedure is for SSI as shown in Fig. 5.1. For the double-side illumination (DSI), where both faces of wedge is illuminated by incident field, the uniform currents are also induced on the bottom surface, hence one additional step, which is similar to step 2, needs to be performed. In this step, the bottom surface of the wedge is extended to infinity and the time domain currents are recorded. The recorded currents are formed by only uniform currents and they need to be subtracted from the total currents obtained in step 1 on bottom surface.

Note also that, these non-uniform currents are broadband therefore, FFT is applied to obtain fringe currents at a specified frequency. Finally, fringe waves are calculated using the Green's function representations given, for example, as in (3.84) for the TE and TM modes.

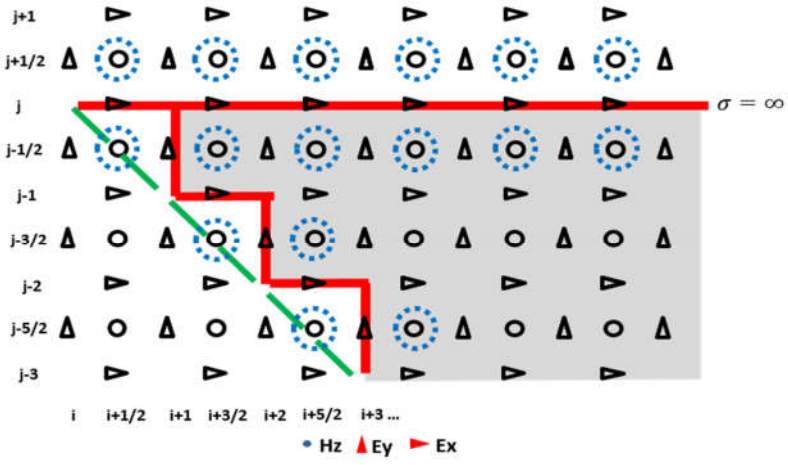

Figure 5.3 An FDTD model of the problem in the TE_z configuration. The magnetic field components used for calculation of surface currents are circled.

5.2. Examples and Comparisons

The proposed approach is validated and verified against PTD and MoM through the examples presented in Figs. 5.4-5.9. Here, different wedge angles ($0°, 45°$ and $90°$) and different angle of illuminations are used. The frequency is 30 MHz and MoM and FDTD fringe fields are normalized to PTD fringe fields. In all examples, $\Delta = \lambda / 20$ resolution is used for FDTD and $\Delta = \lambda / 10$ resolution is used for MoM.

In Fig. 5.4, TM_z fringe fields around a 90° PEC wedge, illuminated by a line source at $\rho_0 = 60, \varphi_0 = 70°$, recorded on a circle with a radius 20 m (2λ) from the tip are shown. Note that, Fig 5.4a shows angular variation of the fringe fields in the frequency domain, while Fig. 5.4b shows a snapshot during the FDTD simulations (i.e., time domain pulsed fringe fields).

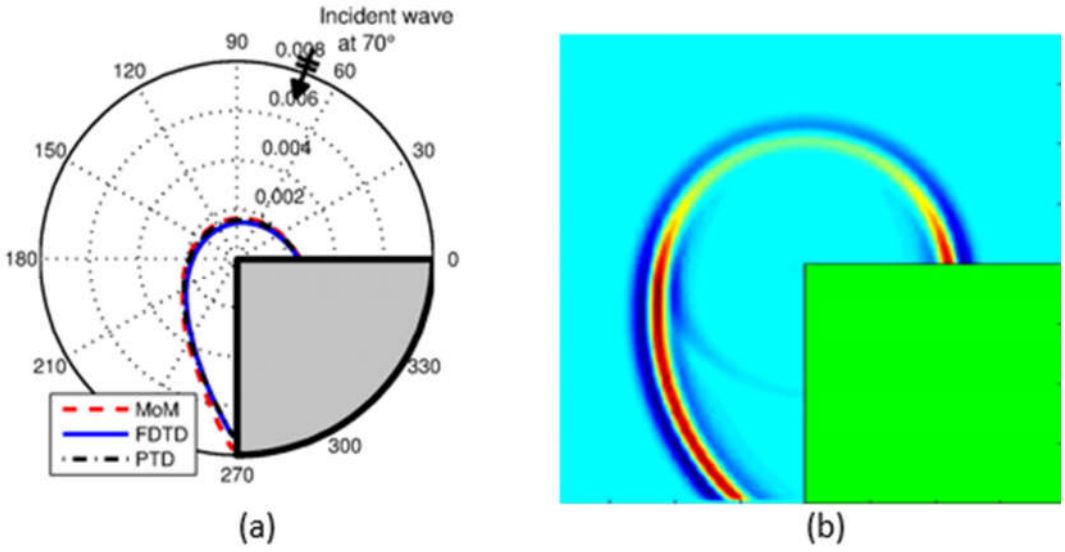

Figure 5.4 (a) Fringe fields around the tip of the wedge for TM_z polarization (SSI), Dashed: MoM, Solid: FDTD, Dashed-dotted: PTD, $\alpha = 270°$, $\rho_0 = 60m$, $\varphi_0 = 70°$, $\rho = 20m$, $f = 30MHz$; (b) A time domain snapshot showing broadband fringe fields.

Time domain characteristics of PO and fringe currents, recorded on the top surface of this wedge at a point 1.5 away from the tip, are shown at Fig.5.5. Frequency domain variations of the same point are also shown at Fig.5.6 with source's FFT.

The total (uniform + non-uniform) and non-uniform currents induced on this PEC wedge are shown in Fig.5.7. As observed, non-uniform currents concentrate in the vicinity of edge. Figures 5.8 and 5.9 belong to the same scenario but for the TE_z polarization.

The simulations are repeated for $0°$ and $45°$ PEC wedges and results are presented in Figs. 5.10 and 5.11. As observed, very good agreement among analytical and numerical methods are achieved.

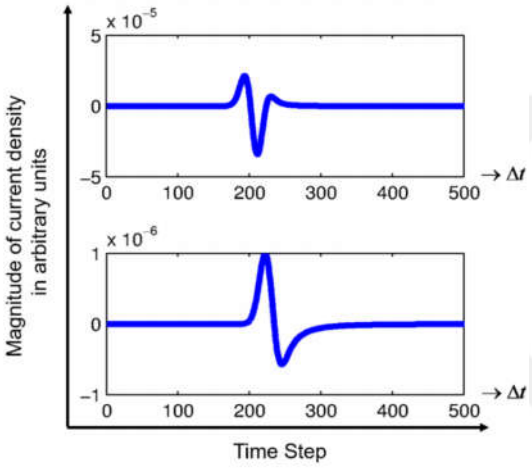

Figure 5.5 Time domain surface currents for TM_z polarization of above scenario recorded on top surface at 1.5λ distance from the tip, (Top) PO currents, (Bottom) fringe (non-uniform) currents, $\alpha = 270°$, $\rho_0 = 60m$, $\varphi_0 = 70°$, $\rho = 20m$, $f = 30MHz$.

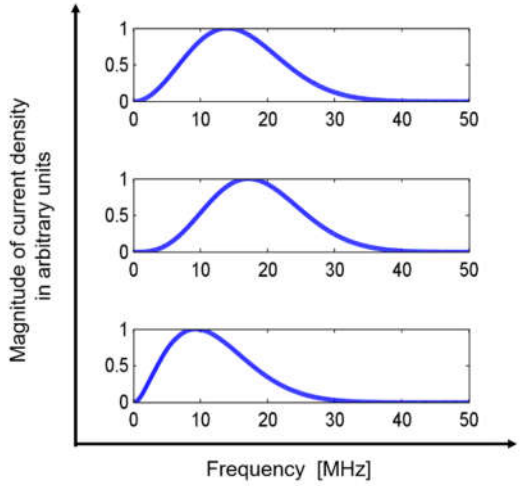

Figure 5.6 Frequency domain surface currents for TM_z polarization of above scenario recorded on top surface at 1.5λ distance from the tip, (Top) Source's FFT, (Middle) FFT of PO currents, (Bottom) FFT of fringe (non-uniform) currents, $\alpha = 270°$, $\rho_0 = 60m$, $\varphi_0 = 70°$, $\rho = 20m$, $f = 30MHz$.

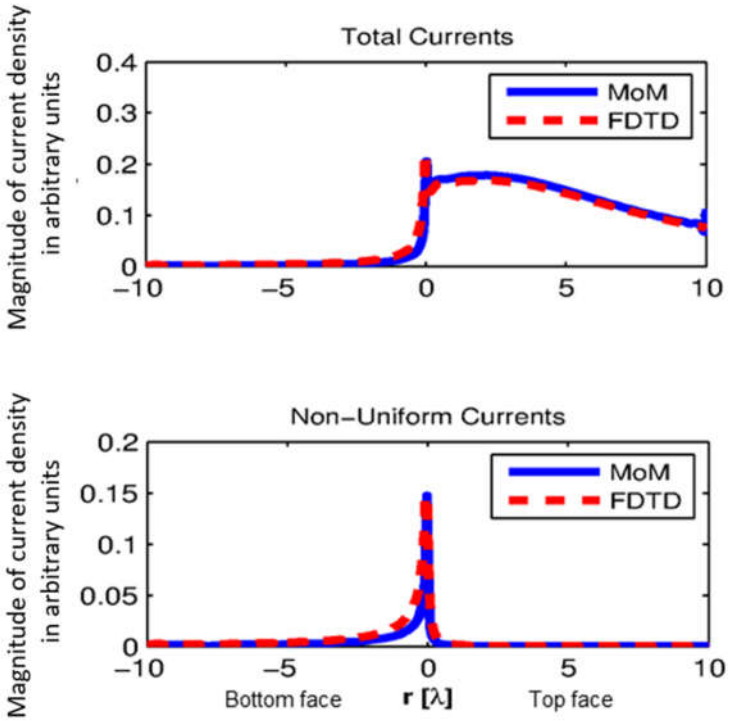

Figure 5.7 Wedge surface currents for TM_z polarization of above scenario, (Top) total currents, (Bottom) fringe (non-uniform) currents, $\alpha = 270°$, $\rho = 20m$, $f = 30MHz$ Solid: MoM, Dashed: FDTD (left and right portions belong to the bottom and top surfaces, respectively).

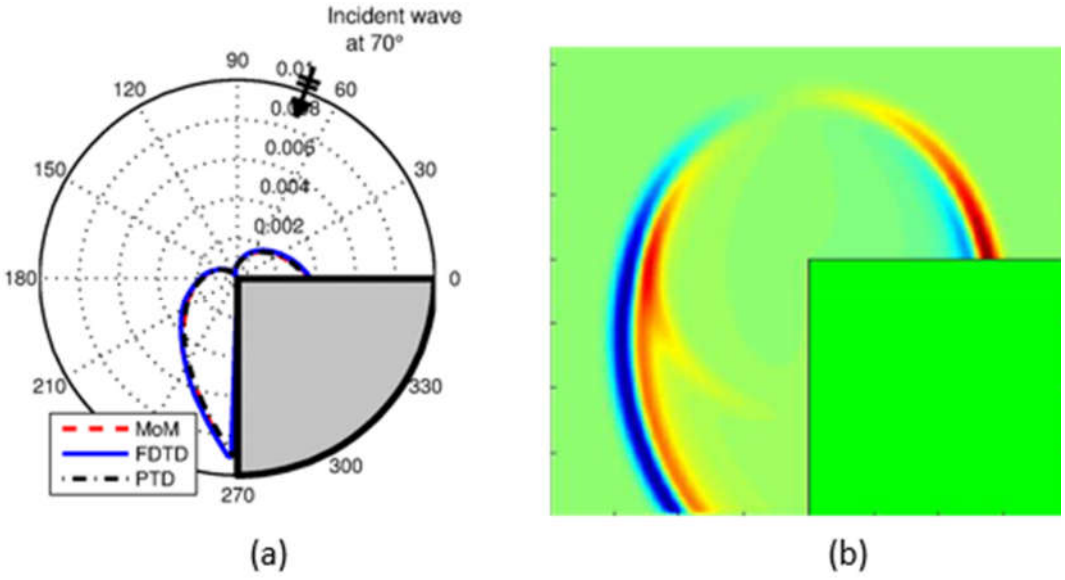

Figure 5.8 (a) Fringe fields around the tip of the wedge for TE_z polarization (SSI), Dashed: MoM, Solid: FDTD, Dashed-dotted: PTD, $\alpha = 270°$, $\rho_0 = 60m$, $\varphi_0 = 70°$, $\rho = 20m$, $f = 30MHz$; (b) A time domain snapshot showing broadband fringe fields.

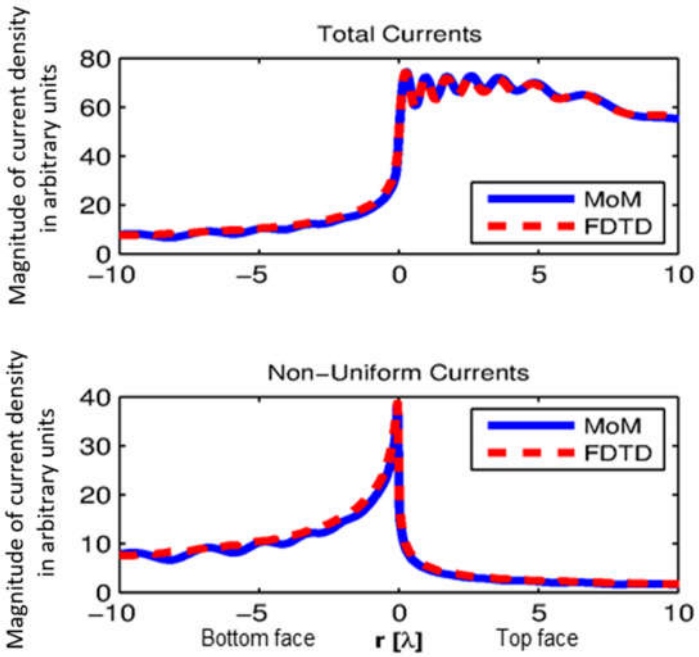

Figure 5.9 Wedge surface currents for TEz polarization of above scenario, (Top) total currents, (Bottom) fringe (non-uniform) currents, $\alpha = 270°$, $\rho_0 = 60m$, $\varphi_0 = 70°$, $\rho = 20m$, $f = 30MHz$ Solid: MoM, Dashed: FDTD (left and right portions belong to the bottom and top surfaces, respectively).

5.3. Conclusions

A novel, FDTD based diffraction modeling procedure is introduced for the simulation of fringe currents and fringe waves around a PEC wedge. The presented results verified the validity of proposed method. Note that, using geometric averaging yields better performance for collocating electric and magnetic fields [75] and the accuracy maybe increased. Also, the rectangular grid used in the standard FDTD algorithm limits the accuracy, especially for the TE polarization [76]. This limitation can be removed by using FDTD algorithms based on conformal cells [30, 77].

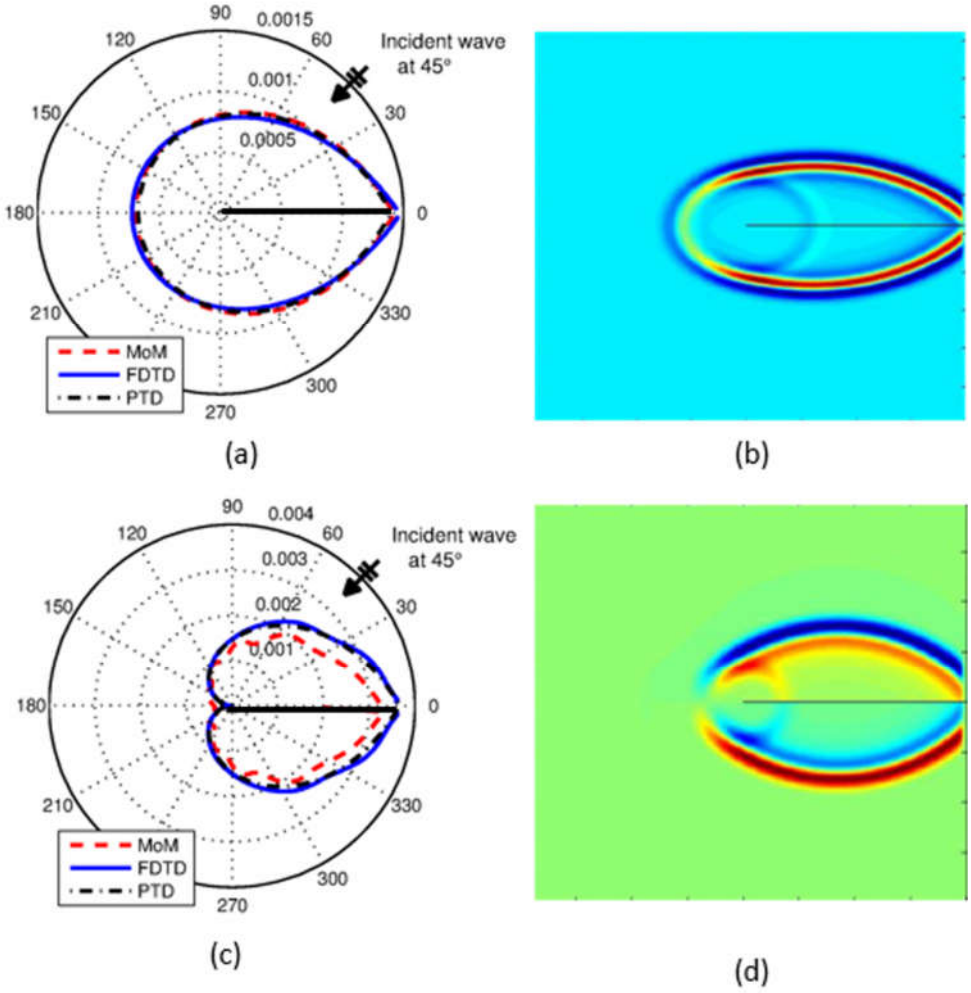

Figure 5.10 Fringe fields around the tip of the wedge (SSI), Dashed: MoM, Solid: FDTD, Dashed-dotted: PTD, $\alpha = 360°$, $\rho_0 = 70m$, $\varphi_0 = 45°$, $\rho = 20m$, $f = 30MHz$, (a) and (c) Polar plot for TM_z and TE_z mode, (b) and (d) Time domain snapshot for TM_z and TE_z mode.

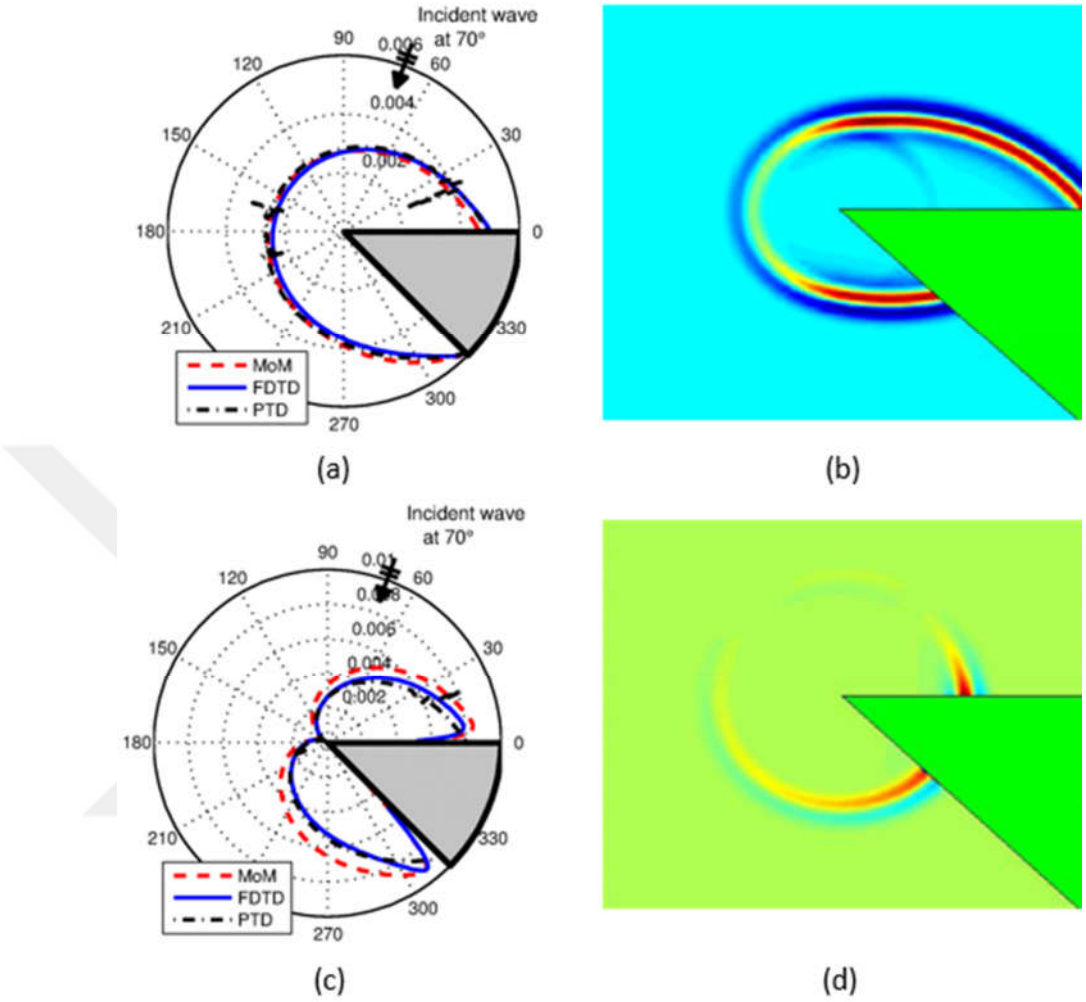

Figure 5.11 Fringe fields around the tip of the wedge (SSI), Dashed: MoM, Solid: FDTD, Dashed-dotted: PTD, $\alpha = 315°$, $\rho_0 = 60m$, $\varphi_0 = 70°$, $\rho = 5m$, $f = 30MHz$, (a) and (c) Polar plot for TM_z and TE_z mode, (b) and (d) Time domain snapshot for TM_z and TE_z mode.

6. CONCLUSIONS AND FUTURE WORK

6.1. Conclusions

This thesis contributes to the literature on diffraction theory by presenting three novel studies. First, double tip diffraction phenomena is studied on 2D PEC structure which is shown at Fig. 3.3. FDTD based multi-step diffraction model is introduced. The novelty of this work is that, for the first time in literature, double tip diffracted fields are extracted from total fields. The validity of the proposed model is proved with MoM simulations presented in section 3.4. This work is published in IEEE Transactions on Antennas and Propagation journal [11].

Secondly, diffraction from 2D strip geometry with one face is soft (PEC) BC and the other hard (PMC) BC is considered. These materials does not exist in nature but the latest advances in technology enables them to be produced artificially [68], [69]. In this work, time domain diffraction model for SHBC strip geometry is introduced via FDTD method. The novelty of this work is that, for the first time in literature, diffracted fields formed from soft-hard strip structure are extracted from total fields in time domain. Analyzing diffracted field in time domain helps to understand the physics underlying the diffraction phenomena. The validity of the proposed model is proved via existing MoM model with comparisons presented in section 4.3. This work is submitted to IEEE Transactions on Antennas and Propagation journal for review [12].

Finally, a time domain model is introduced to obtain fringe currents and fringe waves on canonical 2D PEC wedge geometry. Fringe waves constitute a portion of diffracted fields and can be seen as correction to the physical optic diffracted fields which are formed by abrupt termination of induced currents [5]. The novelty of this paper is that, for the first time in the literature, fringe currents and waves are obtained in time domain with FDTD method. With the introduced method, the contribution of fringe (non-uniform) currents to diffracted field can be observed in time domain visually. The validity of the proposed model is proved via comparisons with existing PTD and MoM solutions presented in section 5.2. This work is submitted to IEEE Transactions on Antennas and Propagation journal for review [13].

6.2. Future Work

The following studies can be carried out in the future:

1) In this thesis we addressed 2D diffraction models. To handle more realistic problems, the introduced models should be extended to 3D.
2) We consider PEC/PMC objects for diffraction modeling. The models can be extended for objects composed of dielectric materials. Although it is hard to derive such a model, it may be obtained for specific incident and observation angles. An instructive work carried on canonical wedge geometry [52].
3) All diffraction models can be assembled in a Graphical User Interface (GUI) and made available as a teaching tool for lecturers and students.

REFERENCES

[1] A. Sommerfeld, "The propagation of waves in wireless telegraphy," *Ann. der Phys.,* vol. 28, pp. 665-736, 1909.

[2] G. Tyras, Radiation and Propagation of Electromagnetic Waves, 111 Fifth Avenue, New York: Academic Press Inc., 1969.

[3] J. B. Keller, "Geometrical Theory of Diffraction," *Journal Optical Society of America ,* vol. 52, no. 2, pp. 116-130, 1962.

[4] R. Pathak and P. Kouyoumjian, "A uniform geometrical theory of diffraction for an edge in a perfectly conducting surface," *Proceedings of the IEEE,* vol. 62, no. 11, pp. 1448-1461, 1974.

[5] P. Y. Ufimtsev, Fundamentals of the Physical Theory of Diffraction, John Wiley & Sons, Inc., 2006.

[6] P. Y. Ufimtsev, Theory of edge diffraction in electromagnetics, Tech Science Press; 1st edition, 2003.

[7] P. Uslenghi, Electromagnetic Scattering, 111 Fifth Avenue, New York: Academic Press Inc , 1978.

[8] K. Yee, "Numerical solution of initial boundary value problems involving maxwell's equations in isotropic media," *Antennas and Propagation, IEEE Transactions on ,* vol. 14, no. 3, pp. 302-307, May 1966.

[9] R. F. Harrington, Field Computation by Moment Methods, Wiley-IEEE Press, 1993.

[10] J.-M. Jin, The Finite Element Method in Electromagnetics, Wiley-IEEE Press, 2002.

[11] M. Uslu, G. Apaydin and L. Sevgi, "Double Tip Diffraction Modeling: Finite Difference Time Domain vs. Method of Moments," *Antennas and Propagation, IEEE Transactions on,* vol. 62, no. 12, pp. 6337-6343, 2014.

[12] M. Uslu, G. Apaydin and L. Sevgi, "Diffraction Modeling by a Soft-Hard Strip: Finite Difference Time Domain vs. Method of Moments," *Antennas and Propagation, IEEE Transactions on,* p. submitted for publication, 2015.

[13] M. Uslu, G. Apaydin and L. Sevgi, "Finite Difference Time Domain Modeling of Fringe Waves," *Antennas and Propagation, IEEE Transactions on,* p. submitted for publication, 2015.

[14] A. C. Balanis, Advanced Engineering Electromagnetics (2nd ed.), River Street,Hoboken, NJ: Wiley, 2012.

[15] G. Apaydin, F. Hacivelioglu and P. Ufimtsev, "Wedge Diffracted Waves Excited by a Line Source: Method of Moments (MoM) Modeling of Fringe Waves," *Antennas and Propagation, IEEE Transactions on,* vol. 62, no. 8, pp. 4368 - 4371, 2014.

[16] "Robert O'Donnell. RES.LL-001 Introduction to Radar Systems, Spring 2007. (Massachusetts Institute of Technology: MIT OpenCourseWare), http://ocw.mit.edu (Accessed 2 Jan, 2016). License: Creative Commons BY-NC-SA," [Online].

[17] E. Knott, J. Shaeffer and M. Tuley, Radar Cross Section, Raleigh,NC: SciTech Publishing, Inc., 2004.

[18] E. Saleh and M. Teich, Fundamentals of Photonics (2nd Ed.), 111 River Street, Hoboken, NJ: Wiley-Interscience, 2007.

[19] E. Wolf and M. Born, Principles of Optics, New York: Pergamon Press, 1959.

[20] M. Kline, Electromagnetic theory and geometrical optics, CHARLESTON, SC : Nabu Press, 2011.

[21] G.L.James, Geometrical Theory of Diffraction for Electromagnetic Waves, Ieee Electromagnetic Waves Series, 1979.

[22] D. Jenn, Radar and Laser Cross Section Engineering, Second Edition, AIAA, 2005.

[23] W. C. Gibson, The Method of Moments in Electromagnetics, Broken Sound Parkway, NW, Suite 300: CRC Press, 2008.

[24] R. Perez, Handbook of Electromagnetic Compatibility, Academic Press, 1995.

[25] L. Sevgi and E. Arvas, "A Tutorial on the Method of Moments," *Antennas and Propagation Magazine, IEEE,* vol. 54, no. 3, pp. 260-275, 2012.

[26] A. Polycarpou, Introduction to the Finite Element Method in Electromagnetics, Morgan & Claypool Publishers, 2006.

[27] M. N. Sadiku, “A Simple Introduction to Finite Element Analysis of Electromagnetic Problems,” *IEEE Transactions on Education,* vol. 32, no. 2, pp. 85-93, May 1989.

[28] J. L. Volakis, A. Chatterjee and L. Kempel, Finite Element Method Electromagnetics: Antennas, Microwave Circuits, and Scattering Applications, Wiley-IEEE Press, 1998.

[29] G. Murr, "Absorbing Boundary Conditions for the Finite-Difference Approximation of the Time-Domain Electromagnetic-Field Equations," *Electromagnetic Compatibility, IEEE Transactions on ,* Vols. EMC-23, no. 4, pp. 377-382, 1981.

[30] A. Taflove and S. Hagness, Computational Electrodynamics: The Finite-Difference Time-Domain Method, Third Edition ed., Artech House Antennas and Propagation Library, 2005.

[31] J. Berenger, Perfectly Matched Layer (PML) for Computational Electromagnetics, Morgan & Claypool, 2007.

[32] H. Jamid, "Enhanced PML performance using higher order approximation," *Microwave Theory and Techniques, IEEE Transactions on ,* vol. 52, no. 4, pp. 1166 - 1174, 2004.

[33] P. Talukder, F. Schmuckle and W. Heinrich, "Optimizing the FDFD Method in Order to Minimize PML-Related Numerical Problems," in *Microwave Symposium, 2007. IEEE/MTT-S International*, Honolulu, HI, 2007.

[34] P. Monk and E. Suli, "Error estimates for Yee's method on non-uniform grids," *Magnetics, IEEE Transactions on,* vol. 30, no. 5, pp. 3200 - 3203, 1994.

[35] M. Steeds, S. Broschat and J. Schneider, "A comparison of two conformal methods for FDTD modeling," *Electromagnetic Compatibility, IEEE Transactions on,* vol. 38, no. 2, pp. 181-187, 1996.

[36] Y. Wenhua, R. Mittra, Y. Xiaoling, Y. L., Q. R. and M. A., "High-Performance Conformal FDTD Techniques," *Microwave Magazine, IEEE,* vol. 11, no. 4, pp. 43-55, 2010.

[37] U. S. Inan and M. R. A, Numerical Electromagnetics: The FDTD Method, New York: Cambridge University Press, 2011.

[38] C. Railton and J. Schneider, "An analytical and numerical analysis of several locally conformal FDTD schemes," *Microwave Theory and Techniques, IEEE Transactions on,* vol. 47, no. 1, pp. 56 - 66, Jan 1999.

[39] R. Fitzpatrick, "Electromagnetism and Optics," 14 July 2007. [Online]. Available: http://farside.ph.utexas.edu/teaching/302l/lectures/node150.html.

[40] F. Hacivelioglu, L. Sevgi and P. Ufimtsev, "On the modified theory of physical optics," *IEEE Trans. Antennas Propag.,* vol. 61, no. 12, pp. 6115-6119, Dec. 2013.

[41] C. Balanis, L. Sevgi and P. Ufimtsev, "Fifty years of high frequency diffraction," *Int. J. RF Microw. Computer-Aided Eng.,* vol. 23, no. 4, pp. 394-402, 2013.

[42] G. Pelosi, Y. Rahmat-Samii and J. Volakis, "High-frequency techniques in diffraction theory: 50 years of achievements in GTD, PTD,related approaches," *IEEE Antennas Propag. Mag.,* vol. 55, no. 4, pp. 17-19, Aug 2013.

[43] P. Ufimtsev, "The 50-year anniversary of the PTD: Comments on the PTD's origin and development," *IEEE Antennas Propag. Mag.,* vol. 55, no. 3, pp. 18-28, 2013.

[44] Y. Rahmat-Samii, "GTD, UTD, UAT, STD: A historical revisit and personal

observations," *IEEE Antennas Propag. Mag.,* vol. 55, no. 3, pp. 29-40, Jun. 2013.

[45] G. Pelosi and S. Selleri, "The wedge-type problem: The building brick in high-frequency scattering from complex objects," *IEEE Antennas and Propagation Mag.,* vol. 55, no. 3, pp. 41-58, Jun 2013.

[46] F. Hacivelioglu, M. Uslu and L. Sevgi, "A Matlab-based virtual tool for the electromagnetic wave scattering from a perfectly reflecting wedge," *IEEE Antennas Propag. Mag.,* vol. 53, no. 6, pp. 234-243, Dec. 2011.

[47] F. Hacivelioglu, L. Sevgi and P. Ufimtsev, "Backscattering from soft-hard strip: Primary edge waves approximations," *IEEE Antennas Wireless Propag. Lett.,* vol. 12, pp. 249-252, 2013.

[48] G. Stratis, V. Anantha and A. Taflove, "Numerical calculation of diffraction coefficients of generic conducting and dielectric wedges using FDTD," *IEEE Trans. Antennas Propag.,* vol. 45, no. 10, pp. 1525-1529, Oct. 1997.

[49] G. Cakir, L. Sevgi and P. Y. Ufimtsev, "FDTD modeling of electromagnetic wave scattering from a wedge with perfectly reflecting boundaries: Comparisons against analytical models and calibration," *IEEE Trans. Antennas Propag.,* vol. 60, no. 7, p. 3336–3342, Jul. 2012.

[50] M. Uslu and L. Sevgi, "Matlab-based virtual wedge scattering tool for the comparison of high frequency asymptotics and FDTD method," *App. Comp. Electromagn. Soc. J.,* vol. 27, no. 9, pp. 697-705, Sep. 2012.

[51] G. Apaydin and L. Sevgi, "A novel wedge diffraction modeling using method of moments," *App. Comp. Electromagn. Soc. J.,* submitted for publication.

[52] D. Stratis, A. V. and A. Taflove, "Numerical calculation of diffraction coefficients of generic conducting and dielectric wedges using FDTD," *IEEE Trans. Antennas Propag.,* vol. 45, no. 10, p. 1525–1529, Oct. 1997.

[53] R. Tiberio, G. Manara, G. Pelosi and R. G. Kouyoumjian, "Scattering by a strip with 2

face impedances at edge-on incidence," *Radio Sci.,* vol. 17, no. 5, pp. 1199-1210, 1982.

[54] R. Tiberio, G. Manara, G. Pelosi and R. G. Kouyoumjian, "High frequency diffraction by a double wedge," in *IEEE Int. Symp. on Antennas Propag.*, Vancouver, Canada,, Jun. 1985.

[55] R. Tiberio, G. Manara, G. Pelosi and R. G. Kouyoumjian, "High-frequency electromagnetic scattering of plane-waves from double wedges," *IEEE Trans. Antennas Propag.,* vol. 37, no. 9, p. 1172–1180, Sep. 1989..

[56] M. Schneider and R. Luebbers, "A general uniform double wedge diffraction coefficient," *IEEE Trans. Antennas Propag.,* vol. 39, no. 1, pp. 8-14, Jan. 1991.

[57] L. P. Ivrissimtzis and R. J. Marhefka, "A note on double edge-diffraction for parallel wedges," *IEEE Trans. Antennas Propag.,* vol. 39, no. 10, pp. 1532-1537, Oct. 1991.

[58] M. Albani, F. Capolino, S. Maci and R. Tiberio, "Double diffraction coefficients for source and observer at finite distance for a pair of wedges," *Proc. IEEE Int. Symp. on Antennas and Propagation,* vol. 2, pp. 1352-1352, 1995.

[59] F. Capolino and S. Maci, "Uniform high-frequency description of singly, doubly, vertex diffracted rays for a plane angular sector," *J. Electromagn. Waves Applicat.,* vol. 10, no. 9, p. 1175–1197, Oct.1996.

[60] I. Herman and J. L. Volakis, "High-frequency scattering by a double impedance wedge," *IEEE Trans. Antennas Propag.,* vol. 36, no. 5, p. 664–678, May 1998.

[61] M. Albani, "A uniform double diffraction coefficient for a pair of wedges in arbitrary configuration," *IEEE Trans. Antennas Propag.,* vol. 53, no. 2, pp. 702-710, Feb. 2005.

[62] A. Karousos and C. Tzaras, "Time-domain diffraction for a double wedge obstruction," *Proc. IEEE Int. Symp. on Antennas Propag.,* p. 4153–4156, Jun. 2007.

[63] J. M. L. Bernard, "A spectral approach for scattering by impedance polygons," *Quart.*

J. Mechan. Appl. Math., vol. 59, no. 4, pp. 517-550, Nov. 2006.

[64] D. Erricolo, U. G. Crovella and P. L. E. Uslenghi, "Time-domain analysis of measurements on scaled urban models with comparisons to ray-tracing propagation simulation," *IEEE Trans. Antennas Propag.,* vol. 50, no. 5, pp. 736-741, May 2002.

[65] D. Erricolo, D. G. and P. L. E. Uslenghi, "Measurements on scaled models of urban environments and comparisons with ray-tracing propagation simulation," *IEEE Trans. Antennas Propag.,* vol. 50, no. 5, pp. 727-735, May 2002.

[66] D. Erricolo, "Experimental validation of second order diffraction coefficients for computation of path-loss past buildings," *IEEE Trans. Electromagn. Compat.,* vol. 44, no. 1, pp. 272-273, Feb. 2002.

[67] T. Negishi, V. Picco, D. Spitzer, D. Erricolo, G. Carluccio, F. Puggelli and M. Albani, "Measurements to validate the UTD triple diffraction coefficient," *IEEE Trans. Antennas Propag.,* vol. 62, no. 7, pp. 3723 - 3730, Jul. 2014.

[68] J. Sohn, K. Kim and H. -S. Tae, "Comparative study on various artifical magnetic conductors for low-profile antenna," *Prog. in EM Res., PIER,* vol. 61, pp. 27-37, 2006.

[69] P. Kildal, A. Kishk and S. Maci, "Special Issue on Artificial Magnetic Conductors, Soft/Hard Surfaces, and Other Complex Surfaces," *IEEE Trans. Antennas Propag.,* vol. 53, no. 1, Jan. 2005.

[70] G. Apaydin and L. Sevgi, "Method of moments (MoM) simulation of backscattering by a soft-hard strip," *IEEE Trans. Antennas Propag. submitted for publication.*

[71] H. Macdonald, Electric Waves, Cambridge University Press, 1902.

[72] F. Hacivelioglu, L. Sevgi and P. Ufimtsev, "Wedge diffracted waves excited by a line source: Exact and asymptotic forms of fringe waves," *IEEE Trans. Antennas Propag.,* vol. 61, no. 9, pp. 4705-4712, Sept. 2013.

[73] J. Bowman, T. Senior and P. Uslenghi, Electromagnetic and Acoustic Scattering by Simple Shapes, New York: Hemisphere, 1987.

[74] F. Hacivelioglu, L. Sevgi and P. Ufimtsev, "On the numerical evaluation of diffraction formulas for the canonical wedge scattering problem," *IEEE Antennas Propag. Mag.,* vol. 55, no. 5, pp. 257-272, Oct. 2013.

[75] D. Robinson and S. J., "On the use of the geometric mean in fdtd near-to-far-field transformations," *IEEE Trans. Antennas Propag.,* vol. 55, no. 11, pp. 3204-3211, Nov. 2007.

[76] H. R., "Pitfalls of staircase meshing," *IEEE Trans. Electromagnetic Compatibility,* vol. 35, no. 4, pp. 434-439, Nov. 1993.

[77] S. Dey and R. Mittra, "A locally conformal finite-difference time-domain (FDTD) algorithm for modeling three-dimensional perfectly conducting objects," *IEEE Micro. Guided Wave Lett.,* vol. 7, pp. 273-275, 1997.

LIST OF PUBLICATIONS

Sci-indexed Journal Papers

1. A. Sefer, M.A. Uslu, L.Sevgi, “MATLAB-Based 3-D MoM and FDTD Codes for the RCS Analysis of Realistic Objects,” *IEEE Antennas and Propagation Magazine*, Vol:57, Issue:4, pp.122-148, Aug. 2015.
2. M.A. Uslu, G Apaydin, L. Sevgi, " Diffraction Modeling by a Soft-Hard Strip: Finite Difference Time Domain vs. Method of Moments", *Antennas and Propagation, IEEE Transactions on*, submitted for publication.
3. M.A. Uslu, G Apaydin, L. Sevgi, " Finite Difference Time Domain Modeling of Fringe Waves", *Antennas and Propagation, IEEE Transactions on*, submitted for publication.
4. M.A. Uslu, G Apaydin, L. Sevgi, "Double Tip Diffraction Modeling: Finite Difference Time Domain vs. Method of Moments", *Antennas and Propagation, IEEE Transactions on*, Oct. 2014.
5. G. Toroğlu, M.A. Uslu, L. Sevgi, “RCS2D: A 2D MoM and FDTD based Scattering Simulator”, *International Journal of RF and Microwave Computer-Aided Engineering* Wiley July 2013.
6. G. Toroğlu, M.A. Uslu, L. Sevgi, “RCS2D: A 2D Scattering Simulator for MoM vs. FDTD Comparisons”, *ACES, Int Journal on Applied Computational Electromagnet*ics Vol:28, Issue:3, pp.173-177, March 2013.
7. M. A. Uslu, L. Sevgi, “Matlab-Based Virtual Wedge Scattering Tool for the Comparison of High Frequency Asymptotics and FDTD Method,” *ACES, Int Journal on Applied Computational Electromagnetics* Vol:27, Issue:9, pp.697-705, Sep. 2012.
8. M. A. Uslu, L. Sevgi, Matlab-Based Filter Design Program : From Lumped Elements to Microstriplines, *IEEE Antennas and Propagation Magazine*, Vol:53, Issue:1, pp.213-224, Feb. 2011.
9. F. Hacıvelioglu, M. A. Uslu, L. Sevgi, A MatLab-based Virtual Tool for the Electromagnetic Wave Scattering from a Perfectly Reflecting Wedge, *IEEE Antennas and Propagation Magazine*, Vol:53, Issue:6, pp.234-243, Dec. 2011.

Conference Papers

1. M.A. Uslu, G. Apadın, L.Sevgi, "EMC/EMI Problems and Diffraction Modeling: Finite Difference Time Domain vs. Method of Moments", EMC'14 Tokyo / Tokyo Japan.
2. G. Toroğlu, M.A. Uslu, L. Sevgi, “RCS2D: A 2D MoM and FDTD based Scattering Simulator”, ACES 2013 / California USA.
3. G. Toroğlu, M.A. Uslu, L. Sevgi, “RCS2D: 2D Electromagnetic Simulator based on MoM and FDTD”, MMS 2012 / Istanbul.
4. M. A. Uslu, L. Sevgi, “FDTD Modeling of Electromagnetic Wave Scattering from a Non-Penetrable Wedge,” APEMC 2012 / Singapore.
5. M. A. Uslu, L. Sevgi, “Modeling and Simulation of Electromagnetic Wave Diffraction: High Frequency Asymptotics vs. FDTD” MMS 2012, Mediterranean Microwave Symposium, Dogus University – Istanbul, Sep. 2012.
6. M. A. Uslu, L. Sevgi, “MATLAB Based Filter Design Program:From Lumped Elements to Microstriplines,” EMC Europe 2011, York/England.

BIBLIOGRAPHY

Mehmet Alper USLU was born in Bolu, Turkey. He received B.Sc, M.Sc degrees in 2010 and 2011 in Electronics and Communications engineering from Dogus University respectively. He is continuing Ph.D. education at the same university since 2011. He has published more than 15 papers in international journals and international/national conferences.

Due to his research on applied electromagnetic, he is bestowed Leopold B. Felsen Excellence in Electromagnetics award in 2011. He completed his graduate education with high honor degree and received Outstanding Achievement award from Dogus University. He is also granted visiting scholar award from University of Massachusetts Lowell – USA in 2012.

He developed OS/Firmware for ARM based SOCs, Radar Cross Section Simulator, Numerical Tool for analyzing scattered fields formed from wedge shaped obstacles, A Novel Filter design software which automates Kuroda Transformations. He took part in various national, international conference organization committees.

His research interests are diffraction theory, radar system design, computational electromagnetics, RF Microwave circuits and systems, EMC, Digital Signal Processing Algorithms, Real-time/Embedded Software Development, Radar Cross Section modeling, Stealth technology and Aerodynamics.

He is a member of IEEE Antennas and Propagation Society, Applied Electromagnetic Society (ACES) and Institute of Electronics, Information and Communication Engineers (IEICE). His hobbies are winter sports, chess, photography, and reading.

He is Oracle Certified Java Programmer and currently working as Senior Radar Design and Software Engineer at NETAS.